

Discrete luminescence particle imaging to determine temperature distributions in highly scattering solid-fluid systems

Dissertation

zur Erlangung des akademischen Grades

Doktoringenieur

Dr.-Ing.

von **MSc. Guangtao Xuan**

geb. am 22.11.1991 in Guangxi, China

genehmigt durch die Fakultät für Verfahrens- und Systemtechnik
der Otto-von-Guericke-Universität Magdeburg

Promotionskommission: Prof. Dr. Ulrich Krause (Vorsitzender)
Dr. Benoît Fond (Betreuer, Gutachter)
Prof. Dr. Sebastian Kaiser (Gutachter)
Prof. Dr.-Ing. Frank Beyrau (Gutachter)

eingereicht am: November 30, 2023

Promotionskolloquium am: April 15, 2024

Xuan, Guangtao:

Discrete luminescence particle imaging to determine temperature distributions in highly scattering solid-fluid systems

Dissertation, Otto-von-Guericke University

Magdeburg, 2023.

Declaration

I hereby declare that I prepared this dissertation with the title:

Discrete luminescence particle imaging to determine temperature distributions in highly scattering solid-fluid systems

is submitted without inadmissible assistance and without the use of any aids other than those indicated. Facts or ideas taken from other sources, either directly or indirectly, have been marked as such.

In particular, I did not use the services of a commercial graduation consultation. Further, I have not made payments to third parties either directly or indirectly for any work connected with the contents of the submitted dissertation.

The work has not so far been submitted either in Germany or abroad in the same or similar form as a dissertation and has also not yet been published as a whole.

Guangtao Xuan

November 2023, Magdeburg

Abstract

Experimental temperature measurement in solid-fluid systems is essential to the development of new energy-efficient chemical processes involving pyrolysis, calcination, and catalysis. Compared to the conventional thermometry method with physical probes, e.g., thermocouples, optical thermometry techniques are preferable since they would not perturb the measured environment. However, a challenge in the application of optical techniques to solid-fluid systems is the presence of solid boundaries which can lead to multiple reflections. In extreme cases, such as in porous structures composed of solid particles, the use of direct imaging methods is prevented as opaque particles would block the direct light paths.

Phosphor thermometry as an optical technique has been demonstrated for temperature imaging, relying on solid luminescent particles, i.e., phosphor particles, dispersed in fluids or coated on solid surfaces. To derive temperature, the temporal or spectral dynamics of the luminescence with temperature are exploited. For this, the luminescence is spectrally or temporally separated into two separate signals, resulting in a temperature-dependent ratio of these signals. This thesis introduces two innovative concepts based on ratiometric phosphor thermometry, aimed to address the scattering and reflection issues caused by solid boundaries. Both concepts leverage the fact that luminescence originates from discrete emitters.

The first concept involves dispersing micron-sized phosphor particles in transparent fluids and subsequently forming separated diffraction-limited images of the particle luminescence on high-resolution cameras. In this way, each phosphor particle is treated as an independent temperature detector located at discrete particle positions. 2D rotated Gaussian functions are fitted to each particle image, allowing for integrating particle signals in the separated images for ratiometric thermometry and locating the particles with sub-pixel resolution ($< 10 \mu m$). This fitting process can separate the luminescence signal of the imaged particles from interfering signals with a low spatial

frequency, such as those from surface reflection or re-scattering of luminescence light. Initial experiments are conducted in a liquid dispersion and in a seeded gas with an imposed scattering interference from an LED light, which demonstrate the feasibility of this concept, and the robustness of the temperature measurements against high levels of re-scattered signals. The concept focuses on finely resolving the temperature distribution within a 500 μm thermal boundary layer. The results are validated against the laminar Prandtl-Blasius equation. Moreover, the performance of different optical imaging configurations employing the spectral separation method is compared to analyze the measurement deviation. As an alternative ratiometric way to the spectral separation method, the dual-frame lifetime method is also explored by performing some test cases in isothermal liquid dispersions.

The second concept combines phosphor thermometry and ray tracing simulations to determine the internal temperatures of an opaque porous structure. To establish and validate this concept, a reproducible regular packed bed is selected. The luminescence from a phosphor-coated sphere inside the packed bed, excited by penetrating laser, exits the bed after multiple reflections and is collected to determine the sphere's temperature using the dual-frame lifetime method. When multiple phosphor-coated spheres are present in packed beds, their signals can be separated by linear regression of their spatial intensity distributions in the acquired images. This is demonstrated using a setup including three luminescent spheres, with the results validated against thermocouple readings. However, purely experimental measurements only apply to regular packed beds, whereas the practical situation is ordinarily irregular. Hence, a ray tracing simulation is carried out and the results demonstrate that its combination with phosphor thermometry can substantially streamline the measurement process while offering adaptability for temperature detection in irregular packed beds.

This thesis contributes to the development of advanced temperature measurement techniques in solid-fluid systems, constituting a solid foundation for downsizing the measurement scale and optimizing the CFD simulation.

Kurzzusammenfassung

Experimentelle Temperaturmessungen in Fest-Fluid-Systemen sind für die Entwicklung neuer energieeffizienter chemischer Prozesse, einschließlich Pyrolyse, Kalzinierung und Katalyse, unerlässlich. Im Vergleich zu konventionellen Thermometriemethoden mit physischen Sonden, wie beispielsweise Thermoelementen, sind optische Thermometrietechniken häufig bevorzugt, da sie die Messumgebung nicht stören. Eine Herausforderung bei der Anwendung optischer Techniken in Fest-Fluid-Systemen besteht jedoch in der Anwesenheit von festen Grenzflächen, die zu mehrfachen Reflexionen führen können. In extremen Fällen, wie in porösen Strukturen aus festen Partikeln, wird die Verwendung direkter Bildgebungsverfahren verhindert, da undurchsichtige Partikel die direkte Sichtverbindungen blockieren. Phosphor-Thermometrie wurde in optischen Temperaturmessungen demonstriert und basiert auf festen leuchtenden Partikeln (Phosphorpartikel), die in Fluiden dispergiert oder auf festen Oberflächen beschichtet werden. Zur Ableitung der Temperatur werden die zeitlichen oder spektralen Dynamiken der Lumineszenz mit der Temperatur ausgenutzt. Hierbei wird die Lumineszenz spektral oder zeitlich in mehrere Signale getrennt, was zu einem temperaturabhängigen Verhältnis dieser Signale führt. Diese Arbeit stellt zwei innovative Konzepte der ratiometrischen Phosphor-Thermometrie vor, die darauf abzielen, die durch feste Grenzflächen verursachten Streu- und Reflexionsprobleme zu bewältigen. Beide Konzepte nutzen die Tatsache aus, dass die Lumineszenz von diskreten Emittoren ausgeht. Das erste Konzept beinhaltet die Dispergierung mikrometergroßer Phosphorpartikel in transparenten Fluiden und die anschließende Bildung separater beugungsbegrenzter Bilder der Lumineszenz der Partikel auf einer hochauflösenden Kamera. Auf diese Weise wird jeder Phosphorpartikel als unabhängiger Temperatursensor an diskreten Partikelpositionen behandelt. Jedes Partikelbild wird mit 2D Gauß-Funktionen modelliert, um Partikelsignale in den separierten Bildern für die ratiometrische Thermometrie zu integrieren und die Partikel mit subpixelgenauer Auflösung ($< 10 \mu m$) zu lokalisieren.

Dieser Anpassungsvorgang kann das Lumineszenzsignal der abgebildeten Partikel von störenden Signalen mit niedriger räumlicher Frequenz trennen, wie z.B. von Oberflächenreflexionen oder der erneuten Streuung des Lumineszenzlichts. Erste Experimente wurden in einer Flüssigdispersion und in einem mit Partikeln versehenen Gasstrom mit einer aufgeprägten Streuinterferenz von einem LED-Licht durchgeführt, was die Machbarkeit dieses Konzepts und die Robustheit der Temperaturmessungen gegenüber hohen Leveln an erneuten gestreuten Signalen zeigt. Das Konzept konzentriert sich darauf die Temperaturverteilung innerhalb einer 500 μm dünnen thermischen Grenzschicht fein aufzulösen. Die Ergebnisse werden gegen die laminare Prandtl-Blasius-Gleichung validiert. Darüber hinaus wird die Leistung verschiedener optischer Bildgebungskonfigurationen, die die spektrale Separationsmethode verwenden, verglichen, um die Messabweichung zu analysieren. Als alternative ratiometrische Methode zur spektralen Separationsmethode wird auch die Doppelbild-Lebensdauer-Methode durchgeführt, indem einige Versuche in isothermer Flüssigdispersion durchgeführt werden. Das zweite Konzept kombiniert die Phosphor-Thermometrie und Ray-Tracing-Simulationen, um die internen Temperaturen einer undurchsichtigen porösen Struktur zu bestimmen. Um dieses Konzept zu etablieren und zu validieren, wird ein reproduzierbares, regelmäßiges Festbett ausgewählt. Die Lumineszenz einer phosphorbeschichteten Kugel im Inneren des Festbetts, angeregt durch eingeleitetes Laser-Licht, verlässt das Bett nach mehrfachen Reflexionen und wird gesammelt, um die Temperatur der Kugel mithilfe der Doppelbild-Lebensdauer-Methode zu bestimmen. Wenn mehrere phosphorbeschichtete Kugeln im Festbett vorhanden sind, können ihre Signale durch lineare Regression ihrer räumlichen Intensitätsverteilungen in den aufgenommenen Bildern getrennt werden. Dies wird anhand eines Aufbaus mit drei leuchtenden Kugeln gezeigt, wobei die Ergebnisse gegen Thermoelementmessungen validiert werden. Allerdings gelten rein experimentelle Messungen nur für regelmäßige Festbette, während die praktische Situation in der Regel unregelmäßig ist. Daher wird eine Ray-Tracing-Simulation durchgeführt, und die Ergebnisse zeigen,

dass ihre Kombination mit der Phosphor-Thermometrie den Messprozess erheblich vereinfachen kann und gleichzeitig Anpassungsfähigkeit für die Temperaturmessung in unregelmäßigen Festbetten bietet. Diese Arbeit trägt zur Entwicklung fortschrittlicher Temperaturmessmethoden in Fest-Fluid-Systemen bei und bildet eine solide Grundlage für die Verkleinerung des Messmaßstabs und der Optimierung von CFD-Simulation.

Contents

| | |
|--|------------|
| List of Figures | xii |
| List of tables | xix |
| 1 Introduction | 1 |
| 1.1 Non-linear regression analysis concept to measure temperature near solid walls | 4 |
| 1.2 Linear regression analysis concept for packed beds internal thermometry | 6 |
| 1.3 Structure of this thesis | 9 |
| 2 Thermometry techniques in solid-fluid systems: packed beds and thermal boundary layer | 11 |
| 2.1 High spatial resolution thermometry applicable to thermal boundary layers | 12 |
| 2.1.1 Micro-thermistors | 12 |
| 2.1.2 Rayleigh scattering thermometry | 13 |
| 2.1.3 Coherent anti-Stokes Raman spectroscopy (CARS) | 15 |
| 2.1.4 Planar laser-induced fluorescence (LIF) | 17 |
| 2.1.5 Microfluidics fluorescence thermometry techniques | 18 |
| 2.2 Measurements of packed bed internal temperature | 20 |
| 2.3 Phosphor themometry | 23 |
| 3 Imaging strategies for implementing ratio-based thermometry | 28 |
| 3.1 Principle of the intensity ratio determination | 29 |

CONTENTS

| | | |
|----------|--|-----------|
| 3.1.1 | Spectral separation method | 29 |
| 3.1.2 | Dual-frame lifetime method | 30 |
| 3.2 | Imaging of individual particles dispersed in transparent fluids | 32 |
| 3.2.1 | Two-color imaging applying the spectral separation method | 33 |
| 3.2.1.1 | Configuration with beamsplitter | 33 |
| 3.2.1.2 | Configuration with opposite camera setting | 35 |
| 3.2.2 | Temporally-separated dual-frame imaging | 36 |
| 3.3 | Imaging of luminescent particles in a porous structure composed of millimeter-sized solid particles | 37 |
| 4 | Image processing and data evaluation | 40 |
| 4.1 | Temperature and position determination of individual dispersed particles | 41 |
| 4.1.1 | Theory of the concept | 41 |
| 4.1.2 | Particles detection and localization | 44 |
| 4.1.3 | Particle image fitting | 45 |
| 4.1.4 | Misalignment correction between spectrally separated images | 50 |
| 4.1.5 | Intensity ratio calculation, corrections and conversion to temper- ature | 51 |
| 4.1.6 | Particle positioning accuracy | 52 |
| 4.2 | Temperature determination of luminescent particles in an opaque packed bed | 54 |
| 4.2.1 | Case of a single luminescent sphere | 54 |
| 4.2.2 | Extension to multiple luminescent spheres case | 55 |
| 4.2.2.1 | Separation of spatial and temperature variables in single sphere images | 56 |
| 4.2.2.2 | Linear regression to separate contributions from multiple luminescent spheres | 57 |

| | | |
|----------|--|-----------|
| 5 | Demonstration of high spatial resolution temperature measurements in fluid flows based on individual dispersed particle imaging | 60 |
| 5.1 | Experiments applying the spectral separation method | 61 |
| 5.1.1 | Choice of thermographic phosphor particles | 61 |
| 5.1.2 | Preliminary demonstration of liquid dispersions | 64 |
| 5.1.2.1 | Experimental setup | 64 |
| 5.1.2.2 | Results | 65 |
| 5.1.3 | Rejection of multiple scattering interference | 67 |
| 5.1.3.1 | Experimental setup | 67 |
| 5.1.3.2 | Results | 70 |
| 5.1.4 | Temperature measurements within thermal boundary layers . . . | 73 |
| 5.1.4.1 | Experimental setup | 73 |
| 5.1.4.2 | Results | 75 |
| 5.1.5 | Analysis of ratio precision for different systems | 82 |
| 5.2 | Test cases using the dual-frame lifetime method | 86 |
| 5.2.1 | Thermographic phosphor particles investigated | 87 |
| 5.2.2 | Experimental setup | 90 |
| 5.2.3 | Results | 92 |
| 6 | Multi-point temperature reconstruction in opaque packed beds | 94 |
| 6.1 | Thermographic phosphor particles selection | 95 |
| 6.2 | Design of the packed bed | 95 |
| 6.3 | Optical setup | 97 |
| 6.4 | Calibration and assessment of position independence of the phosphor thermometry method | 99 |
| 6.5 | Demonstration of three spheres instantaneous thermometry | 102 |
| 6.5.1 | Experimental results | 102 |
| 6.5.2 | Analysis of combination with ray tracing simulations | 104 |

CONTENTS

| | | |
|----------|--|------------|
| 6.5.2.1 | Comparison of measured and simulated intensity distributions | 105 |
| 6.5.2.2 | Application in the demonstration case | 105 |
| 6.5.2.3 | Limits of reconstruction and its a priori estimation | 107 |
| 7 | Conclusions and Future Works | 110 |
| 7.1 | Imaging of individual dispersed particle for high spatial resolution thermometry in fluids | 111 |
| 7.1.1 | Summary of the works | 111 |
| 7.1.2 | Application in cooling film thermometry | 112 |
| 7.1.3 | Application in thermometry in the preheated zone of a flame . . . | 113 |
| 7.1.4 | Future works | 114 |
| 7.2 | Determination of temperature distribution within opaque packed beds . | 118 |
| 7.2.1 | Summary of the works | 118 |
| 7.2.2 | Future Works | 119 |
| | Reference | 123 |
| | Publications list | 140 |

List of Figures

| | | |
|-----|--|----|
| 2.1 | Intensity ratio thermometry technique to measure the instantaneous temperature evolution wake of a heated cylinder, reproduced from ABRAM et al. (2013) | 25 |
| 3.1 | Normalised luminescence emission spectra of tin-doped phosphor $(\text{Sr,Mg})_3(\text{PO}_4)_2:\text{Sn}^{2+}$ from 300 to 900 K in furnace superimposed with the filter transmission curves of BG18 and RG645 (both from SCHOTT), and the derived ratios as a function of temperature. The spectra data is obtained from FOND et al. (2019). | 29 |
| 3.2 | (a) Data of YAG:Cr ³⁺ lifetime versus temperature from Lopez-Bonilla et al. LOPEZ-BONILLA et al. (2023). (b) The time sequences of the optical devices for implementing the dual-frame 2D lifetime determination. F_1 and F_2 are the frame numbers. | 31 |
| 3.3 | Two-color configuration of beamsplitter arrangement to enable spectrally separated Imaging of individual dispersed particles. | 33 |
| 3.4 | Example particle images obtained with different optical setup arrangements: thin beamsplitter, high flatness beamsplitter, pellicle beamsplitter and no beamsplitter (cameras on opposite sides). This figure is reproduced from XUAN et al. (2023). | 35 |
| 3.5 | Two-color configuration with opposite camera setting to enable spectrally separated Imaging of individual dispersed particles. | 36 |
| 3.6 | Single camera configuration to enable temporally separated Imaging of individual dispersed particles. | 37 |

LIST OF FIGURES

| | | |
|-----|---|----|
| 3.7 | Schematic of the configuration implementing dual-frame lifetime method to indirectly image luminescence originating inside an opaque scattering media of large solid particles. | 38 |
| 4.1 | Illustration of the particle point spread function fitting: (a) raw particle image and (b) the corresponding 2D Gaussian fit image. This figure is reproduced from XUAN et al. (2023). | 42 |
| 4.2 | Illustration of particle image processing. (a) Raw image in one recording channel; (b) corresponding fitting and (c) derived intensity ratios. This figure is reproduced from XUAN et al. (2023). | 43 |
| 4.3 | Image processing steps to locate particles: a) raw image b) local maximums c) gradient filter d) detected particle positions. This figure is reproduced from XUAN et al. (2023). | 44 |
| 4.4 | Particle fit example, reproduced from XUAN et al. (2023). | 47 |
| 4.5 | Fitting for astigmatic particle images. a) raw particle image; b) result of general Gaussian fit; c) result of rotated Gaussian fit. This figure is reproduced from XUAN et al. (2023). | 48 |
| 4.6 | (a) Synthetic particles images based on 2D rotate Gaussian; (b) Significantly rotated particles simulating the strong astigmatism in the near edge region; (c) Highly Gaussian-like images with negligible astigmatism in the center region. | 53 |
| 4.7 | Fitted center residuals in x and y direction and of the composite vector obtained for virtual particle images | 54 |
| 4.8 | A background-subtracted recorded image when a luminescent sphere is located at the packing center. The white rectangle denotes an intensity-masked region inside which only analysis occurs. This figure is reproduced from XUAN et al. (2024). | 55 |

LIST OF FIGURES

4.9 (a)-(c) The normalized images of individual signals of the spheres S1-S3 in configuration (d). (e) The compound signals of the three luminescent spheres and (f) the corresponding fitting. All the recorded images are the first one out of the frame pair. This figure is reproduced from XUAN et al. (2024). 56

5.1 Normalized spectra of 2 μm SMP:Sn²⁺ particles dispersed in water from 32 to 63 °C, superimposed with the filter transmission curves used in this study. This figure is reproduced from XUAN et al. (2023). 62

5.2 Normalized spectra of ZnO in the gas phase from 293 to 483 K, plotted with the filter transmission curves used in this study. The temperature interval between curves is 15 K. This figure is reproduced from ABRAM et al. (2015). 63

5.3 Optical setup for high-resolution particle imaging in liquid-phosphor particle dispersions, reproduced from XUAN et al. (2023). 64

5.4 Ratio calibration curves for the phosphor SMP:Sn²⁺ in liquid dispersions: measured intensity ratios obtained from 2D particle image fitting; the theoretical ratios derived from spectral convolution of emission spectra, filters transmission in both channels and beamsplitter transmission/reflection ratio. This figure is reproduced from XUAN et al. (2023). 66

5.5 Picture and schematic of the optical setup used to test the effect of re-scattered LED emission. 67

5.6 The applied LED lamp and its controller. These two figures are reproduced from <https://www.thorlabs.de/>. 68

5.7 (a) Emission spectrum of interfering LED plotted together with the filter transmission curves and SMP:Sn²⁺ emission spectrum at 300 K. (b) An example of the single particle image with LED on and off recorded in the BG18 channel, after subtracting the LED background (unseeded flow, LED on). This figure is reproduced from XUAN et al. (2023). 69

LIST OF FIGURES

5.8 Contribution of re-scattered LED emission at different LED output level power, reproduced from XUAN et al. (2023). 70

5.9 Ratio maps obtained from the single particle fit technique and the conventional method (window-based) for different LED output powers (a) 0mW, (b) 22mW (0.2A input), (c) 67mW (0.4A input), (d) 114mW (0.6A input), (e) 297mW (0.8A input), and (f) 840mW (1A input). This figure is reproduced from XUAN et al. (2023). 71

5.10 Single particle intensity ratios distribution with LED off and at maximum power based on (a) the single particle fit technique and (b) the window-based method. This figure is reproduced from XUAN et al. (2023). 73

5.11 Side view of the optical setups for resolving temperature profile in a thermal boundary layer. 74

5.12 (a) Raw particle image of flow in the boundary layer experiments. The processed sub-region is indicated by red dashed rectangles that is 3 pixels away from the detected wall; (b) an example of near-wall particle frame pair and their fitting results. The gray regions are the discarded input data in the fitting. This figure is reproduced from XUAN et al. (2023). 76

5.13 ZnO temperature - ratio calibration curve, obtained from Ref. ABRAM et al. (2015) and from the present study. Both data sets are fitted by power law functions of the form $a + b \cdot IR^c$, with IR the normalized intensity ratio. This figure is reproduced from XUAN et al. (2023). 77

5.14 Single shot temperature field: (a) the full processed area and (b) a subset of the near-wall domain. The theoretical thermal boundary layer thickness is also plotted in red dashed line. This figure is reproduced from XUAN et al. (2023). 78

5.15 A zoom-in view of the three temperature measurements located in the marked rectangle in the upper left corner of Fig. 5.14(b) 79

LIST OF FIGURES

5.16 Temperature field obtained from accumulated measurements: (a) the full processed area and (b) a subset of the near-wall domain. The theoretical extent of the thermal boundary layer is also plotted as the red dashed line. This figure is reproduced from XUAN et al. (2023). 80

5.17 Comparison of the temperature profile in the thermal boundary obtained from this single particle fit thermometry technique and calculated using the laminar Prandtl-Blasius equation. This figure is reproduced from XUAN et al. (2023). 82

5.18 Emission decay time ($1/e$) of SMP:Sn²⁺ after 266nm excitation over the 300-900 K range, reproduced from FOND et al. (2019). 87

5.19 Lifetime as a function of temperature for ScVO₄:1%Bi, YVO₄:1%Bi and Y_{0.6}Sc_{0.4}VO₄:1%Bi excited by 266nm laser. This figure is reproduced from RASHED (2022). 88

5.20 Radiative lifetimes of ⁵D₀ level of Eu³⁺ of Y₂O₃ with 3 %, 1 % and 0.1 %, and YVO₄ doped with 1 % concentration of Eu³⁺, on the temperature range from 40 °C to 460 °C. This figure is reproduced from ĆIRIĆ et al. (2020). 89

5.21 Optical setup to acquire temporal separation intensity ratios for high-resolution particle imaging in liquid dispersion. 90

5.22 Intensity ratios distribution of four tested phosphor particles obtained from the dual-frame lifetime method at room temperature. (a) tin-doped phosphor particles, SMP:Sn²⁺; (b) YVO₄:1%Bi particles; (c) Y_{0.6}Sc_{0.4}VO₄:1%Bi particles; (d) Y₂O₃:Eu³⁺ particles. 92

6.1 (a) Regular packing coordination system; (b), (c) and (d) are the examples of location indices of the red-colored spheres. This figure is reproduced from XUAN et al. (2024). 96

LIST OF FIGURES

| | | |
|-----|--|-----|
| 6.2 | (a) Setup for optical thermometry and. (b) Photograph of packing with heating element and thermocouple. This figure is reproduced from XUAN et al. (2024). | 98 |
| 6.3 | The intensity ratios measured at four locations of the luminescent spheres inside the packing, over the 27 – 150 °C temperature range. Exponential fit curves are used for ratio to temperature conversion and to guide the eye. | 100 |
| 6.4 | Repeated temperature measurements for single luminescent sphere placed at 13 different locations separately in the packing under isothermal condition (25 °C). This figure is reproduced from XUAN et al. (2024). | 101 |
| 6.5 | Temperature-time traces using linear regression fit to isolate the multiple spheres signals into individual contributions based on measured $S^{(j)}(x, y)$ templates. The temperature of all the spheres except S3 were measured by thermocouple (TC) simultaneously, but the thermocouple readings for S1 is from a separate measurement, denoted by the asterisk exponent. This figure is reproduced from XUAN et al. (2024). | 102 |
| 6.6 | (a) Comparison between recorded and simulated image of luminescent light formed on the camera when a luminescent sphere is located at the center of the packing. (b) Normalized intensity plot of the data region indicated by the red dash line in (a). The intensities from the two approaches are normalized to the their respective maximum intensities. This figure is reproduced from XUAN et al. (2024). | 106 |
| 6.7 | Temperature histories measurement for the three luminescent spheres case described in Section. 6.5.1, but using simulated spatial intensity distribution function $S^{(j)}(x, y)$ for signal separation. This figure is reproduced from XUAN et al. (2024). | 108 |
| 7.1 | overlap particle | 115 |

LIST OF FIGURES

- 7.2 Center: micro-CT scan of irregular packing with larger number of spheres and 6 colour-marked luminescent spheres; left, right: single-particle simulated images for two different spheres. This figure is reproduced from Fig. 15 in XUAN et al. (2024). 122

List of Tables

| | | |
|-----|--|-----|
| 4.1 | Results of the fitted single particle image example | 47 |
| 5.1 | The particle-to-particle standard deviation in ratios with SMP:Sn ²⁺ particles seeded in the gas for two optical configurations at room temperature. Of the two, the pellicle beamsplitter configuration is also tested using different filters combinations or even without filters. | 83 |
| 5.2 | The particle-to-particle standard deviation in ratios for the two applied phosphors dispersed in gas and water at room temperature | 85 |
| 6.1 | Condition number and fitting errors of the linear regression fit for measured and simulated spatial intensity distribution functions $S^{(j)}(x, y)$, for the sphere arrangement shown in Section. 6.5.1. In the table, F_1 and F_2 indicated the results of the two frames used for the temperature determination. | 109 |



Introduction

As minute as chemical reactions within cells or as vast as the wind current on Earth's surface, heat transfer phenomena are ubiquitous in daily life. The investigation of complex heat transfer consequently has received considerable attention from researchers who continually dedicate themselves to better understanding it. In particular, resolving the complex heat transfer in solid-fluid particle systems by experimental methods is crucial to the development of new energy efficient chemical processes involving combustion, pyrolysis, and catalysis (TOSCANO et al., 2022; LI et al., 2023). One of the important ways, or even the most important, to gain insight into heat transfer is to obtain the temperatures in the system. However, in many thermochemical processes, traditional thermometry methods with physical probes such as thermocouples may generate additional measurement uncertainties. For example, in microwave reactors, the physical probe has the potential to couple with the microwave radiation, which causes erroneous temperature readings due to the induced currents in it (GANGURDE et al., 2017; SIDDIQUE und SALEMA, 2023; GARCÍA-BAÑOS et al., 2019). In the plasma reactor, the material of the physical probe might react with the plasma, especially at high temperatures, leading to degradation or contamination of the plasma (PIEJAK et al., 1998). In the flow sub-region such as the thermal boundary layer, the intrusiveness

of the physical probe would extensively perturb the flow as the probe size is relatively large compared to the extremely thin boundary layer (ZHAO et al., 2019), and it can bias the temperature profile in the layer since it would act as a heat sink that absorbs or releases heat (BECK und HURWICZ, 1960). Because of those limitations, alternative methods of optical diagnostics, are particularly attractive as they do not disturb the system and are not affected by the aggressive environment in the same way a physical probe might be.

Optical diagnostics refer to a set of techniques and methods that employ light to investigate, diagnose, and monitor various phenomena, primarily in the thermodynamics and biomedical field. A salient category within optical diagnostics is luminescence imaging. In traditional luminescence imaging methodologies, photons are generally emitted by the objects under study and then traverse directly to the camera. Luminescence signals collected on the imaged plane are subsequently interpreted on a pixel-to-pixel basis. Since the emissions of luminescence vary temporally or spectrally in response to temperature change, temperatures can be derived accordingly. In this way, luminescence imaging directly provides spatial insights as the investigated objects can be directly observed in the images. However, some cases necessitate temperature measurements inferred on indirect light paths. For instance, in-vivo temperature imaging typically applies fluorescent thermometers that emit temperature-dependent luminescence diffusing throughout the tissue (CHIHARA et al., 2019), enabling indirect temperature measurements at deeper levels within biological tissues.

When solid boundaries are present in the measurement systems, the main challenge in the application of luminescence imaging arises from the fact that the luminescence light is rescattered or reflected multiple times before reaching the detector. Such phenomena can bias the signals originating from luminescent entities, thereby perturbing the temperature readings and blurring the spatial information, as observed in the near wall region of luminescent particles seeded flows. In a highly scattering media where light paths are obscured or cannot be directly accessed, such as in packed

beds containing luminescent-coated particles, the inherent configuration prevents the use of traditional direct imaging methods, and leads to multiple reflections of luminescence before exiting the system. Consequently, determining the precise origin of luminescence in such case is of difficulty.

The phosphor thermometry technique is one of the luminescence imaging methods using solid luminescent phosphor particles, as local thermometers. Most of the phosphor particles, especially those designed for high-temperature applications, often possess high thermochemical stability, meaning that they do not degrade, decompose, or react easily when subjected to high temperatures or when exposed to potentially reactive chemicals. This ensures that their luminescent properties remain consistent and reliable under extreme conditions, which is crucial for accurate temperature measurements. Additionally, their luminescence can be spectrally or temporally filtered, allowing for the specific isolation of particle luminescence against other radiation sources. These characteristics enable the use of phosphor particles in a wide range of high-temperature and potentially reactive environments, by dispersing the particles into fluid or coating particles on the surface of objects.

This thesis develops and demonstrates two advanced phosphor thermometry concepts that exploit the luminescence emitted from discrete emitters to measure temperature distributions, despite the issues caused by the presence of solid boundaries. By analyzing luminescence images using linear and nonlinear regression approaches, the information of a discrete emitter is isolated from the light originating from other sources and extracted to infer temperature. In the first concept, luminescence images from particles seeded into the flow near solid-fluid interfaces are fitted with 2D Gaussian functions to obtain temperature data points extremely close to the solid-fluid interface ($< 50 \mu\text{m}$). In the second concept, selected particles in a packed bed assembly are coated with thermographic phosphors. The luminescence emitted from coated particles is imaged after multiple light reflections/scattering through the bed, and is

1.1. NON-LINEAR REGRESSION ANALYSIS CONCEPT TO MEASURE TEMPERATURE NEAR SOLID WALLS

analyzed to separate the contribution from each individual sphere in order to obtain multi-point temperature measurements.

1.1 Non-linear regression analysis concept to measure temperature near solid walls

Very near solid boundaries, a thermal boundary layer typically arises where heat is transferred between the solid surface and the surrounding fluid medium at a different temperature. Various factors, such as boundary conditions, fluid properties, surface roughness, flow regime, and irregularities in surface geometry including obstacles, can influence the intricacies of heat exchange within this layer. The aforementioned factors contribute to complexities in heat transfer analysis, manifesting in detailed phenomena including flow separation, the transition from laminar to turbulent flow regimes, and modifications in heat transfer efficiency, either enhancement or degradation. Gaining a comprehensive understanding and characterization of these complexities is vital to optimize thermal systems, analyze natural phenomena, and design effective heat exchange devices. This requires accurately determining temperature distribution within the thermal boundary layer. Though heat transfer simulation in flows can provide detailed spatial and temporal insights, they inherently contain uncertainties, which are often caused by the factors such as mathematical model approximations, difficulties in obtaining precise boundary conditions, and heterogeneities in material properties. Concurrently, with the rise in experimental techniques like Particle Image Velocimetry (PIV) and Laser Doppler Anemometry (LDA) for thermal flows, there was a growing emphasis on validating and verifying simulation methods against accurate experiment data.

The use of luminescence imaging to experimentally measure temperature in thermal boundary layers often suffers from moderate spatial resolution due to the typical

1.1. NON-LINEAR REGRESSION ANALYSIS CONCEPT TO MEASURE TEMPERATURE NEAR SOLID WALLS

spatial averaging effects (ABRAM et al., 2018). It is also susceptible to interfering lights from other sources, leading to additional uncertainties in the obtained results. To address these obstacles, researchers have been dedicating significant efforts to developing temperature measurement methods with a high spatial resolution for accurately resolving temperature gradients and distributions within thermal boundary layers. The proposed technique, using individual tracer particles as independently discrete detectors, aims at improving spatial resolution and simultaneously enabling the rejection of multiple scattering effects during temperature measurement.

The proposed concept builds upon imaging fields of particles as in thermographic particle image velocimetry, while treating the luminescence image of each particle individually. For this, the technique presented in the thesis leverages the high-resolution capabilities of the scientific CMOS camera combined with a macro lens to produce well-defined Gaussian-like images of the particles. The identical particles are anticipated to be imaged in two spectrally- or temporally-separated frames to enable the intensity ratio phosphor thermometry method. As a result, the intensity distribution in individual particle images can be approximated by the two-dimensional Gaussian function to derive total intensity for intensity ratio computation. In principle, by non-linear regression of the particle image, the particle image is able to be separated into two contributions: a 2D Gaussian distribution containing the particle intrinsic temperature information and a non-Gaussian contribution which is the low spatial frequency interference from the solid wall. This concept is expected to remain robust despite variations in particle center-pixel alignment from particle to particle and between the two frames of identical particles, while also allowing for the determination of sub-pixel particle locations to achieve an extremely high in-plane spatial resolution.

1.2 Linear regression analysis concept for packed beds internal thermometry

In the realm of industrial reactor systems, packed beds are the most common reactor for particle transformation processes, including drying, combustion, and catalytic reactions. A large number of applications involve packed bed reactors with particles of arbitrary shape (HORN, 2020) and the reactions there occur very often at high temperature. The measurement and control of the packing particle temperature in the beds are thus crucial to optimize product quality, the energy efficiency of the systems, and pollutant emissions.

Given the inherent randomness in the size and distribution of pores within a packed bed, coupled with the opacity of the packing material, the accurate measurement of the global temperature distribution inside the bed poses significant difficulty. Therefore, researchers and engineers frequently resort to numerical simulations to analyze the internal temperature characteristics of packed beds, which offers a means to overcome the limitations of direct measurements (CHEN et al., 2019; MA et al., 2023; BÉTTEGA et al., 2013). However, the numerical simulation of thermochemical processes in packed beds is also very challenging due to the large domain size, the multi-scale nature of the problem, and the different heat transfer modes that are presented, including convection, particle-to-particle conduction, and radiation.

Even in the absence of radiation, convection and chemical reactions, the simulation of heat transfer in packed beds remains particularly intricate due to the difficulty in resolving complex particle surface properties at contact points and also the variability inherent in the packing structure as a result of the particle filling step (BAHRAMI et al., 2006; BEAULIEU et al., 2021; BUONANNO et al., 2003; TSOTSAS und MARTIN, 1987; DAI et al., 2019). Notably, when dealing with particles of high thermal conductivity and regular geometries like cubes, surface roughness can significantly influence particle-

1.2. LINEAR REGRESSION ANALYSIS CONCEPT FOR PACKED BEDS INTERNAL THERMOMETRY

to-particle heat transfer (RODRIGUES et al., 2022; BEAULIEU et al., 2021). Although the implications of such roughness can theoretically be modeled by a minor air gap between particles (BEAULIEU et al., 2021; PICHLER et al., 2021; YANG und CAI, 2019; TSORY et al., 2013), effective simulation necessitates prior knowledge of this gap size which is often unattainable because of its various determinants such as particle manufacturing methods (RODRIGUES et al., 2022; DAI et al., 2019). It is therefore crucial to have accurate local temperature measurements within the packed bed, especially for multi-point measurements which can provide information on the direction and magnitude of heat transfer rates.

Based on the luminescence imaging methods, we developed a non-contact thermometry concept to experimentally measure the internal temperature of packed beds. This concept also builds upon the thermographic phosphor particle imaging as in the proposed concept above for resolving the thermal boundary layer. In phosphor thermometry, phosphor-coated surfaces (BRÜBACH et al., 2013) or phosphor particles seeded into the fluid flow (ABRAM et al., 2018) are directly illuminated by a laser source and imaged onto a point detector or a camera, but this requires transparency of the medium and a low amount of refraction for direct optical access to the probe location. In this thesis, we explore a method using temperature-sensitive phosphor and binder to coat some selected granules inside the packed bed. In this way, phosphor coatings can be excited indirectly as the laser propagates through the bed by scattering between packing granules surfaces. Consequently, the phosphor luminescence exiting the bed can be exploited to reconstruct the originating location and estimate the temperature at the reconstructed location.

When multiple luminescent particles are presented, the resulting luminescence field is a sum of the individual particle contributions. This thesis proposes to isolate the relative contributions of each particle by linear regression of their radiative transfer. For this, the key point is to obtain the individual particle intensity distribution functions, which provide the spatial distribution of the luminescence formed on the

1.2. LINEAR REGRESSION ANALYSIS CONCEPT FOR PACKED BEDS INTERNAL THERMOMETRY

camera image while only one of the internal particles is emitting light. In simple setups where the packing is regular and repeatable, these distribution functions can be measured experimentally. For complex cases of irregularly packed beds, we propose to obtain the functions using simulations where one can turn individual particles “on” and “off” more easily. The objective is to pave the way for multi-point temperature measurements in general laboratory-sized packed beds with arbitrarily shaped but known geometry so that allows one to obtain dense temperature fields through data assimilation that simulates the dense fields with the measurements as input boundary conditions.

Overall, two concepts for temperature measurement in solid-fluid systems are proposed. On one hand, the particle Gaussian fit approach resolves the sophisticated thermal dynamics near solid boundaries, which seeks to capture the minute details of temperature fluctuations on a single particle basis, thus affording a higher level of spatial resolution. On the other, the multi-particle luminescence separation method offers a pioneering solution to monitor and manage heat within densely packed beds – environments where unpredictability region.

This thesis threads together these seemingly disparate research areas, united by a common underpinning: the potential and versatility of utilizing the spatial discrete nature of single luminescence particles based on phosphor thermometry. Both proposed concepts represent significant strides in the ability to better interpret the temperatures in solid-fluid systems, paving the way for more efficient and sustainable thermochemical processes. Through these advanced concepts, the overall goal is to not only bridge the gap between experimental methods and computational simulations but also to foster a holistic understanding of temperature dynamics in varied environments.

1.3 Structure of this thesis

An overview of the 6 other chapters that compose the main content of this thesis is outlined here. This work focuses on exploiting the discrete nature of luminescence particles to measure the temperature within the thin thermal boundary layer with high spatial resolution, and to enable multi-point temperature detection inside a packed bed of opaque granules.

Chapter 2 briefly reviews the current state of thermometry techniques that can or might be employed to resolve the thermal boundary layer and to probe temperature inside packed beds. These techniques are broadly classified into contact and non-contact methods. Phosphor thermometry techniques, as the basis of the methods used in this thesis, are discussed in detail in this chapter.

Chapter 3 explains the principle of two methods, spectral separation method and dual-frame lifetime method, to obtain the luminescence intensity ratio of particles for ratiometric phosphor thermometry. This chapter introduces the optical configurations selected to implement both methods for imaging individual micron-sized particles dispersed in transparent fluids. Another case of imaging particles with luminescent coatings in highly scattering media consisting of large solid particles is also presented, associated with the optical configuration implementing the dual-frame lifetime method for this case.

Chapter 4 details the image processing to extract the intensity ratios of individual luminescence particles and thus derive their temperature (and spatial) information. When imaging micrometer-sized dispersed particles, the processing mainly involves applying 2D Gaussian fits to their individual luminescence images. On the other hand, for luminescence-coated spheres placed inside an opaque packed bed, the processing of extracting the temperature information from their indirectly recorded image is

described. Multi-point measurements are also addressed where several luminescence-coated spheres are presented inside the bed.

Chapter 5 presents some flow experiment setups that implement the individual particle image fit concept, and discusses the experimental results. The emphasis of the experiments is the temperature distribution measurement in a thin thermal boundary layer. In addition, the flow thermometry performance of some imaging configurations employing the spectral separation method is compared and analyzed.

Chapter 6 demonstrates the use of indirectly recorded images of luminescence-coated spheres in a regular opaque packed bed to achieve a single point or even a multi-point internal temperature detection. The possibility of extending the measurements to an irregular packed bed by combining the thermometry strategy with ray tracing simulation is also discussed.

Chapter 7 provides a comprehensive summary of the obtained results and corresponding conclusions, and offers insights into future prospects and plans for advancing the proposed technique.

2

Thermometry techniques in solid-fluid systems: packed beds and thermal boundary layer

Temperature measurement is a critical component in the study of solid-fluid systems, particularly those involving complex heat transfer processes. Various thermometry methods have been developed to enable the detection in solid-fluid systems where local temperature perturbations or measurement interfering lights frequently exhibit significant randomness. The reviews here are restricted to the methods that can potentially be implemented to measure temperature in packed beds or in thermal boundary layers, the two cases that are the focuses of the concepts presented in this thesis. This chapter first discusses the techniques applied in thermal boundary layer temperature measurement with high spatial resolution, which are mostly laser-based optical thermometry. The brief overview of temperature diagnostics applied to packed beds is provided in the second section of this chapter. Limitations are identified and we propose in this thesis to overcome them by developing novel concepts using the

2.1. HIGH SPATIAL RESOLUTION THERMOMETRY APPLICABLE TO THERMAL BOUNDARY LAYERS

phosphor thermometry technique. The work in this chapter is partly derived from the publications XUAN et al. (2023) and XUAN et al. (2024).

2.1 High spatial resolution thermometry applicable to thermal boundary layers

Measuring the temperature distribution in the near-wall region can provide validation data of CFD models aimed at simulating wall-to-fluid convective heat transfer, for example in the context of film cooling technologies for gas turbines (UNNIKRISHNAN und YANG, 2022; ACHARYA und KANANI, 2017). Compared to the velocity boundary layer which has been investigated by hot wire anemometers (KLEWICKI und FALCO, 1990) or laser velocimetry techniques such as Laser Doppler Velocimetry (LDV) (BAUER et al., 2019; YAO et al., 2016), Particle Tracking Velocimetry (PTV) (SCHNEIDERS et al., 2017; FUCHS2022 et al., 2022) or macro and micro Particle Image Velocimetry (PIV) (CUVIER et al., 2017; SHIMURA et al., 2019), there are much fewer observations on thermal boundary layers, as measurement techniques for flow thermometry are less mature, especially when applied near-walls. Various high spatial resolution techniques with the potential to measure temperature profiles in the thermal boundary layer are reviewed in the following.

2.1.1 Micro-thermistors

Micro-thermistors, also known as cold wire anemometers, have long been applied in measuring temperature distributions in thermal boundary layers (NAGANO und TSUJI, 1994). These sensors operate based on the change in electrical resistance of a probe as a function of temperature, allowing for precise temperature measurements.

2.1. HIGH SPATIAL RESOLUTION THERMOMETRY APPLICABLE TO THERMAL BOUNDARY LAYERS

PUITS et al. (2017) employed a micro-thermistor to investigate the near-wall temperature field in thermally driven convection at a rough surface within a large experimental facility named the "Barrel of Ilmena". They found that the heat flux enhancement generally observed at rough surfaces resulted from an increase in the local heat transfer coefficient at the top of the roughness elements. Likewise, HERTLEIN und DU PUIITS (2021) employed a combined probe of 4 micro-thermistors to resolve the temperature gradient in Rayleigh-Bénard convective boundary for thermal dissipation evaluation. Both studies achieved a temperature precision below 0.05 K but with a relatively long temperature response time on the order of 100 ms in the air due to the physical size of the thermistor, which is above 100 μm in diameter and 330-350 μm in length.

Smaller probes have also been developed for turbulent gas flows (YEH und ATTA, 1973; MYDLARSKI und WARHAFT, 1998), with probe diameters on micron order that can reach a fast response below 1 ms, allowing for instantaneous measurement even in oscillating flows (BERSON et al., 2010). As stated in the study by CLEVE et al. (2017), the authors applied a 3 μm diameter wire to measure temperature and velocity fluctuations close to the stack of a thermoacoustic refrigerator, demonstrating the possibility of measuring the enthalpy flux, which is a characteristic of thermal energy transfer in thermoacoustic devices. However micro cold wire anemometers are limited to single or several point measurements and the probe must be oriented to minimize the intrusiveness of the large support claws.

2.1.2 Rayleigh scattering thermometry

Laser-based optical diagnostics avoid local disturbances to the flow and offer the potential for high spatial/temporal resolution measurements. An example is Rayleigh thermometry, which is based on the phenomenon of Rayleigh scattering. This process involves the scattering of light or other electromagnetic radiation by atomic and molecular particles that have a size significantly smaller than the radiation wavelength, such

2.1. HIGH SPATIAL RESOLUTION THERMOMETRY APPLICABLE TO THERMAL BOUNDARY LAYERS

as the scattered sunlight by the nitrogen and oxygen molecules in the atmosphere, leading the sky to appear to have a blue color. Rayleigh scattering is elastic, meaning that the scattered radiation has the same wavelength as the incident radiation.

The intensity of the scattered light is proportional to the concentration of the particles, as well as the intensity of the incident light. Therefore, the Rayleigh scattering enables the determination of the temperature of the gas medium, since the molecule number density drops due to an elevation in temperature for fixed pressure, and so the Rayleigh scattering intensity reduces accordingly. This method is particularly useful for temperature measurements in turbulent flows, where contact-based thermometry techniques are often sensitive to local disturbances, or limited by their spatial resolution such as thermistors discussed above. With Rayleigh scattering thermometry, the spatial resolution of temperature measurements is typically on the order of a few hundreds of microns, but some researchers have been working on achieving a higher resolution.

FRANK und KAISER (2008) performed high resolution Rayleigh thermometry to probe dissipative structure in flames. The experiment used two high energy (>800 mJ/pulse) pulsed laser sheets overlapped into the near field of a turbulent jet flame resulting in a thickness of about $100\mu\text{m}$. An out-plane spatial resolution was thereby $100\mu\text{m}$ according to the laser thickness, and an in-plane resolution of $20\mu\text{m}$ was achieved using a combination of three imaging lenses.

KRISHNA et al. (2021) proposed the implementation of a high-speed filtered Rayleigh scattering (FRS) system to measure the temperature profile of premixed flames in a millimeter-scale channels. An iodine cell was added in front of the camera as a molecular filter, compared to the conventional Rayleigh thermometry. In the experiment, the laser frequency was tuned to the iodine absorption line, which suppressed the surface scattering to enable FRS in near wall measurement. The FRS systems provided a direct mapping from the measured signal to temperature, with a precision about 3% at temperatures above 1500 K and a spatial resolution of about $200\mu\text{m}$. By combining

2.1. HIGH SPATIAL RESOLUTION THERMOMETRY APPLICABLE TO THERMAL BOUNDARY LAYERS

FRS thermometry with stereoscopic particle image velocimetry (sPIV), MCMANUS et al. (2020) carried out an experimental approach to quantitatively measure temperature and three-component velocity in turbulent non-premixed jet flames simultaneously. Their experimental protocol provided detailed statistical assessment and accurate determination of thermal gradient, dissipation rates, and fluid flow interactions with temperature fields. In their study, the in-plane spatial resolution of temperature measurement was estimated to be $186\mu\text{m}$, while the out-of-plane spatial resolution was found to be about $129\mu\text{m}$ determined by the laser sheet thickness.

When employed to near wall measurements, traditional Rayleigh thermometry often has limitations because of the interfering signal caused by surface scatterings. Though FRS method offers a solution to this problem, its application commonly involves a complex optical setup including components of, for example, a wavelength monitor for measuring the frequency of the excitation laser and tuning the frequency to the desired absorption line of the molecular filter. In addition, in order to provide sufficient Rayleigh scattering signals for measurement, a high illumination energy is typically preferable in Rayleigh thermometry, thereby carrying a risk of damaging the optics. In the case of the FRS method, reaching a sufficient excitation energy necessitates a laser generator capable of temporally stretching the laser pulse. For this, the use of a long-pulse laser or a pulse-stretcher is required (KRISHNA et al., 2019), which can however further increase the complexity of the optical setup.

2.1.3 Coherent anti-Stokes Raman spectroscopy (CARS)

Coherent anti-Stokes Raman spectroscopy (CARS) is another molecular optical technique for temperature and species concentration measurements in various applications. CARS is an advancement of Raman spectroscopy that leverages inelastic spontaneous Raman scattering by illuminating a molecule with monochromatic light, such as a laser, leading to a change in the molecule's vibrational or rotational energy

2.1. HIGH SPATIAL RESOLUTION THERMOMETRY APPLICABLE TO THERMAL BOUNDARY LAYERS

level. This change prompts the molecule to emit light with a frequency shift relative to the illumination, allowing for identifying the vibrational modes of the measured molecule. However, the spontaneous Raman scattering, including Stokes Raman signal and anti-Stokes Raman signal, is often very weak due to a much higher possibility of elastic scattering occurring, i.e., Rayleigh scattering. Unlike the traditional Raman spectroscopy, CARS typically uses three synchronized lasers, a Stokes laser (frequency ω_s), a pump laser (frequency ω_p) and a probe laser (frequency ω_{pr} , often $\omega_{pr} = \omega_p$), to focus on the probe volume location, generating a CARS signal at the frequency of $\omega_{pr} + \omega_p - \omega_s$ in response to the probe laser. In CARS, the frequency difference between pump and Stokes lasers ($\omega_p - \omega_s$) is modulated to match the Raman-active vibrational frequency of the molecule, thus resonantly enhancing the CARS signal to orders of magnitude intenser than the spontaneous Raman signal. Since the CARS signal is nonlinearly related to the population of vibrationally excited state that follows the temperature-dependent Boltzmann distribution, it is applicable to gas phase thermometry by, for example, analyzing the spectra of CARS signals.

This technique can provide accurate point thermometry at sampling rates of up to a few kHz and can efficiently reject stray light for measurements near walls. Using CARS, KOSAKA et al. (2018) measured gas phase temperatures as close as $100\mu m$ to a temperature-controlled wall with a spatial resolution of $80\mu m$, as given by the diameter or the interaction volume at the intersection of the laser beams. KRISHNA et al. (2017) performed a CARS thermometry system on a wall-stabilized methane-air and ethylene-air flames at various strain rates, to measure temperatures as close as $275\mu m$ to the isothermal wall. Their measurement had an in-plane spatial resolution of $30\mu m$ with a dimension of $650\mu m$ in the laser propagation direction.

Extending to 1-D measurements, BOHLIN et al. (2015) implemented hybrid femtosecond/picosecond rotational CARS (HRCARS) to measure the temperature profile in a methane/air premixed flame, at Reynolds number 5000, impinging on a cooled steel surface. The authors achieved a 1D spatial resolution of about $60\mu m$, while mea-

2.1. HIGH SPATIAL RESOLUTION THERMOMETRY APPLICABLE TO THERMAL BOUNDARY LAYERS

surement depth was tuned to 1.5mm to enable the validation against the previous results from a point-wise CARS experiment. ESCOFET-MARTIN et al. (2021) and OJO et al. (2021) employed a consistent optical system to facilitate HRCARS for gaining insights in thermal boundary layers. They measured 1D transient near-wall temperature profiles in a chamber, where a $40\ \mu\text{m}$ spatial resolution at a wall-normal distance below $200\ \mu\text{m}$ with a precision of 3% of the absolute temperature could be achieved.

Though CARS has demonstrated a high in-plane resolution, mostly below $100\ \mu\text{m}$, the probe volume of CARS is typically elongated to more than $600\ \mu\text{m}$ in the laser propagation axis which can cause low path filtering if small-scale turbulent structures are present. In addition, CARS typically performs only point detection, and achieving 1-D measurements requires ultra-fast laser pulses on the order of femtoseconds or even picoseconds.

2.1.4 Planar laser-induced fluorescence (LIF)

Laser Induced Fluorescence (LIF) is also a molecule-based spectroscopic technique that uses a laser light to excite atom or molecule luminescent tracers, such as polycyclic aromatic hydrocarbons (e.g., toluene) or ketones (e.g., acetone) that are seeded as gas tracers for gas thermometry, or dyes dissolved in liquids for liquid thermometry. The tracers then emit light spontaneously with a frequency shift relative to the excitation light, enabling the removal of laser reflections using a spectral filter. In some cases, the use of a two-line LIF approach involving two different laser excitation wavelengths is also possible for simultaneous imaging of temperature and species concentration (KOEGL et al., 2020). By analyzing the thermal-dependent characteristics of the emitted light, generally the fluorescent intensity or the spectral distribution, the temperature of the system can be determined.

Planar LIF, as a specialized form of LIF, uses a laser sheet to illuminate the sample of interest, thereby capable of two-dimensional temperature imaging. It has been

2.1. HIGH SPATIAL RESOLUTION THERMOMETRY APPLICABLE TO THERMAL BOUNDARY LAYERS

utilized in numerous studies to accurately measure temperatures near walls or in large gradient regions owing to its advantages, such as selective excitation to match the absorption peak of target species. BANKS et al. (2019) employed planar LIF to observe the temperature in a thermal boundary layer on the cuvette wall due to spot heating, and measure the temperature field around laser-induced cavitation bubbles, without disturbing the bubble dynamics. The authors achieved an in-plane spatial resolution of $90 \times 200 \mu\text{m}$ with a maximum temperature uncertainty of $\pm 17 \text{ }^\circ\text{C}$ and an average uncertainty of $\pm 7 \text{ }^\circ\text{C}$ over $25 - 85 \text{ }^\circ\text{C}$. In addition, toluene-based planar LIF was frequently implemented to measure the temperature stratification near walls through the thermometry strategy of one-color detection or two-color detection. The former strategy extracts the temperature information from the spectrally integrated fluorescence signals, while the latter relies on the temperature-dependent ratio of two spectral bands. The applications of toluene-based planar LIF has been reported in an optical engine (PETERSON et al., 2014), a shock tube (YOO et al., 2011), and an impacting jet (JAINSKI et al., 2014). In these studies, in-plane spatial resolutions on the order of $100 \mu\text{m}$ were achieved, limited by the resolution of the intensifier microchannel plate and the smoothing steps performed on the image for noise reduction. On the other hand, the laser sheet thicknesses were in the range of $500\text{-}700 \mu\text{m}$ which also limits the spatial resolution in the third direction.

2.1.5 Microfluidics fluorescence thermometry techniques

In microfluidics, a high level of spatial resolution in temperature measurements can be achieved by fluorescence microscopy techniques. Those techniques typically use fluorescent dyes or molecular species as temperature tracers, thus allowing for a thermometry mechanism similar to that in the Planar laser-induced fluorescence.

An example is the widefield fluorescence microscopy. In contrast with confocal microscopy which uses a pinhole configuration to focus the excitation laser on the point

2.1. HIGH SPATIAL RESOLUTION THERMOMETRY APPLICABLE TO THERMAL BOUNDARY LAYERS

of interest and scans the laser to access different regions, widefield fluorescence microscopy exposes the entire sample to the excitation light, generating a luminescence image that can be viewed via eyepieces or on a digital camera-connected monitor for 2D temperature imaging. ROSS et al. (2001) exploited the temperature-dependent fluorescence of Rhodamine to demonstrate temperature measurements in microfluidic systems affected by Joule heating. A temperature field was successfully resolved in a $70\mu m$ wide liquid channel, with an in-plane spatial resolution of $1\mu m$ and an out-of-plane resolution determined by the $30\mu m$ channel height.

In contrast with the widefield fluorescence microscopy, total internal reflection fluorescence (TIRF) microscopy exploits the confined evanescent wave to selectively illuminate and excite fluorophores in a very thin layer of the specimen, usually a few hundred nanometers, immediately adjacent to a solid-liquid interface (AXELROD D, 1983). This means it has the potential to limit the measurement volume depth to very near the wall. As such, TIRF imaging of a suspension of quantum dots (nanometer-sized single fluorophores) in a solution also containing Rhodamine dye was proposed for thermometry and velocimetry within 200 nm of the wall with an uncertainty of about 5K (GUASTO und BREUER, 2008). It should be noted that here the Rhodamine was used as a reference dye, and the fluid temperature is derived from the two-color imaging, which is based on the temperature calibration curve of the ratio of the quantum dots fluorescence intensity to the Rhodamine fluorescence intensity.

Microcapsules doped with encapsulating fluorescence dyes were also reported for temperature measurement in liquid microfluidics (SOMEYA, 2021; VOGT und STEPHAN, 2012). Such tracers are generally in the 5-15 μm range with a density close to that of the fluid, offering the advantages of size control. In addition, when combined with Astigmatic Particle Tracking Velocimetry (APTV) method (CIERPKA et al., 2010a), seeding luminescent particles instead of using dissolved dyes allows a 3D positioning of the particles, enabling measurement resolution better than a few microns in all three directions CIERPKA et al. (2010b). MASSING et al. (2018) implemented this concept

with the tracer particles of encapsulated europium chelate to probe temperature based on lifetime imaging by a high-speed camera, simultaneously achieving 3D thermometry and velocimetry in their research. Similar to the work (GUASTO und BREUER, 2008) mentioned previously, here the author also applied the two-color imaging to perform temperature measurement, while the intensity ratio is obtained only from the europium chelate luminescence by temporally separating it.

These microscopic techniques are primarily constrained to near-field applications, offering a limited observation only at millimeter scale or even lower. While long distance microscopes can be used to achieve a longer working distance, they typically come with a larger f-number, which tends to diminish light-gathering ability and spatial resolution. This thesis aims to explore techniques capable of providing a broader application spectrum in macroscopic fields, thereby serving as a complement to the aforementioned near-field techniques.

Various techniques potentially available for measuring temperature distributions near the wall have been discussed. The next section will present another key focus of this thesis, involving the methods and challenges related to temperature detection inside opaque packed beds.

2.2 Measurements of packed bed internal temperature

Temperature measurements inside packed beds are key for process control, safety, and understanding of the phenomena occurring within the beds. Different contact measurement techniques to access internal particle temperatures of packed beds exist in the literature. Thermocouples are often used (THOMÉO et al., 2004) by placing thermocouples either directly in packed beds, or inside a thermowell which normally is a protective metal tube vertically/horizontally inserted in packed beds to lead and protect the thermocouples. YANG und CAI (2019) employed twelve K-type thermocouples to measure the temperature of the molten salt in a thermocline storage system

2.2. MEASUREMENTS OF PACKED BED INTERNAL TEMPERATURE

packed with sensible heat material and phase change material. The temperature in the system was in the range of 200-350°C, and the authors achieved a precision of 0.3°C. ROUSSEAU et al. (2014) used various types of thermocouples to measure temperature distributions and gradients along the radius direction in a pebble bed. The thermocouples were embedded at different levels within the bed, with three sets of thermocouples spaced at 120° intervals around the circumference for each level. The repeatability of the measurement was demonstrated over the range of 100-1200°C, with a maximum temperature variation of 10.5°C. In the study carried out by DE BEER et al. (2018), the thermocouple wires were led through drilled spheres of the packing, and the junction inserted into a target sphere at temperatures of up to 800°C. The temperature distribution in packed beds was obtained, with a precision better than 5°C, to infer the local temperature gradient, which is required to determine the effective thermal conductivity of packed beds. Some other studies using thermocouples to estimate the effective thermal conductivity in packed beds are reviewed in DÍAZ-HERAS et al. (2020). Though these works showed good temperature precision of thermocouple measurements in packed beds, the presence of metals prevents its application in environments where plasma, microwave heating or electric resistance heating is applied. In addition their readings are sensitive to electromagnetic interference (BLAIR und BENNETT, 1987), magnetic fields (KOLLIE et al., 1977) and thermocouples can be damaged by ionizing radiations (SPOSITO et al., 2021).

Instead, for harsh process conditions, such as high pressure or corrosion, methods based on thermochemically inert optical fibers could be used. An instance of this is the use of phosphor-tipped fibers, wherein a special coating of phosphors is applied on the end of the fiber for sensing and excitation purposes. When light is transmitted through the fiber, it excites the phosphor which then emits light at a different spectral range from the excitation depending on the temperature, enabling the temperature determination through a process called phosphor thermometry. The details of phosphor thermometry will be discussed later in Section. 2.3. A measurement originating from

2.2. MEASUREMENTS OF PACKED BED INTERNAL TEMPERATURE

the phosphor-tipped fiber was carried out by SPOSITO et al. (2021), who developed an hybrid fiber-optic phosphor thermometer to place inside a nuclear fuel waste canister to detect the temperature in the range of 20 to 220°C, achieving an uncertainty below 0.5°C. In another study (BAO und CHEN, 2012), temperature measurements based on distributed fibers using time of flight Brillouin Rayleigh or Raman Reflectrometry were reviewed, with a focus on the spatial resolution and the limitations on sensing length. However, for the mentioned cases, the use of fibers restricts the temperature range to below 600 °C and their transmission may degrade, for example when subject to radiation (PISANI et al., 2022).

With contact-based techniques for temperature measurements, the heat transfer between the probe, the packing particles, and the fluidized flow must also be considered. In addition, the fiber or thermocouple wires require appropriate sealing, careful positioning, and may create additional heat transfer modes in the bed. Non-contact techniques avoid the above problems. Nevertheless, the geometry of the packing prevents the direct use of optical techniques. Although transparent particles is able to restore optical access, the multiple particle/gas interfaces cause severe beam steering and multiple reflections. The use of transparent particles and liquid with matching refractive index, for example with glycerol/water mixtures, can avoid reflection and distortion (WU und MIRBOD, 2018). But the fluid/particle system allows in this case only fluid mechanical or mixing studies in cold non-reactive flows. For fluids containing both liquid and gas, refractive index matching is often not applicable. The behavior of a gaseous system can be simulated by a liquid system via scaling the properties and conditions of the liquid system, such as the fluid velocity and fluid properties (like viscosity and thermal conductivity), until their dimensionless numbers match. However, one can easily find that it is not possible to maintain those dimensionless numbers match due to large differences in transport properties of, for example, density and conductivity. Alternatively, X-ray thermometry has also been applied (DUNNMON et al., 2017) to measure gas phase temperature distribution in a porous media burner

using a mixture containing krypton, but this does not provide direct information about the packing particle temperatures.

Unlike using phosphor-tipped fibers, we propose in this thesis a non-contact approach for measuring the temperature based on phosphor-coated packing particles inside packed beds, by exploiting the temperature-dependent property of phosphors emission decay. Upon incident excitation light, phosphor-coated particles emit frequency-shifted luminescence that depends on temperature. The coating has high thermochemical stability and is applicable for measurements over a wide range of temperatures from cryogenic to 1700K (ALDÉN et al., 2010). In addition, the luminescence of many phosphors is insensitive to the surrounding gas composition or pressure (ABRAM et al., 2018), or the presence of a high magnetic field or electromagnetic interference (LOWE et al., 2022). Owing to its robustness, phosphor particles were used to measure on a burning coke particle (CAI et al., 2021), on a burning fiberboard OMRANE et al. (2002), and in a methanation catalytic reactor (GEITENBEEK et al., 2018). Since the packing particles are opaque, the concept we proposed uses indirect excitation and detection of phosphor-coated particles, allowing temperature probes at multiple locations simultaneously in an opaque packed bed without the need for optical fibers.

2.3 Phosphor themometry

Phosphor thermometry is a non-contact optical method for surface and fluid temperature measurement. This method uses inorganic phosphor particles as temperature-sensitive luminescent particles to obtain temperature information (SOMEYA et al., 2011b; FOND et al., 2012; CAI et al., 2022), and even flow velocity information at the same time, as reviewed in Refs. (ABRAM et al., 2018; SOMEYA, 2021). The velocity information can be derived using Particle Image Velocimetry or Particle Tracking Velocimetry approach, by analyzing either particle images in luminescence emission (GUASTO und BREUER, 2008; SOMEYA et al., 2011a,b; FAN und HOCHGREB, 2019) or in

2.3. PHOSPHOR THERMOMETRY

Mie scattered light (FOND et al., 2012; SCHREIVOGEL et al., 2016; STRAUSSWALD et al., 2021).

To detect temperature, inorganic phosphor particles are employed in a concept called thermographic PIV or aerosol phosphor thermometry, which has been applied in a variety of flows spanning a wide temperature range, typically from 200 to 900 K (ABRAM et al., 2018) and in a recent study even up to ~ 1400 K (HERZOG et al., 2021). Upon excitation by UV or visible light, the luminescence properties of phosphor particles vary with temperature; for example, the particle emission spectrum can shift with temperature or the decay time of the luminescence is normally decreased with temperature rise. Aerosol phosphor thermometry exploits those properties by seeding micron-size phosphor particles into fluids as tracers, especially in turbulent gas flows, which involve short flow time scales and a low thermal conductivity of the medium that is more likely to cause non-uniform temperature. The response time of $2\ \mu\text{m}$ size phosphor particles is typically below $50\ \mu\text{s}$ in air (ABRAM et al., 2018), allowing to rapidly follow temperature changes. In general, the temperature is inferred from probing either the temporal or spectral characteristics of phosphor luminescence emissions, referring to lifetime-based and two-colour spectrally separated methods, respectively.

In the lifetime-based approach, the luminescence emission decay is typically resolved with a high-speed camera (SOMEYA et al., 2011a,b) to determine the luminescent lifetime, which is a function of temperature. In a recent study (ABRAM et al., 2020), the luminescence emission decay of a short-lifetime phosphor was instead resolved by a global shutter camera that runs in dual-frame mode with a short ($< 1\ \mu\text{s}$) interframe time at 10 Hz. Consequently, the pixel-wise ratio of the recorded intensities between these two spectrally identical but temporally separated frames was also a function of temperature, and thus enabled the 2D measurement of the temperature field. With $2\ \mu\text{m}$ -size $\text{ScVO}_4:\text{Bi}^{3+}$, ABRAM et al. (2020) achieved a precision for instantaneous 2D measurements as high as 0.3 K over a 50 K temperature range with an in-plane spa-

2.3. PHOSPHOR THERMOMETRY

tial resolution of about $400\ \mu\text{m}$. This dual-frame lifetime-based method can enable ratio-based phosphor thermometry using only one camera, and offers a simple way to resolve the phosphor luminescence at a specific point, or even at multiple points, inside an opaque scattering media.

The two-colour spectrally separated method involves imaging particle luminescence using two distinct imaging detectors equipped with different spectral filters. Those filters are intentionally chosen to cover wavelength regions with different temperature behavior and to split the luminescence emission spectrum into two spectral bands, resulting in a temperature-sensitive and -dependent intensity ratio between the two bands (FOND et al., 2012; MASSING et al., 2016). To obtain temperature information, the luminescence intensity ratio can be derived either from groups of particles (e.g., when combined with PIV (FOND et al., 2012; SOMEYA et al., 2011a)) or from individual particles (e.g., when combined with PTV (MASSING et al., 2018; CAI et al., 2022; STELTER et al., 2023)). An example of luminescence image pair obtained when seeding particles to measure temperature in the rear wake of a heated cylinder is shown in Fig. 2.1, together with the resulting temperature field estimated from the intensity divisions of particle groups.

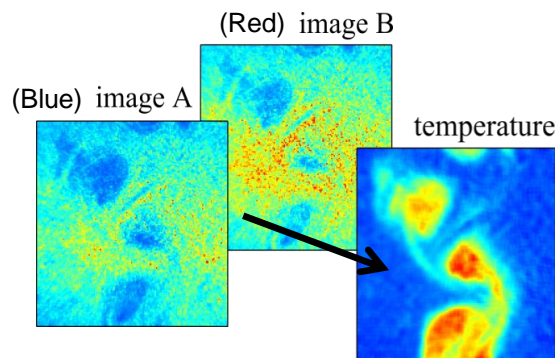


Figure 2.1: Intensity ratio thermometry technique to measure the instantaneous temperature evolution wake of a heated cylinder, reproduced from ABRAM et al. (2013)

In most previous applications of thermographic phosphors in gas flows, to the exception of OJO et al. (2015) and STELTER et al. (2023), the temperature informa-

tion is derived from groups of particles contained in averaging windows (typically of 10×10 pixels, above $200 \mu\text{m}$) that are divided to form temporal or spectral ratio images. However, when applied for temperature measurements in thin boundary layers, temperature gradients may be presented within the averaging window. In addition, strong luminescence from particles deposited on the wall may be re-scattered by the phosphor particle aerosol causing a near-wall signal interference (SCHREIVOGEL et al., 2016; ZENTGRAF et al., 2017). In the examples in Refs. (SCHREIVOGEL et al., 2016; STRAUSSWALD et al., 2021), the area within 3mm of the wall is clipped as the uncertainties in the near wall region would be too high. In experiments involving large seeded volume, re-scattered luminescence can also interfere with free stream measurements (VAN LIPZIG et al., 2013; LEE et al., 2016). This is because the out-of-focus particles can scatter the luminescence from the particles in the laser path, or can even be excited by the scattering excitation light, causing the detector to collect signals that do not originate from particles within the measurement plane. A possible solution to alleviate the scattering and reflection interference, structured laser illumination planar imaging (SLIPI), was proposed in Ref. (ZENTGRAF et al., 2017) using a laser sheet that is spatially intensity-modulated for luminescence excitation. The in-plane luminescence emission signals are therefore modulated with the same spatial frequency as the excitation laser whereas the interference is not. Several modulated sub-images, ideally three, with different spatial phases can reconstruct the light information originating from emitted luminescence. Multiple pulsed lasers are needed to perform single shot SLIPI, as in Ref. (STEPHAN et al., 2019). Nevertheless, the excitation modulation process was found to come at the cost of a reduced signal-to-noise ratio. Additionally, it is based on a linear luminescence response to excitation density which is often not achieved (FAN und HOCHGREB, 2019). Instead of adopting the averaging window containing tens of particles as the probe unit, we aim to derive temperature information from individual micron-size particles for temperature distribution measurements in the thermal boundary layer.

Different image processing methods have been proposed to access temporal or spectral ratios from individual luminescent particle images. The luminescence signal can be summed in a fixed window (SOMEYA et al., 2011a,b) or recently with an adaptive window (CAI et al., 2022) to take into account particle displacements when using the temporal approach. However, MASSING et al. (2016) showed using virtual particle images that particle center-to-pixel misalignment can cause significant errors in the ratio determination. To minimize such error, they propose to apply a circular Gaussian fit on the particle image to determine the mean or peak intensity value for calculating the ratios. The additional advantages of Gaussian fits are positioning the particle image center with sub-pixel resolution (KÄHLER et al., 2012a).

In this thesis, the Gaussian fit concept is extended and applied to two-color macroscopic imaging of phosphor tracer particles in gas flows. There is a double objective to be achieved, while the first is to obtain high spatial resolution and the second is to avoid re-scattered luminescence signals. Combining high-resolution scientific CMOS camera equipped with a macro objective lens, we aim for diffraction-limited Gaussian-like images of individual particles. Circular Gaussian fit is extended to rotated Gaussian fit to account for astigmatism, and an offset term is added to determine low spatial frequency signals such as re-scattered luminescence. By analytical integration of the Gaussian term, the contribution of re-scattered luminescence is removed from the particle luminescence.

Although this concept is implemented with the two-colour spectral method, it can be directly adapted to the dual-frame lifetime-based approach by using temporally separated images instead. The utilization of both spectrally- and temporally-separated intensity ratios for the determination of temperatures of dispersed individual particles and particles within highly scattering media will be discussed in detail in the subsequent chapter.

3

Imaging strategies for implementing ratio-based thermometry

This thesis employs the phosphor thermometry technique to access temperature information on the basis of the luminescence intensity ratio. Such an intensity ratio determination requires obtaining two spatially matched images of a luminescence field to subsequently calculate the intensity ratio. These two ratio images can be either separated spectrally or temporally. Both separation ways are considered in this thesis to image individual luminescent particles in transparent dispersed fluids, opening the possibility of processing individual particle images to reach a thermometric spatial resolution on the order of the particle size.

On the other hand, another challenging case is studied involving luminescent particles within a porous structure composed of millimeter-sized solid particles, that can be regarded as an opaque and highly scattering media. This case only explores the use of a temporally separated intensity ratio at this stage, given the advantages such as adapting only one camera.

3.1. PRINCIPLE OF THE INTENSITY RATIO DETERMINATION

Also, this chapter presents the selected imaging configurations implementing the intensity ratio determination to image discrete luminescent particles for the two distinct scenarios described above.

3.1 Principle of the intensity ratio determination

The spectral separation method and the dual-frame lifetime method are mainly used to enable the intensity ratio determination, with their difference lying in separating the luminescence spectrally or temporally. The principles of these two methods are briefly presented in this section.

3.1.1 Spectral separation method

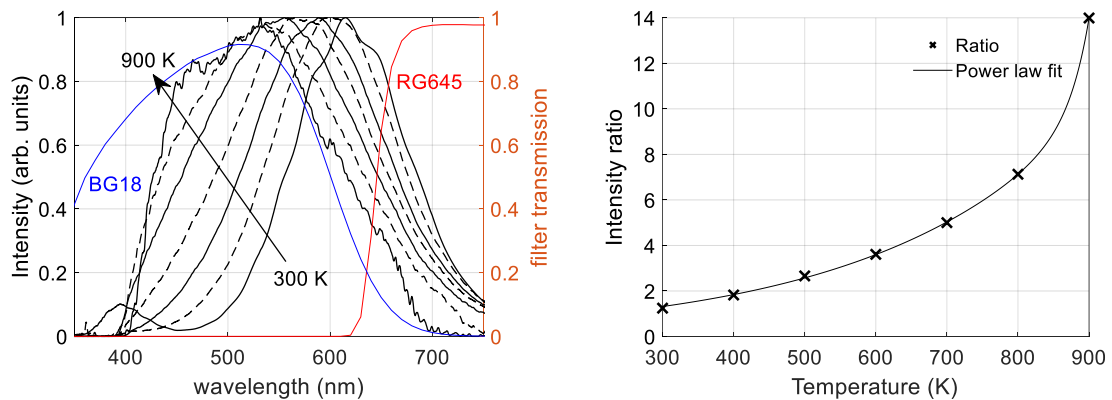


Figure 3.1: Normalised luminescence emission spectra of tin-doped phosphor $(\text{Sr,Mg})_3(\text{PO}_4)_2:\text{Sn}^{2+}$ from 300 to 900 K in furnace superimposed with the filter transmission curves of BG18 and RG645 (both from SCHOTT), and the derived ratios as a function of temperature. The spectra data is obtained from FOND et al. (2019).

The intensity ratio for deriving temperature is commonly obtained with a spectrally separated imaging method, called spectral separation method or two-color imaging. This method typically involves a light source, two spectral filters with different wavelength coverage, two cameras, and a beamsplitter for some configurations. The light

3.1. PRINCIPLE OF THE INTENSITY RATIO DETERMINATION

source provides the excitation light that is directed towards the sample to excite the luminescent particles. Subsequently, the emitted light from the luminescent particles is filtered by the two spectral filters, which are specifically selected to match the peak wavelengths of the emission spectrum. The two filtered emission signals are then collected by the cameras usually with high spatial resolution. After some necessary processes on the recorded images, temperature information can be extracted based on the intensity ratio of the two spectrally filtered emission signals. An illustration of this process for tin-doped phosphor $(\text{Sr,Mg})_3(\text{PO}_4)_2:\text{Sn}^{2+}$ seeded in the gas is presented in Fig. 3.1. It can be observed that the emission spectrum of tin-doped phosphor powders exhibits notable changes when subjected to increasing temperatures within the range of 300 K to 900 K. This spectral transformation spans a wavelength spectrum from approximately 350 nm to over 750 nm. The intensity ratios between the BG18 filter channel and the RG645 channel is calculated as a monotonically increasing function of temperature. Consequently, the ratio establishes a unique and direct correlation with temperature, thus facilitating precise temperature determination within the specified heating temperature range.

3.1.2 Dual-frame lifetime method

Upon excitation by a radiant energy source, some luminescent materials such as phosphors experience an emission that decays exponentially with time. The luminescence intensity decreases over time due to the gradual relaxation of excited electrons from higher energy levels to lower energy levels. The decay process is characterized by the lifetime, representing the average duration for an excited state of a luminescent particle to return to the ground state by emitting a photon. The decay rate is influenced by several factors, such as temperature, oxygen concentration, and impurities present in the luminescent materials. Hence, the luminescence decay, or luminescence lifetime, can be utilized as a sensing mechanism to measure different physical and chemical pa-

3.1. PRINCIPLE OF THE INTENSITY RATIO DETERMINATION

rameters, primarily temperature. To measure the lifetime of the emission, a high-speed camera is commonly used to record a sequence of decayed luminescence intensities of the sample over time. Those intensities are then mathematically fitted using an exponential function to calculate the time for the luminescence intensity decay to $1/e$ of the initial intensity, referring to the emission lifetime. An example of the lifetime of phosphor YAG:Cr³⁺ changing over temperature can be found in Fig. 3.2(a), and this particle was implemented in the demonstration experiment work which will be presented in Chapter. 6.

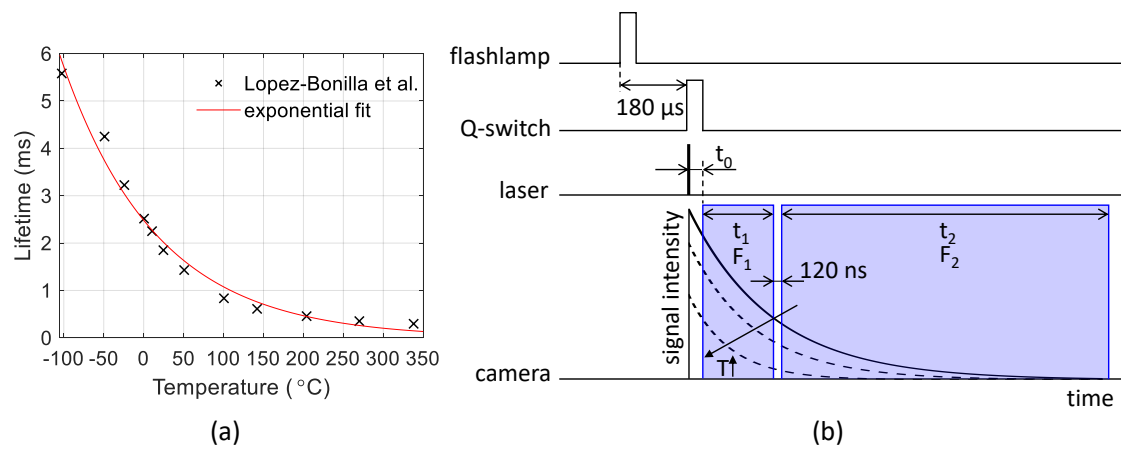


Figure 3.2: (a) Data of YAG:Cr³⁺ lifetime versus temperature from Lopez-Bonilla et al. LOPEZ-BONILLA et al. (2023). (b) The time sequences of the optical devices for implementing the dual-frame 2D lifetime determination. F_1 and F_2 are the frame numbers.

In addition to the spectral separation method in two-color imaging, the intensity ratio can be alternatively obtained by dividing the luminescence signals into two temporally separated images, referred to the dual-frame lifetime method (ABRAM et al., 2018; MASSING et al., 2018; ABRAM et al., 2020). This method typically employs a single camera capable of capturing two consecutive frames with a very short time delay between them. In analog to the spectral separation method, the imaging also includes a light source to excite the phosphor particles and an optical filter but to isolate the phosphorescence emission wavelength. The total intensities collected in the two consecutive frames are computed to relate the ratio to temperature. The

3.2. IMAGING OF INDIVIDUAL PARTICLES DISPERSED IN TRANSPARENT FLUIDS

imaging setup of this method generally requires careful synchronization of the light source and camera to ensure accurate temperature measurement.

Fig. 3.2(b) illustrates the time sequence of the optics to exploit characteristics of phosphor emission decay for temperature measuring. The camera was operated in double frame mode, with the first frame gating delayed with respect to the laser pulse by t_0 , from 0.1 microseconds to several microseconds depending on the phosphor lifetime in our experiments, so as to minimize residual laser reflections and the fast laser induced fast fluorescence from the cuvette material or the binder (MENDIETA et al., 2019). The temperature-dependent decaying luminescence was split into two consecutive camera frames with a short inter-frame time (~ 120 ns for our camera). Therefore, for a given camera-laser timing, the recorded luminescence intensity ratio $\varphi(T)$ between the two frames is a function of temperature, enabling the temperature measurement of interest. To achieve optimal temperature precision, the ratio of the exposure time of the first frame (t_1) to the lifetime (τ) of seeded phosphor should fall within the range of 0.5-4, which was demonstrated in the study conducted by ABRAM et al. (2020).

3.2 Imaging of individual particles dispersed in transparent fluids

Individual luminescent particles can act as independent thermometers in transparent fluids to reach a high spatial resolution temperature measurement. For this, it is essential to establish two images of a single particle field and perform the intensity ratio determination on individual dispersed particles. Various two-color imaging configurations that have advantages in acquiring two spatially matched images have been discussed in ABRAM et al. (2018). The main point here is the visualization and acquisition of well-separated, micron-sized, individual particle images. Within the

3.2. IMAGING OF INDIVIDUAL PARTICLES DISPERSED IN TRANSPARENT FLUIDS

scope of this thesis, we explore both the spectral separation method and the dual-frame lifetime method for imaging isolated particles dispersed in water and air environments. This section clarifies the selection and adjustments of the optical configurations for facilitating the implementation of these two methods.

3.2.1 Two-color imaging applying the spectral separation method

3.2.1.1 Configuration with beamsplitter

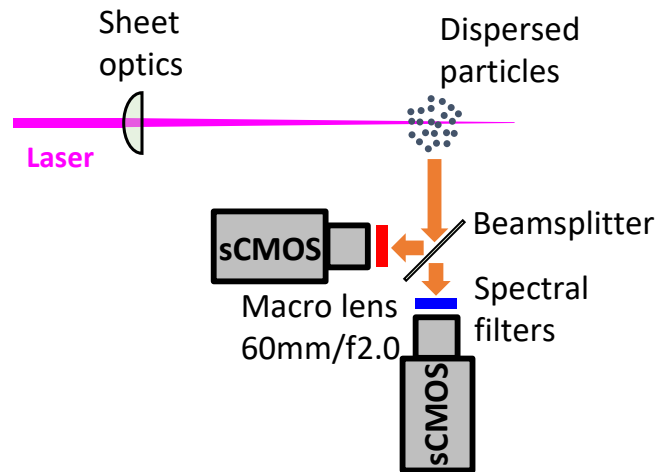


Figure 3.3: Two-color configuration of beamsplitter arrangement to enable spectrally separated Imaging of individual dispersed particles.

The first configuration enabling the spectral separation method is a high spatial resolution version of the thermometry part of a typical thermographic PIV setup, which was employed in previous studies to exploit the usual two-color intensity ratio (ABRAM et al., 2018). The arrangement of this configuration can be seen in Fig. 3.3. A laser beam, normally operating in the UV range, is pulsed to go through a convex lens forming a light sheet, with a dual purpose of exciting the dispersed particles and defining the measurement plane in the dispersion. The luminescence excitation would first reach a beamsplitter, which serves a uniform division of the luminescent signals without any spectral selection. The divided signals are then directed toward two cameras

3.2. IMAGING OF INDIVIDUAL PARTICLES DISPERSED IN TRANSPARENT FLUIDS

that are mounted with different spectral filters and placed at orthogonal angles of 90 degrees to each other. Both of these two cameras run in single-frame mode, leading to a simultaneous capture of two distinct views of the same individual particle in different spectral regions. For detection, scientific-CMOS (sCMOS) cameras were chosen. These cameras possess a full resolution of 2560×2160 pixels, a pixel size of $6.5 \mu\text{m}$, and a full well capacity of $30000e^-$. The consistent utilization of sCMOS cameras is across all imaging configurations within this thesis as they present a lower noise level compared to other common optical imaging cameras such as CMOS and CCD cameras. To obtain distinct individual particle images, Tamron 60mm f/2.0 Macro objective lenses were determined for their advantage in having a high magnification ratio approaching 1:1, which indicates an individual particle can be reproduced on the camera sensor at almost life-size, resulting in highly detailed particle images.

Aiming at minimizing the individual particle image aberrations induced by the beamsplitter, the performance of multiple types of beamsplitters on imaging liquid dispersed particles was explored. The objective was to obtain Gaussian-like particle image intensity distribution to implement the two-dimensional Gaussian fit (discussed later in Chapter. 4). In the first column of Fig. 3.4, images obtained with a 1 mm thin flat plate 50/50 beamsplitter (Edmund Optics 46-642) are displayed. Due to the compromised surface flatness of this arrangement, a significant amount of aberration is introduced in the reflected image. When a high-quality dichroic beamsplitter (Chroma T445lp, surface flatness better than 1λ) with a thickness of 2 mm was used, the resulting reflection image was found to be Gaussian-like, whereas the transmission images would exhibit a rhombus shape as shown at the top of the second column of Fig. 3.4, presumably due to the larger thickness of the beamsplitter causing parallel plates beamsplitter astigmatism and coma. Therefore, to minimize the thickness, a $2 \mu\text{m}$ thin 50/50 pellicle beamsplitter (Thorlabs BP245B1) was applied instead, which was found to almost eliminate aberration in both channels, as shown in the third column

3.2. IMAGING OF INDIVIDUAL PARTICLES DISPERSED IN TRANSPARENT FLUIDS

of Fig. 3.4. This pellicle beamsplitter was consequently determined to be used in the beamsplitter configuration.

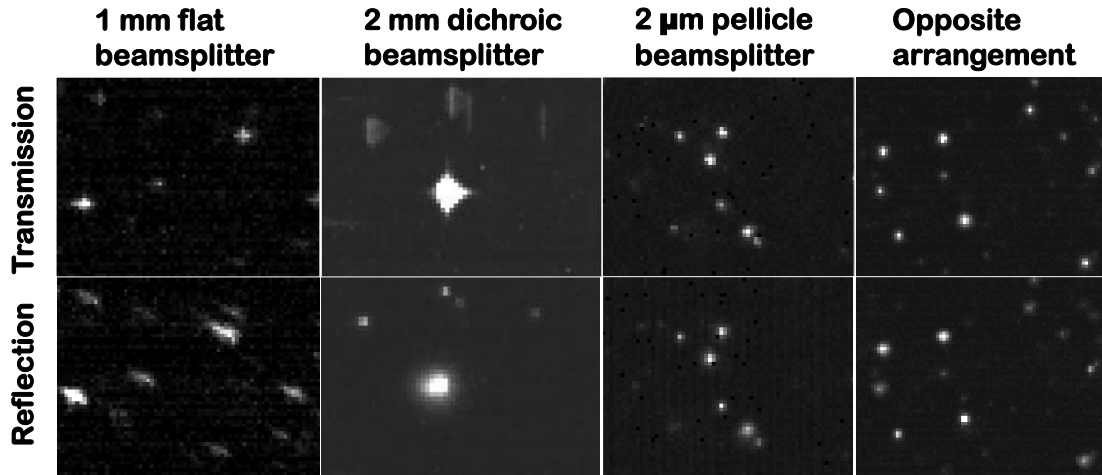


Figure 3.4: Example particle images obtained with different optical setup arrangements: thin beamsplitter, high flatness beamsplitter, pellicle beamsplitter and no beamsplitter (cameras on opposite sides). This figure is reproduced from XUAN et al. (2023).

3.2.1.2 Configuration with opposite camera setting

The second configuration selected for implementing the spectral separation method is shown in Fig. 3.5. This configuration is almost identical to the beamsplitter configuration shown previously in Section. 3.2.1.1, while the only discrepancy is that it is adjusted by positioning the cameras on opposite sides of the measurement plane so that the beamsplitter can be abandoned. It is important to note that the filters used here can block light with wavelengths outside the transmission range by absorption. Therefore, the reflected luminescent signals from the opposite filters can be neglected. This configuration has the advantage of maximizing the signal-to-noise ratio and avoiding the abovementioned beamsplitter aberrations, as shown in the final column of Fig. 3.4. However, because of the distinct acquisition directions of the two cameras, this configuration may be more sensitive to potential luminescence anisotropy.

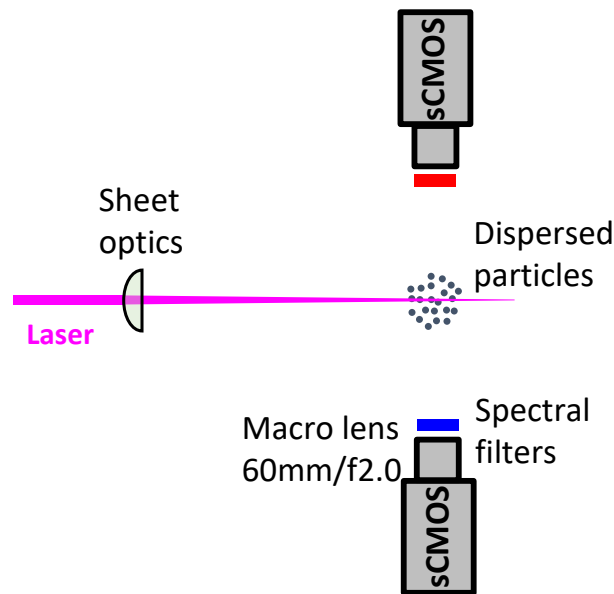


Figure 3.5: Two-color configuration with opposite camera setting to enable spectrally separated Imaging of individual dispersed particles.

3.2.2 Temporally-separated dual-frame imaging

Fig. 3.6 illustrates the configuration designed for the implementation of the dual-frame lifetime method to acquire individual dispersed particle images. Rather than using two cameras to obtain spectrally distinct particle images, this configuration opts for only one camera (the same camera type) operated in a double-frame mode to exploit the temporal characteristics of particle luminescence, yielding two time-consecutive images of the same individual particles within a single particle emission event. On the other hand, unlike the spectral filters utilized in the spectral separation method, which match the peak wavelengths of the particle emission spectrum for spectral selection, the filter set in this configuration primarily serves to mitigate potential interference signals originating from stray light or unintended reflections of the excitation laser. This way enhances the reliability of the acquired images by minimizing undesirable sources of noise or artifacts.

3.3. IMAGING OF LUMINESCENT PARTICLES IN A POROUS STRUCTURE COMPOSED OF MILLIMETER-SIZED SOLID PARTICLES

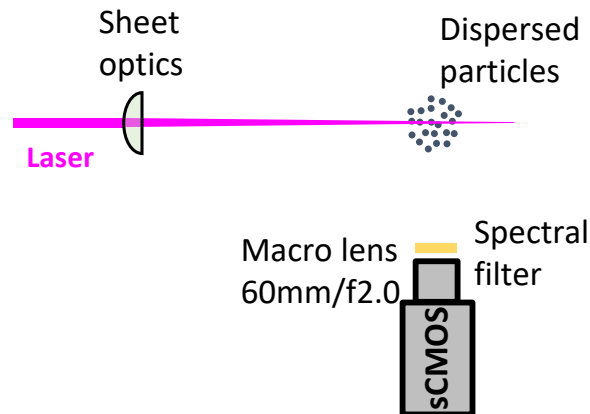


Figure 3.6: Single camera configuration to enable temporally separated Imaging of individual dispersed particles.

3.3 Imaging of luminescent particles in a porous structure composed of millimeter-sized solid particles

To explore the temperature measurement utilizing the luminescent particles in highly scattering media, a media with an opaque porous structure composed of millimeter-sized solid particles is chosen. When the luminescent particles are situated inside such a media, their direct excitation or direct imaging of luminescence becomes impossible. In order to implement the intensity ratio determination, this section presents an optical configuration to obtain the two ratio images in an indirect way using the dual-frame lifetime method, as shown in Fig. 3.7.

Imaging of dispersed individual particles applies both the spectral separation method and the dual frame lifetime method for intensity ratio determination. In the above discussions, the former method involves two imaging configurations in which two cameras are positioned, at 90 degrees to each other, and on opposite sides, respectively. However, within the context of opaque scattering media, the spectrum detected by the camera may deviate from that originating from the luminescence

3.3. IMAGING OF LUMINESCENT PARTICLES IN A POROUS STRUCTURE COMPOSED OF MILLIMETER-SIZED SOLID PARTICLES

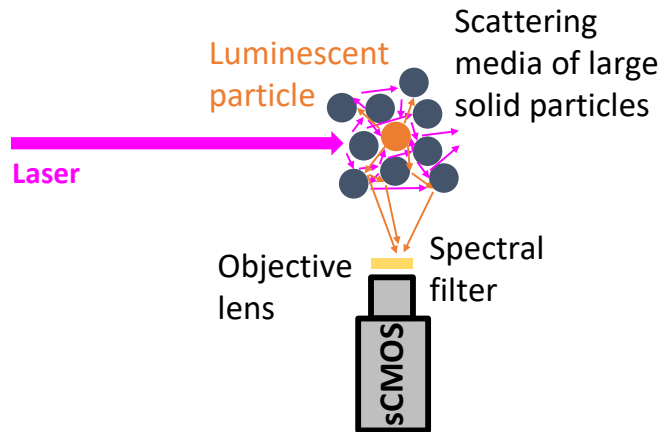


Figure 3.7: Schematic of the configuration implementing dual-frame lifetime method to indirectly image luminescence originating inside an opaque scattering media of large solid particles.

source due to the reflection-induced distortion. In particular, the opposite camera configuration can manifest pronounced anisotropy owing to the significant disparities in the light path when the luminescence leaves the opaque porous structure through multiple scattering/reflection events. On the other hand, this issue also changes the traversing time of each ray to reach the camera, consequently distorting the luminescence lifetime detected by the camera. While it should be noted this distortion generally occurs at the nanosecond scale attributed to the limited size of the porous structure, such a temporal distortion can be neglected, especially when considering a luminescent particle with emission decay times on the order of microseconds or longer. The imaging configuration for this case is therefore designed based on the dual-frame lifetime method.

Compared to the imaging configuration illustrated in Fig. 3.6, the camera also runs in a double-frame mode and the spectral filters here serve the same purpose, while the sheet optic of the convex lens is removed so that the laser beam would directly illuminate the porous structure. Some of the laser light reaches the luminescent particles after multiple scattering/reflections to excite them. A portion of the resulting

3.3. IMAGING OF LUMINESCENT PARTICLES IN A POROUS STRUCTURE COMPOSED OF MILLIMETER-SIZED SOLID PARTICLES

luminescence exits the packed bed, also after multiple scattering/reflections, and is ultimately collected by the camera. In addition, given that the luminescent particles here are on millimeter order or possibly even bigger, a standard objective lens may suffice. Nevertheless, an objective with a lower minimum f-number is preferable, as it provides a larger aperture for the efficient collection of luminescence, especially considering that the scattering medium attenuates a significant portion of the luminescent signal.

4

Image processing and data evaluation

In order to interpret temperature information provided by the particle luminescence images, the acquired raw images are subjected to a sequence of treatments. For micron-sized luminescent particles dispersed in fluids, the goal is to enable each particle to act as an independent detector by means of locating all particles in the interrogation two-dimensional plane and subsequently performing Gaussian fits to each of their images. On the other hand, for large luminescent particles distributed in highly scattering media of millimeter solid particles, here chosen as a packed bed, this thesis aims to separate compound signals of multiple luminescent sources into individual contributions, so that each of the luminescent particles can also act as an independent probe to measure instantaneous multi-point temperature in the packed bed. The work in this chapter is partly derived from the publications XUAN et al. (2023) and XUAN et al. (2024).

4.1 Temperature and position determination of individual dispersed particles

This section presents an overview of the theoretical foundation and the processing steps for high spatial resolution thermometry in fluids through individual particle image analysis. The process starts with locating particles over one of the two ratio frames. Subsequently, fitting windows are defined around these locations. A two-dimensional Gaussian fit is then applied to those fitting windows for quantifying particle signals, and obtaining sub-pixel positioning of the particle center. Note that the dual-frame lifetime method, which utilizes only one camera, can acquire two spatially identical images, meaning there is no displacement of the same particle field between these two images. Conversely, displacement and distortion correction are required when implementing the spectral separation method which typically employs two cameras, even with careful alignment adjustment. To resolve this issue, for each particle found in the first ratio frame, a fitting window in the other ratio frame is determined by performing a pixel shift with respect to the first frame. The shift in the two spatial directions is specified from PIV-like cross correlation process on the two ratio frames. Finally, the intensity ratio from each individual particle is derived through analytical integration of the fit expressions, and converted to temperature. At the end of this section, synthetic particle images are used to evaluate the positioning accuracy of the processing.

4.1.1 Theory of the concept

When light emanating from a distant point source is imaged on an observation plane through a round aperture, such as a camera lens, it generates a far-field diffraction pattern instead of a bright dot, regardless of the size of the light source. Consequently, the recorded luminescence image of a single particle, even nanometer-sized, exhibits

4.1. TEMPERATURE AND POSITION DETERMINATION OF INDIVIDUAL DISPERSED PARTICLES

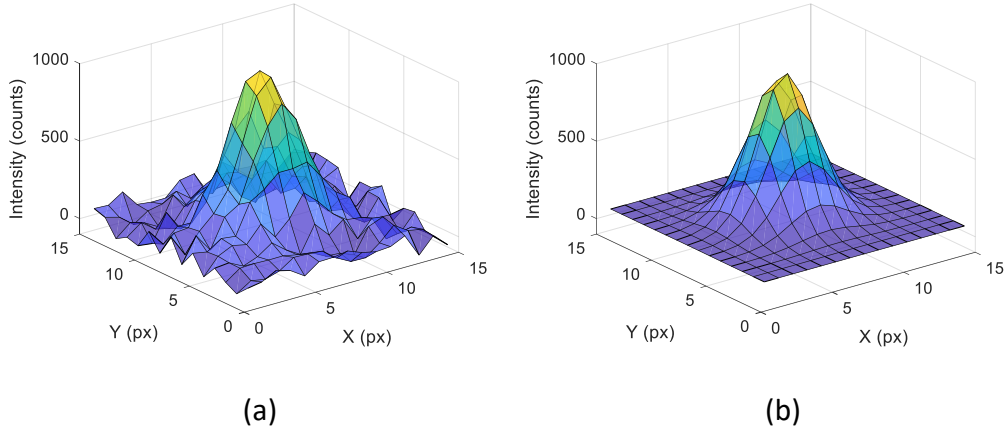


Figure 4.1: Illustration of the particle point spread function fitting: (a) raw particle image and (b) the corresponding 2D Gaussian fit image. This figure is reproduced from XUAN et al. (2023).

a spatial distribution that resembles a Gaussian-like form, as shown in Fig. 4.1(a). This intensity distribution, also known as an Airy disk distribution, is thus typically approximated using the two-dimensional Gaussian function (RAFFEL et al., 2018) or point spread function (PSF), with the particle luminescence signal at location x_0, y_0 written as:

$$I_p(x, y) = I_0 \cdot \exp \left[-\frac{(x - x_0)^2}{2\sigma_x^2} - \frac{(y - y_0)^2}{2\sigma_y^2} \right] \quad (4.1)$$

where I_p is the spatial intensity distribution of a single particle image, I_0 the peak value of the intensity distribution, σ_x and σ_y the particle size constants determining the particle image size in two in-plane dimensions. Fig. 4.1(b) illustrates the fitting of Fig. 4.1(a) using the Eq. (4.1). The difference between the fitted and recorded image is attributed to sensor noise, and the non-gaussian character of the particle image which contains contribution from image aberrations that are induced by the imperfect imaging system. When luminescence signals of a single particle are separated into two channels, either by two different spectral filters or two time-consecutive frames, temperature information can be extracted from the ratio of the total number of photons reaching each channel, as this ratio will be a function of temperature due to the temperature dependence of the emission spectrum or lifetime, respectively. The

4.1. TEMPERATURE AND POSITION DETERMINATION OF INDIVIDUAL DISPERSED PARTICLES

number of photons contributing to one of the channel images of the particles is given by the double spatial integral of the particle PSF:

$$S_p = \int \int I_0 \cdot \exp \left[-\frac{(x-x_0)^2}{2\sigma_x^2} - \frac{(y-y_0)^2}{2\sigma_y^2} \right] dx dy = 2\pi I_0 \sigma_x \sigma_y. \quad (4.2)$$

A temperature-dependent ratio can then be derived for each particle from:

$$\varphi(T) = \frac{(S_p)_{\text{image1}}}{(S_p)_{\text{image2}}} = \frac{(I_0 \sigma_x \sigma_y)_{\text{image1}}}{(I_0 \sigma_x \sigma_y)_{\text{image2}}} \quad (4.3)$$

Fig. 4.2(a) illustrates an example of a subset of a luminescence image containing two phosphor particles in one of the two intensity-separated channels, and Fig. 4.2(b) is the fitted image as a superposition of the fit of these two particles. After performing the fit on both channel images, the ratios of signals from these two particles are derived, and are associated with the center location of the particles, as shown in Fig. 4.2(c). In this way, every seeded phosphor particles acts as an independent thermometer with the spatial resolution approaching the particle-size.

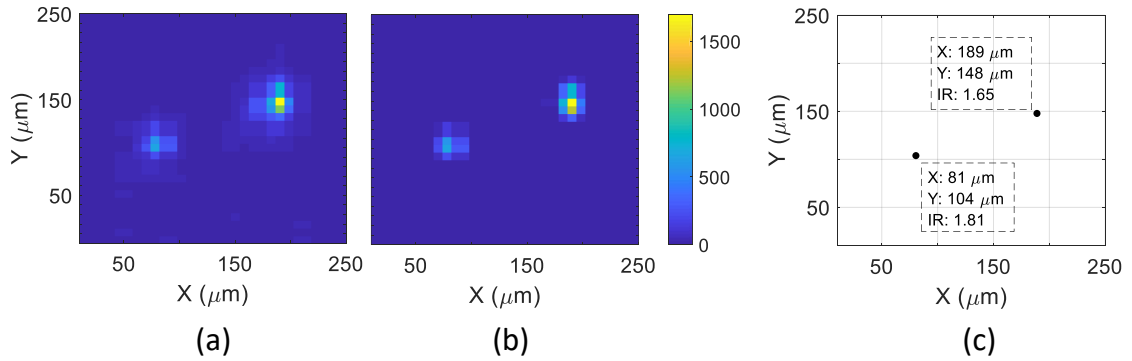


Figure 4.2: Illustration of particle image processing. (a) Raw image in one recording channel; (b) corresponding fitting and (c) derived intensity ratios. This figure is reproduced from XUAN et al. (2023).

4.1.2 Particles detection and localization

To enable the Gaussian fit to individual particle images, it is necessary to identify a subregion of the image centered on each particle locations. Therefore, all the particle locations on at least one ratio image must be determined first. An in-house developed algorithm was used, consisting of a combination of local maximum determination and gradient threshold filtering which is illustrated in Fig. 4.3. The aim of this algorithm is to detect a particle from the values of local differences rather than threshold on the absolute intensity value to be robust in the presence of high background signals. As a first step, pixels with an intensity higher than their eight neighboring pixels are considered local maxima, as presented in Fig. 4.3(b). One can see that there are many more of such local maxima than actual particles, due to spatial features in the dark image or background signals, as well as contributions from the so called "hot" pixels. Since those "fake-particles" are normally isolated pixels without any intensity distribution, we applied an additional gradient filter to distinguish the actual particles. This gradient filter calculates for each pixel $D_{i,j}$ the mean of the local intensity differences between $I_{i,j}$ to its 4 adjacent pixels, $I_{i-1,j}$, $I_{i+1,j}$, $I_{i,j-1}$, $I_{i,j+1}$. Next it evaluates $G_{i,j}$ the mean of the four corners of its centered 9x9 subareas $D_{i-1,j-1}$, $D_{i+1,j-1}$, $D_{i-1,j+1}$, $D_{i+1,j+1}$. A thresholding operation of $G > G_{tr}$ is then applied to the G image, resulting in the binary image shown in Fig. 4.3(c). Finally taking the intersection of the two sets of ensemble

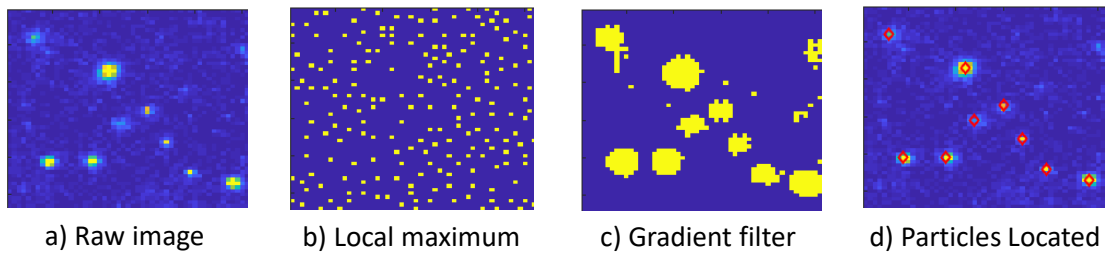


Figure 4.3: Image processing steps to locate particles: a) raw image b) local maximums c) gradient filter d) detected particle positions. This figure is reproduced from XUAN et al. (2023).

4.1. TEMPERATURE AND POSITION DETERMINATION OF INDIVIDUAL DISPERSED PARTICLES

pixels, yields the particle center locations as shown in Fig. 4.3(d). This method, that relies only on intensity gradients rather than direct intensity thresholding, has the benefit of being insusceptible to noise introduced by fluctuations in the background signal.

This algorithm would exclude particles with very low signal intensity, which appear as single pixel-wide images despite a minimum image size constant dictated by diffraction. Additionally, particles with very large particle image size constant would also be discarded. Since the optical system employed limits blur (thin laser sheet) and aberration, such images would originate either from large agglomerates or from re-scattered luminescence. If two particles are present along the same line of sight within the laser sheet thickness, they would incorrectly be detected as a single particle given their image center is less than 2 pixels apart. However, given the light sheet thickness ($150\ \mu\text{m}$) and the average particle distance ($450\ \mu\text{m}$) used here, such a case is highly unlikely. In addition, unless the particle perfectly overlaps, it will lead to a non-Gaussian particle image, which could be detected by a threshold filter based on a fit quality criterion.

4.1.3 Particle image fitting

For each individual particle image it is essential to define a fitting window, i.e. an ensemble of pixels centered on the particle center, so as to utilize the data in those pixels as the input in the fit. A square window was chosen, whose width should be large enough to cover the entire particle signals but also conversely small enough to prevent integrating two or more particles. To guide the selection, we considered a Gaussian function with a theoretical sigma of 1 pixel approximated by the lens modulation transfer function (MTF) provided by the manufacturer following the description in RAFFEL et al. (2018). Note that the implemented optical setup in this study has a diffraction limited diameter of only 0.7 pixels. Therefore, if the particle intensity

4.1. TEMPERATURE AND POSITION DETERMINATION OF INDIVIDUAL DISPERSED PARTICLES

follows a Gaussian distribution, a 6×6 pixel region should in principle encompass 97 % of the overall intensity of single particle. To accommodate the disparity between the window center and the particle's center, we settled on a 9×9 pixel window.

Subsequently, it is important to emphasize that the recorded signal can contain contribution which do not originate from the image particle themselves, e.g. stray light, gas emissions, or re-scattering of luminescence. Those contributions originating outside of the focus plane of our imaging system, we can simply assume that over the length scale of a single fitting window, its spatial variation is negligible. A constant term is thus added into Eq. (4.1), to consider such contributed signals:

$$I_r(x, y) = I_0 \cdot \exp \left[-\frac{(x - x_0)^2}{2\sigma_x^2} - \frac{(y - y_0)^2}{2\sigma_y^2} \right] + I_c \quad (4.4)$$

where the I_r is the recorded intensity and I_c the pixel independent low spatial frequency signal specific to each particle, meaning that the term I_c varies from fitting region to fitting regions.

An example of a raw particle subimage before fitting in one out of the spectrally separated channels can be found in Fig. 4.4 (left), and its peak to background signal-to-noise ratio (SNR) is estimated to be about 50. The fitting intensity distribution of this particle image using Eq. (4.4) based on least square method is in Fig. 4.4 (right). The detailed fitting results are shown in Table. 4.1. During the fitting, the first guess of particle position is obtained from the particle detection (including shift mentioned later in Section. 4.1.4 for identifying the corresponding particle in the other spectrally filtered channel). The initial value for the peak of intensity distribution is taken as the maximum signal within the fitting window. Parameters σ_x and σ_y are set to 1 pixel as discussed above. The initial guess of interference term I_c is set to be zero as the background signal is subtracted.

4.1. TEMPERATURE AND POSITION DETERMINATION OF INDIVIDUAL DISPERSED PARTICLES

If the measured data in i_{th} pixel of the fitted area is represented as I_i and the predicted value from Eq. (4.4) as f_i , a criterion, R-squared or R^2 , to quantify the performance of the prediction on measurement is expressed as:

$$R^2 = 1 - \frac{SS_{res}}{SS_{tot}} \quad (4.5)$$

with SS_{res} being the residual sum of squares (RSS):

$$SS_{res} = \sum_i (I_i - f_i)^2 \quad (4.6)$$

and SS_{tot} is the total sum of squares:

$$SS_{tot} = \sum_i (I_i - \bar{I}_i)^2 \quad (4.7)$$

The closer this R^2 is to 1, the better Eq. (4.4) describes the measured intensity distribution. With a R^2 of 0.98, the fitting illustrated in Fig. 4.4 closely match the measured particle image.

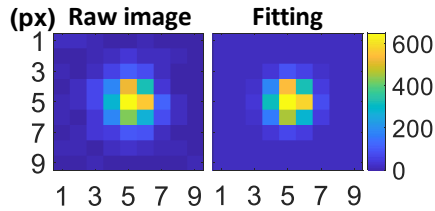


Table 4.1: Results of the fitted single particle image example

| I_0 (cts.) | x_0 (px) | y_0 (px) | σ_x (px) | σ_y (px) | I_c (cts) | R^2 - |
|-------------------|---------------|---------------|--------------------|--------------------|----------------|------------|
| $1.12 \cdot 10^3$ | 5.19 | 4.94 | 0.71 | 0.80 | 27.16 | 0.98 |

Figure 4.4: Particle fit example, reproduced from XUAN et al. (2023).

In reality, however, aberrations in the optical system will prevent the acquisition of perfectly circular Gaussian particle images. Unlike in the thin lens approximation, if parallel light rays pass through the system, they will not meet at the same point but spread out across an area instead of forming an infinitely thin dot in the ideal case. This phenomenon results in the recorded particle image being blurred or distorted

4.1. TEMPERATURE AND POSITION DETERMINATION OF INDIVIDUAL DISPERSED PARTICLES

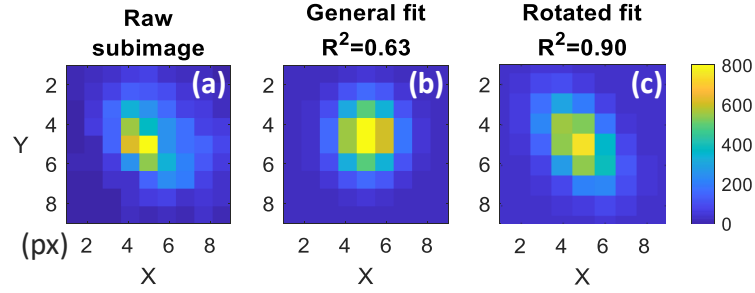


Figure 4.5: Fitting for astigmatic particle images. a) raw particle image; b) result of general Gaussian fit; c) result of rotated Gaussian fit. This figure is reproduced from XUAN et al. (2023).

by astigmatism, especially when the interrogation region is closer to the edge of the view field, where the symmetry axis of the particle image is rotated with respect to the camera axis. Fig. 4.5(a) shows the image of a particle at the edge of view field, whose peak to background SNR is estimated to be about 40. One can easily see that this image, along with a discernible tilt, vaguely spreads out. To address this problem and increase the fitting quality, Eq. (4.4) is transformed into the two-dimensional rotate Gaussian function by introducing an extra coefficient, the shifting angle θ :

$$I_r(x, y) = I_0 \cdot \exp \left[-a(x - x_0)^2 - 2b(x - x_0)(y - y_0) - c(y - y_0)^2 \right] + I_c \quad (4.8)$$

with

$$a = \frac{\cos^2 \theta}{2\sigma_x^2} + \frac{\sin^2 \theta}{2\sigma_y^2} \quad (4.9)$$

$$b = -\frac{\sin 2\theta}{4\sigma_x^2} + \frac{\sin 2\theta}{4\sigma_y^2} \quad (4.10)$$

$$c = \frac{\sin^2 \theta}{2\sigma_x^2} + \frac{\cos^2 \theta}{2\sigma_y^2} \quad (4.11)$$

Again, both Eq. (4.4) and Eq. (4.8) are applied to the distorted particle image in Fig. 4.5(a) based on the nonlinear least squares fit, the outcomes are in Fig. 4.5(b) and (c) separately. Compared to the general Gaussian fit, the rotated Gaussian form matches

4.1. TEMPERATURE AND POSITION DETERMINATION OF INDIVIDUAL DISPERSED PARTICLES

better the observed distribution for particle images with significant aberration, with an improvement in R^2 from 0.63 to 0.9.

In Section. 5.1.5, the performance of the two types of fitting functions is compared, and the rotated Gaussian is shown to provide a lower measurement uncertainty. The rotated Gaussian function was therefore used otherwise stated. Note that when the shifting angle θ is approaching to zero, the rotated Gaussian form Eq. (4.8) that describes the image aberration coincides with the non-rotated Eq. (4.4).

Although R-square (Eq. (4.5)) can well quantify the performance of fitting, a good fit does not always indicate an accurate temperature because the SNR of the raw recorded data itself may be too low, considering the uncertainties in measured temperature will significantly increase with SNR decreasing when SNR is below 20 (MASSING et al., 2016). To avoid contribution from overly weak particles in the temperature statistics, before fitting, a cutoff of the peak intensity (> 300 counts) and, after fitting, a cutoff of the integral intensity (> 1000 counts) are applied on all of the detected particles to make sure they have sufficient SNR.

In addition, prior to performing nonlinear least squares fit, the distance of each particle to the center of its nearest particle, detected in the particle localization process, is computed. Consequently, for simplification and minimizing the fitting uncertainty caused by the particle image superposition, we only select the particles which are located beyond a minimum distance of 4.5 pixels ($45 \mu\text{m}$ for this setup) from any other particles. Though there is a possibility to solve such overlapping situation through considering a sum of 2D Gaussian functions instead of the single term of Eq. (4.1), it would require to determine prior to fitting how many Gaussian terms have to be added in accordance to the number of particles contributing to the signals in single 9×9 interrogation window. Furthermore, the current method is limited in its ability to identify particles that overlap completely in the thickness direction, which may introduce bias in temperature measurement. However, the probability of this occurrence is extremely low, so the resulting errors in a 2D temperature field measurement can be

4.1. TEMPERATURE AND POSITION DETERMINATION OF INDIVIDUAL DISPERSED PARTICLES

considered negligible. To address this issue, a potential way is to incorporate a third camera to reconstruct the stereo positions of the detected particles.

4.1.4 Misalignment correction between spectrally separated images

Until this point, the described processing steps were only applied to one of the two ratio frames. To determine the signals of the particle in the other ratio frames, which is necessary for ratio calculation, the particle image in the other frame should be identified, i.e., the center of the fitting window must be defined for each particles in the other ratio frame. This is a straightforward task for an second frame acquired by the dual-frame lifetime method, since both frames are recorded by the same camera, indicating that the particles are located in very the same positions in both channels.

However, if the temperature measurement employs a method requiring two distinct sensors, such as the two-color spectrally separated approach, displacement correction must be considered, as mentioned above. To address this case, in this study, the intensity distributions of the two frames were subjected to a cross-correlation algorithm in order to create a vector field that represents the relative distortion between the two frames and can thus be used to pair the particles. Over a series of recorded frame pairs, an average vector field was calculated. An example of such vector field was presented in Fig. 18 of ABRAM et al. (2018). This process is analogous to self-calibration in stereoscopic particle image velocimetry (WIENEKE, 2005). The disparity vectors in resultant vector field would have two components, one for each axis of image displacement, typically within 20 pixels in our measurement. If we assign them as Δy and Δx , and we know that the location of the target particle in one ratio image a is at $(x_{0,a}, y_{0,a})$ from the localization in Section. 4.1.2, then the position of this particle $(x_{0,b}, y_{0,b})$ in the other ratio image b is thereupon estimated by the formulas:

$$x_{0,b} = x_{0,a} + \Delta x \quad (4.12)$$

4.1. TEMPERATURE AND POSITION DETERMINATION OF INDIVIDUAL DISPERSED PARTICLES

$$y_{0,b} = y_{0,a} + \Delta y \quad (4.13)$$

The fitting window for the second frame is then centered around the shifted particle positions. According to the research presented in WIENEKE (2005), the inaccuracy introduced by this self-calibration procedure is less than 1 pixel, which is satisfactory for our method. It is sufficient for the corrected displacement to be less than half of the minimum inter-particle distance to unambiguously establish particle correspondence between the images in two sensors. Since these two images are fitted independently to determine both total luminescence signals, once correspondence is established, the residual displacement should in theory not impact on the intensity ratio calculation.

4.1.5 Intensity ratio calculation, corrections and conversion to temperature

To determine temperatures, it is required to compute the total intensity ratio of each individual particle between the two images that have been spectrally or temporally separated. As a result of the fact that Eq. (4.8) splits the recorded intensity from a single particle into two distinct signals, referring to particle-self emission and interference, we can then obtain total particle intensity from integrating particle-self emission only (the first term on the right-hand side of Eq. (4.8)). This can seem like a complicated computation; but note that the difference in physical meaning represented by Eq. (4.8) and Eq. (4.4) is only in the orientation indicating that they should share the same integration particle intensity which was described in Eq. (4.2). The temperature-dependent ratio of the integrated particle intensity in each 9x9 pixels window can thus also be inferred using Eq. (4.3).

Furthermore, a "white field" correction (sometimes called flat field) is necessary to remove spatial variations originating from fluctuations in spectral transmittance across the field of view due to the angular dependence of the beamsplitter and or filters, as well as potential effect of non uniform laser fluence. Here, we accomplished this

4.1. TEMPERATURE AND POSITION DETERMINATION OF INDIVIDUAL DISPERSED PARTICLES

by obtaining a discrete ratio distribution using the proposed fitting-based technique under isothermal conditions, such as at room temperature, followed by interpolation to generate a smooth and continuous intensity ratios field as a reference. The evaluated ratios under non-isothermal conditions are then divided from the ratios at the corresponding location in the reference field. Consequently, the intensity ratios are only correlated to temperature, but independent of the fluence distribution or the non-uniformity of the light transmission.

4.1.6 Particle positioning accuracy

In this section, we evaluate, using virtual particle images, the ability of the algorithm to accurately position the center of each particle, and therefore of each temperature measurement.

The evaluation can rely on frameworks developed for Particle Tracking Velocimetry (PTV), which is a technique to measure fluid velocity that depends on tracking individual particles between time-separated images. The velocity accuracy is directly related to the positioning accuracy of the particle images, and virtual particle images are often used to determine velocity uncertainty. In KÄHLER et al. (2012a), the Root Mean Square Error (RMSE) of the particle center localization was shown to be a measure of the spatial resolution. Here, we also used synthetic luminescence image with a realistic noise contribution to provide a statistical quantification of the localization bias.

The rotated Gaussian Eq. (4.8) was used here to simulate particles randomly distributed in a 3D volume, and sliced by the laser sheet. To emulate similar signal levels as the measured data, in Fig. 4.5, the peak intensity of particle signals distribution was set to be 800 counts and a baseline of 10 counts was added across the full frame to simulate the multiple scattering between luminescent particles. Additionally, the particle size constants, σ , was chosen to be 1 pixel as described in Section. 4.1.3, so

4.1. TEMPERATURE AND POSITION DETERMINATION OF INDIVIDUAL DISPERSED PARTICLES

the apparent diameter of digital particle images was approximately 6 pixels. In order to account for astigmatism, the rotation angle gradually increased from 0 degree at the synthetic image center to 45 degree near the image edge, see particles in Fig. 4.6 that are away from the optical axis. The rotation angle changing follows a 2D Gaussian distribution, and we added a 10 % variation in this changing. Noise signal was imposed by adding a normally distributed random number multiplied by the square root of local intensity to consider the shot noise contribution and a fixed value of 8 counts to consider the readout noise.

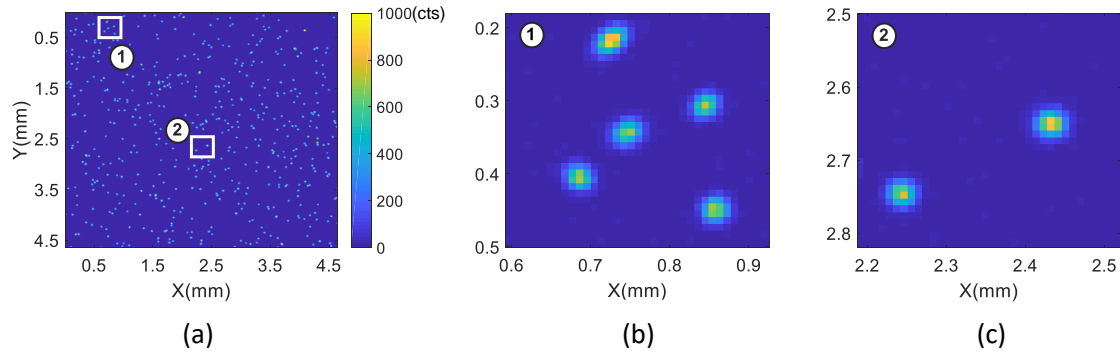


Figure 4.6: (a) Synthetic particles images based on 2D rotate Gaussian; (b) Significantly rotated particles simulating the strong astigmatism in the near edge region; (c) Highly Gaussian-like images with negligible astigmatism in the center region.

Approximately 350 particles were consequently analysed in a 4.5×4.5 mm sub-area after filtering out overlapping particles. Fig. 4.7 shows the deviations between the fitted and the synthetic image for the particles center in x and y direction (x_0 and y_0) as well as the center to center distance. It can be seen that the root mean square error is less than 0.2 pixel. This agrees with the previous study on the PTV technique, which obtains a RMS-uncertainty below 0.1 pixels for the simulation particle diameter from 3 - 20 pixels using a non-rotated general 2D Gaussian function (KÄHLER et al., 2012b). Thus, our technique should enable a 2D thermometry with a measurement positioning accuracy resolution in the order $2 \mu m$.

4.2. TEMPERATURE DETERMINATION OF LUMINESCENT PARTICLES IN AN OPAQUE PACKED BED

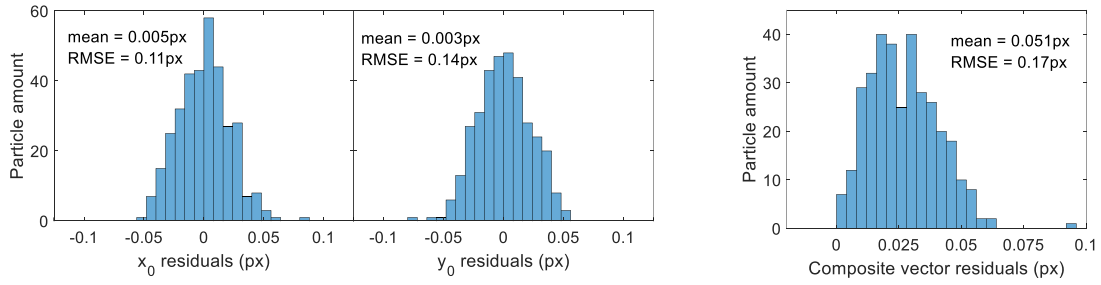


Figure 4.7: Fitted center residuals in x and y direction and of the composite vector obtained for virtual particle images

4.2 Temperature determination of luminescent particles in an opaque packed bed

This section covers the process of temperature measurement at the points corresponding to the phosphor-coated spheres inside a packed bed through the analysis of signals within the acquired luminescence images. Initially, the case of a single luminescent sphere in a designed regular packed bed is considered, where all the collected signals are from the same sphere, so that the total emission intensity from the sphere can be calculated easily, and the intensity ratio between the two temporally separated frames can be directly computed to derive the temperature. The work is then extended to the case of multiple luminescent spheres, where a linear regression is performed to accurately isolate the signal contribution of each sphere, enabling the temperatures at each sphere location to be inferred from their respective intensity ratios.

4.2.1 Case of a single luminescent sphere

Fig. 4.8 illustrates an example of the recorded image in the first ratio frame when there is only one luminescent sphere at the core of the designed packed bed. Within the region in the figure indicated by the white-dashed rectangle, the brightest regions are the interstices surrounding the location of the center sphere. A large region of

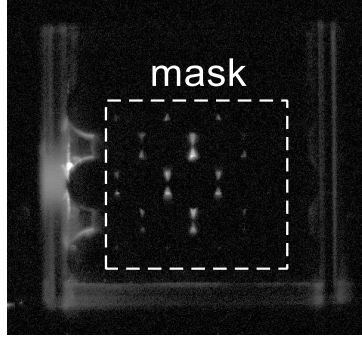


Figure 4.8: A background-subtracted recorded image when a luminescent sphere is located at the packing center. The white rectangle denotes an intensity-masked region inside which only analysis occurs. This figure is reproduced from XUAN et al. (2024).

the image is dominated by luminescence from the glass and camera read-out noise, appearing as dark noise areas. Consequently, for analysis purposes, only a subregion or mask, denoted as M , at the center of packing was considered and an intensity filter was then applied over this subregion to isolate the phosphor luminescence signals.

For each of the two ratio frames, the filtered signals were accumulated over the entire subregions M to obtain a more robust value for the intensity ratio estimation:

$$\varphi(T) = \frac{\sum_{(x,y) \in M} I_1(T, x, y)}{\sum_{(x,y) \in M} I_2(T, x, y)} \quad (4.14)$$

where $I_1(T, x, y)$ and $I_2(T, x, y)$ are the filtered signals at pixel (x, y) for frame 1 and 2, respectively.

4.2.2 Extension to multiple luminescent spheres case

When multiple luminescent spheres are present in a packed bed, the luminescence emissions from each sphere overlap each other on the camera image and the individual temperatures can only be reconstructed if the contribution from each sphere is separated.

4.2. TEMPERATURE DETERMINATION OF LUMINESCENT PARTICLES IN AN OPAQUE PACKED BED

4.2.2.1 Separation of spatial and temperature variables in single sphere images

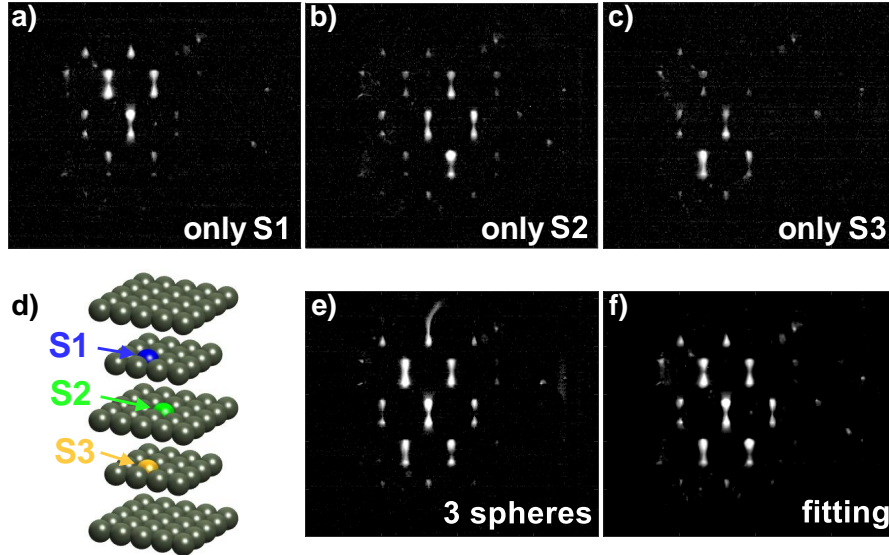


Figure 4.9: (a)-(c) The normalized images of individual signals of the spheres S1-S3 in configuration (d). (e) The compound signals of the three luminescent spheres and (f) the corresponding fitting. All the recorded images are the first one out of the frame pair. This figure is reproduced from XUAN et al. (2024).

Luminescence images obtained for the case of one luminescent sphere placed at three different positions within the bed are shown in Fig. 4.9(a)-(c). Each sphere position results in a specific spatial distribution of the intensity in the recorded image, and the strongest intensity area in each case is found to be related to the position of the projection of the luminescent sphere onto the imaging plane. For the single luminescent sphere case, we can assume that although the absolute signal may vary with temperature, the position-related relative spatial distribution is independent of temperature; in other words, the scattering properties in the packing have a negligible temperature dependence.

4.2. TEMPERATURE DETERMINATION OF LUMINESCENT PARTICLES IN AN OPAQUE PACKED BED

The measured signal $I_k(T, x, y)$ in Eq. (4.14) can therefore be expressed as a multiplication of temperature independent 2D intensity distribution function $S^{(j)}(x, y)$ for the j -th sphere and a temperature dependent factor $c_k(T)$ for the k -th frame, i.e.,

$$I_k^{(j)}(T, x, y) = c_k(T) S^{(j)}(x, y) \quad (4.15)$$

where the super-script j is omitted when only one sphere is considered; and $k = 1$ or 2 as we only have two frames.

Since the intensity spatial distribution is time invariant due to the fact that luminescence decays uniformly and isotropically, $S(x, y)$ of a fixed sphere j is identical for the two frames. Eq. (4.14) can therefore be simplified as

$$\varphi(T) = \frac{\sum_{(x,y) \in M} c_1(T) S^{(j)}(x, y)}{\sum_{(x,y) \in M} c_2(T) S^{(j)}(x, y)} = \frac{c_1(T)}{c_2(T)}. \quad (4.16)$$

If the intensity spatial distribution $S(x, y)$ of all the luminescent spheres are given, Eq. (4.15) and Eq. (4.16) allow to ignore the spatial dependency in the temperature evaluation and simplify the analysis. This opens the possibility to separate the signals from multiple luminescent spheres and hence to perform multi-point temperature measurements.

4.2.2.2 Linear regression to separate contributions from multiple luminescent spheres

Fig. 4.9(e) shows the luminescence image under isothermal conditions (room temperature) for a packing simultaneously containing 3 luminescent spheres at the positions designated in Fig. 4.9(d). These three positions correspond to that of the spheres in the image where only one sphere is present (Fig. 4.9(a-c)).

It can be observed that the individual intensity distributions are superimposed in the compound measurement with 3 spheres. The superimposition is a consequence

4.2. TEMPERATURE DETERMINATION OF LUMINESCENT PARTICLES IN AN OPAQUE PACKED BED

of the linearity of radiative transport (CHANDRASEKHAR, 1960) when higher order luminescence effects (i.e., luminescence and absorption induced by luminescent light) are ignored. In other words, the substitution of a non-luminescent sphere by one luminescent sphere has a negligible effect on the contribution of another sphere to the compound signal image, implying that substituting a sphere has no impact on the scattering/reflection or absorption properties of the bed. For the scattering/reflection properties, this independence is based on the fact that all other spheres than the luminescent spheres were also coated with non-luminescent paint to obtain similar scattering/reflection properties as mentioned in Section. 6.2. Regarding absorption, we measured the transmitted light through the bed using a photodiode placed along the beam path at the exit face. The transmitted light was found to change less than 2% whether no luminescent sphere or 5 luminescent spheres were placed in the beam path. No correlation between number of luminescent spheres and transmitted light could be found. We thus conclude that the substitution of a non-luminescent sphere by a luminescent sphere does not change the excitation light field through the bed.

Under the assumptions from the previous section that temperature only affects the absolute luminescence intensity but has a negligible impact on the spatial distribution, all pixels in the recorded image have the same linear dependence, i.e., Eq. (4.15) holds. We then have for a setup with N luminescent spheres that

$$I_k(T, x, y) = \sum_j^N I_k^{(j)}(T, x, y) = \sum_j^N c_k^{(j)}(T) S^{(j)}(x, y). \quad (4.17)$$

where $I_k(T, x, y)$ is the measurement for the k -th frame. The linearity of radiative transport implies that the individual contribution $I_k^{(j)}(T, x, y)$ of the j -th sphere to a measurement can be determined as the solution of Eq. (4.17).

Considering we typically have many more pixels $(x, y) \in M$ than unknown temperature contribution factors $c_k^{(j)}$ which number equals to that of the luminescent spheres N , Eq. (4.17) amounts to a least square problem in the $c_k^{(j)}$ with each pixel value

4.2. TEMPERATURE DETERMINATION OF LUMINESCENT PARTICLES IN AN OPAQUE PACKED BED

$I_k(T, x, y)$ providing one measurement and the $S^{(j)}(x, y)$ forming the columns of the input data matrix. Since the linear system is highly overdetermined, one expects that an accurate reconstruction of the $c_k^{(j)}$ is possible. The condition number of the system, which describes the amplifications of errors in the inputs $I_k(T, x, y)$ when solving for the $c_k^{(j)}$, allows one to quantify the attainable accuracy. This will be discussed later in the Section. 6.5.2.3.

The spatial intensity distribution functions $S^{(j)}(x, y)$ that provide the data matrix can be obtained from normalized luminescence images when only one luminescent sphere is present in the packed bed, cf. Fig. 4.9(a)-(c). Least square fitting of the compound intensity distribution of multiple luminescent spheres using Eq. (4.17) for both frames results in the temperature contributing factors $c_1^{(j)}(T)$ and $c_2^{(j)}(T)$. The temperature of the j -th individual luminescent sphere can then be determined by the intensity ratio $\varphi(T)$ given in Eq. (4.16).

An example of the least squares fit for the configuration in Fig. 4.9 can be seen in Fig. 4.9(f), which is of high agreement with the measurements. Note that here all the estimated $c_1^{(j)}(T)$ are approaching 1 as expected, since the individual signals and the compound signals are at the same temperature.

The least squares signal separation method described above necessitates templates of 2D spatial distribution function $S^{(j)}(x, y)$ for individual particles. A possibility to obtain the $S^{(j)}(x, y)$ template is to build a library by collecting the normalized intensity distribution data for all the locations by dis- and re-assembling the experimental apparatus with always one luminescent sphere in all possible positions. Ensuring reproducibility, e.g. that spheres are located at the same position, is already highly challenging in a simple setup such as those in Fig. 4.9 and it becomes impossible in complex, irregular packing. In Section. 6.5.2, we therefore discuss how the $S^{(j)}(x, y)$ templates can also be obtained using numerical ray tracing simulations of the light propagation.

5

Demonstration of high spatial resolution temperature measurements in fluid flows based on individual dispersed particle imaging

This chapter presents the application of the concept of individual dispersed particle imaging to resolve the temperature distribution in fluids, especially near the wall, with a two-dimensional high spatial resolution. Three main experiments implementing the spectral separation method are included: the first is conducted by dispersing micron-sized phosphor particles in water under uniform temperature settings to evaluate the accuracy of discrete temperature readings obtained from individual particles; the second is carried out, in which phosphor particles are this time seeded in a large gas flow and additionally illuminated by an LED light with a different emission spectrum than the phosphor particles; finally, measurements are performed in a thin thermal boundary layer that formed between a cold wall and a hot air flow in order to examine the ability to obtain high resolution temperature measurements near walls. Moreover,

precisions in spectrally separated intensity ratios from different two-colour imaging configurations are also compared and analyzed. At the end of this chapter, some test-cases exploring alternatives to applying the dual-frame lifetime method are discussed. The work in this chapter is partly derived from the publication XUAN et al. (2023).

5.1 Experiments applying the spectral separation method

The demonstration experiments are primarily carried out on the basis of the spectral separation method, as it is the typical method for ratio-based thermometry techniques. The main purpose is to demonstrate the capability of the proposed concept in resolving the temperature distribution in a thermal boundary layer.

5.1.1 Choice of thermographic phosphor particles

Two types of phosphor particles were employed as dispersed tracers to enable spectral separation method. The first one is a tin-doped phosphor $(\text{Sr,Mg})_3(\text{PO}_4)_2:\text{Sn}^{2+}$ (hereafter referred to as SMP: Sn^{2+}), which has been characterized in FOND et al. (2019) for temperature measurement. This phosphor offers a good level of temperature sensitivity (0.6 %/K at room temperature with the filter combination used in FOND et al. (2019)), and its intensity ratio shows very little sensitivity to excitation laser fluence (corresponding to 0.6 K for 10 % change in fluence). However, the long lifetime ($\sim 26 \mu\text{s}$) of this phosphor when seeded in the very fast fluid would result in an image with streaks. Interestingly, these streaks were utilized in a recent velocimetry concept (FAN et al., 2021, 2022). Although it would be possible to derive two-colour ratios too by fitting streaked images, for simultaneous thermometry and velocimetry, this is not the focus of our work; thus we restrain the use of SMP: Sn^{2+} to the slow flow in the liquid dispersion and bulky seeded gaseous flow cases.

5.1. EXPERIMENTS APPLYING THE SPECTRAL SEPARATION METHOD

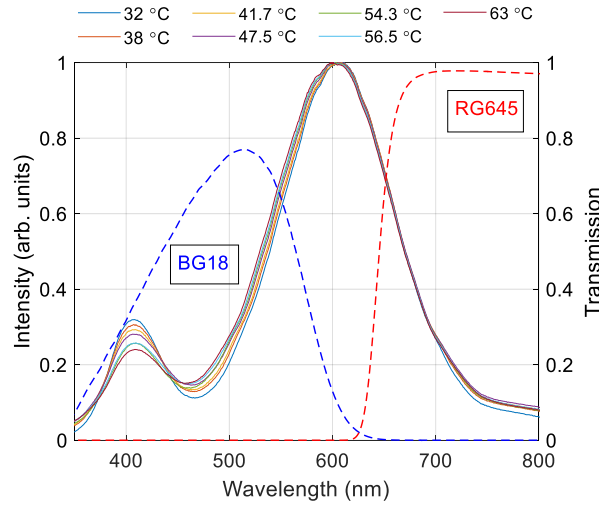


Figure 5.1: Normalized spectra of $2 \mu\text{m}$ SMP:Sn²⁺ particles dispersed in water from 32 to 63 °C, superimposed with the filter transmission curves used in this study. This figure is reproduced from XUAN et al. (2023).

The emission spectrum of SMP:Sn²⁺ dispersed in water is plotted in Fig. 5.1. From 32 °C to 63 °C, this phosphor spectrum broadens by approximately 8 nm on the blue side. The transmission curves of the colored glass filters utilized in this study (blue: BG18 and red: RG645) are also shown. This filter combination provides in theory a greater signal collection (+ 60 %), as computed via spectral curve convolution, but a lower temperature sensitivity (0.45 %/K) than the filters (Edmund 84113 and RG645) used in FOND et al. (2019), leading to a slight improvement in temperature error performance.

The second phosphor used was ZnO. Its emission spectrum in gas phase is shown in Fig. 5.2, which is reproduced from ABRAM et al. (2015). ZnO has a short luminescence decay time (< 1 ns) and is therefore applicable to fast gas jets. The structural and luminescent properties of the submicron ZnO particles have been described in ABRAM et al. (2015). In contrast to SMP:Sn²⁺, ZnO particles display a broad emission band peaking at 387 nm at room temperature, which gradually broadens and red-shifts as the temperature rises. The very same filters applied in ABRAM et al. (2015), specifically a 387-11 and a 420-30 (notation center wavelength and full width half maximum in

5.1. EXPERIMENTS APPLYING THE SPECTRAL SEPARATION METHOD

nm), were also used in this study. It was reported that this filter combination would produce a temperature sensitivity in the range from $\sim 0.6\%/K$ at 300 K to $\sim 2\%/K$ at 500 K (ABRAM et al., 2015).

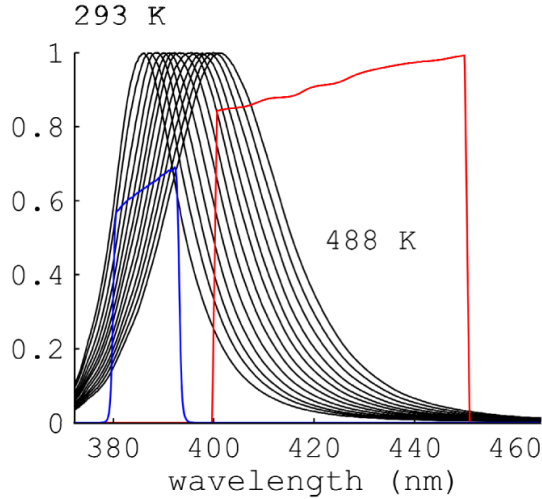


Figure 5.2: Normalized spectra of ZnO in the gas phase from 293 to 483 K, plotted with the filter transmission curves used in this study. The temperature interval between curves is 15 K. This figure is reproduced from ABRAM et al. (2015).

Particle-based thermometry relies on the ability of the seeded particles to reach thermal equilibrium with their surrounding fluid much faster than the temperature fluctuations of the fluids. Heat transfer at the particle-fluid interface is limited by heat conduction through the fluid layer due to the low Reynolds number of the particles, and its higher thermal conductivity (ABRAM et al., 2018). Additionally, as the thermal conductivity of phosphor particles is typically orders of magnitude larger than fluid conductivity, it can be assumed that the temperature inside the particle is uniform. The 95 % temperature response time (t_{95}) is a critical quantity for assessing the ability of the seeded particles to follow rapid fluid temperature changes. FOND et al. (2019) have estimated the 95% temperature response time (t_{95}) of SMP:Sn²⁺ particles to be about 70 μs and STRAUSSWALD et al. (2021) evaluated the t_{95} of the submicron ZnO particles to be about 5 μs , both at room temperature. ZnO particles are therefore better suited to track turbulent fluctuations of several kHz.

5.1.2 Preliminary demonstration of liquid dispersions

5.1.2.1 Experimental setup

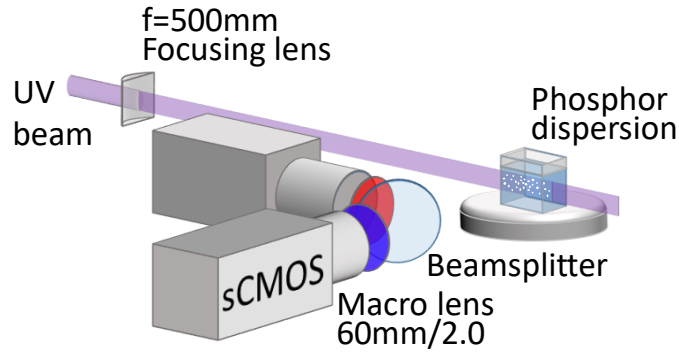


Figure 5.3: Optical setup for high-resolution particle imaging in liquid-phosphor particle dispersions, reproduced from XUAN et al. (2023).

For the first implementation of the concept, a dispersion of SMP:Sn^{2+} particles in water volume at uniform temperature was considered. The imaging setup is shown in Fig. 5.3. A 266 nm excitation laser sheet with a thickness of $150 \mu\text{m}$ and an energy fluence of about $35 \text{ mJ}/\text{cm}^2$ was formed to be directed through the liquid particle dispersion, which is contained within a fused silica cuvette that is placed on a stirring/heating plate. A stirring bar was placed at the bottom of the cuvette to ensure that the particle concentration and the temperature were uniform throughout the cuvette. Using a water dispersion offers better control over the concentration of particles than a gas jet but the temperature range is limited. For all the experiments in this chapter, a magnification of approximately 0.6 was achieved by the macro camera objectives without extension rings, leading to a pixel projection size of about $10 \mu\text{m}$. The objective lenses were operated at maximum aperture to maximise signal collection, giving a focus depth of field defined on the pixel size ($6.5 \mu\text{m}$) of $90 \mu\text{m}$, which was a slightly less than the laser sheet thickness. The both cameras were running in rolling shutter mode, with a total exposure time for the lines of 35 ms and a common exposure time for all lines of 5 ms. The laser pulse was synchronized so that the luminescence emission

occurred during the common time. Note that the effective signal collection duration is dictated by the luminescence decay time or by the laser pulse duration, whichever is the longest. Such pseudo global shutter mode, yields a lower readout noise below $2e^-$ and reduces the occurrence of hot pixels compared to the actual global shutter mode.

5.1.2.2 Results

The temperature of the dispersion in the cuvette was set to five different levels in the 33-75°C range. A sequence of about 200 fitted particles was collected at each temperature, and intensity ratios of the blue to red channels were then calculated. For each temperature, the average and standard deviation of the particle ensemble ratio were determined. It is presumed that the temperature remains constant throughout the cuvette since the liquid dispersion is constantly being stirred. The mean measured ratios are plotted as a function of temperature in Fig. 5.4, with the error bars derived from dividing the particle-to-particle ratio standard deviations by the square root of the total particle number at each temperature. The ratios rise monotonically with temperature, which is to be anticipated given that the emission spectra of tin-doped phosphor blue-shifts with increasing temperature. A linear fit was applied over this small temperature range to derive the temperature sensitivity at 50°C of 0.35%/K. This sensitivity is as expected lower than the value reported in FOND et al. (2019) because of the different filters used. Ratios were also derived from spectral integration of the emission spectrum and the filters transmission (as shown in Fig. 5.1) convoluted with the reflection/transmission ratio of the beamsplitter (not shown). The resulting ratios are plotted in Fig. 5.4 as well. The absolute values of the ratio differ from measurement, as expected due to differences in gain between the cameras and uncertainties in the absolute transmittance of the filters and beamsplitter. However, a similar level of sensitivities is achieved, with that of the spectral ratios is 0.27%/K which is slightly lower than the value for the ratio obtained from particle image fits. It should be noted that in-situ calibration data is always preferable to convert ratio to temperature data

5.1. EXPERIMENTS APPLYING THE SPECTRAL SEPARATION METHOD

in actual experiments as discussed in ABRAM et al. (2018) (Section 3.4). The results confirm that the fitting approach yields similar results to the conventional approach in terms of sensitivity.

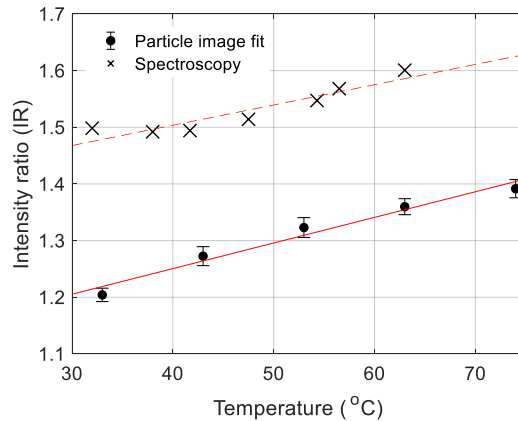


Figure 5.4: Ratio calibration curves for the phosphor SMP:Sn²⁺ in liquid dispersions: measured intensity ratios obtained from 2D particle image fitting; the theoretical ratios derived from spectral convolution of emission spectra, filters transmission in both channels and beamsplitter transmission/reflection ratio. This figure is reproduced from XUAN et al. (2023).

The ratio precision of particle-to-particle standard deviation to the mean ratio was also estimated for the measurement, ranging between 12 to 13.5%, which corresponds to a temperature precision of 34K to 38K. This random variation is actually larger than that of the window-based thermographic PIV method (~ 4% at a resolution of 400 μ m, see Fig.5 in FOND et al. (2015)) due to the overall much weaker signal, since only one particle is probed as opposed to several tens of particles for the latter. Examining the distributions of total particle intensities, the median value in transmission is 3500 counts, and in reflection it is 2700 counts, resulting in a theoretical precision of 4.3% based on the random uncertainty analysis in FOND et al. (2015).

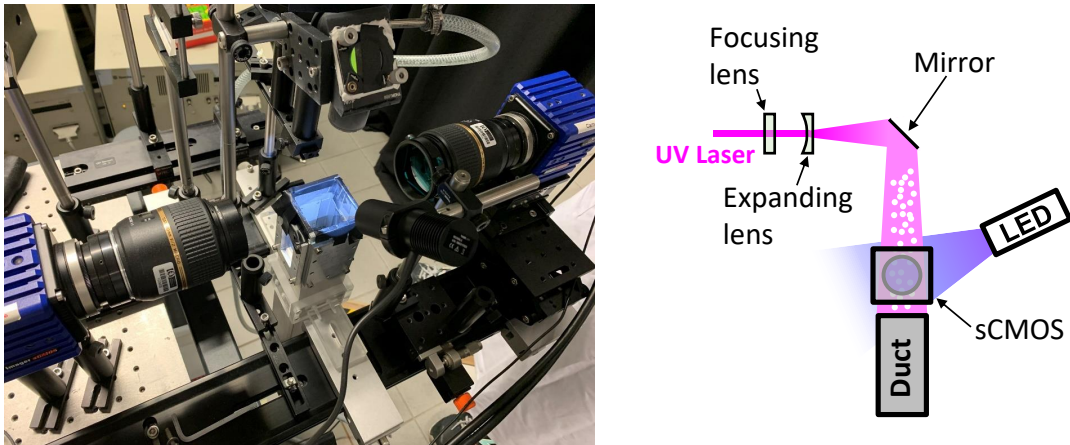


Figure 5.5: Picture and schematic of the optical setup used to test the effect of re-scattered LED emission.

5.1.3 Rejection of multiple scattering interference

5.1.3.1 Experimental setup

A second demonstration experiment was performed in a low velocity (approximately 1.2 m/s) seeded gas flow at room temperature which was illuminated by an additional LED light source to test the ability of the method to reject re-scattered luminescence. The illustration of this experiment is shown in Fig. 5.5. SMP:Sn²⁺ particles were here seeded into the 70 × 45 mm duct, with an exit velocity of approximately 1.2 m/s. Compared to the previous imaging system employed in the liquid dispersion experiment, the imaging setup was adjusted by propagating the laser vertically along the jet axis to minimize reflection of a surface placed perpendicular to the jet exit. Moreover, an additional $f = -500$ mm expanding lens was installed to enlarge the laser sheet in the vertical direction in order to create a more steady energy fluence by using only the center-part of the expanding excitation laser sheet.

An uncollimated LED light source (from Thorlabs MCWHL5, see Fig. 5.6(a)) was positioned slightly above the camera field of view and oriented towards the imaging

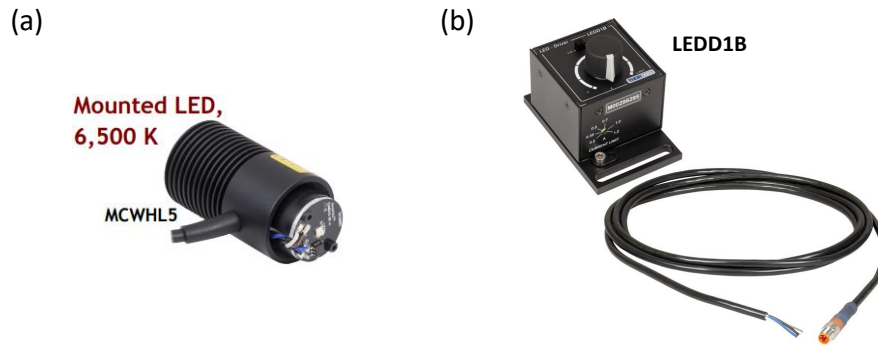


Figure 5.6: The applied LED lamp and its controller. These two figures are reproduced from <https://www.thorlabs.de/>.

region at the outlet of the flow section to provide a continuous illumination over a large volume seeded with particles. This caused the LED light to be re-scattered by particles in front of and behind the thin UV light sheet to produce out-of-focus signals, similar to a configuration in which the laser strikes a surface with deposited particles, causing surface signal re-scattered by particles as in ZENTGRAF et al. (2017). This scattering light would result in a low spatial frequency interference signal contributing to the luminescence detected in-focus. To modulate the intensity of the interfering light, an LED Driver (Thorlabs LEDD1B) as shown in Fig. 5.6(b) was used to power the LED at constant current, with input currents ranging from 0 to 1 A, corresponding to an output power range of 0 to 840 mW as measured by a power meter. To avoid that the large gas flow may stretch the membrane of the pellicle beam splitter and thus affects image quality, we opted for the system with cameras on the opposite side of the light sheet. In addition, since a beamsplitter system would naturally reduce the signal-to-noise ratio as it splits the signal intensity in half, a configuration with two cameras situated on opposite sides of the laser sheet was thereby used instead.

The employed LED and seeded phosphor, SMP:Sn^{2+} , both have a broad emission spectrum but peak at different positions as shown in Fig. 5.7(a), so when imaged by the two-colour system, their emissions result in different intensity ratios. Due to the fact that the blue channel (low-pass band) spans the entire LED emission range,

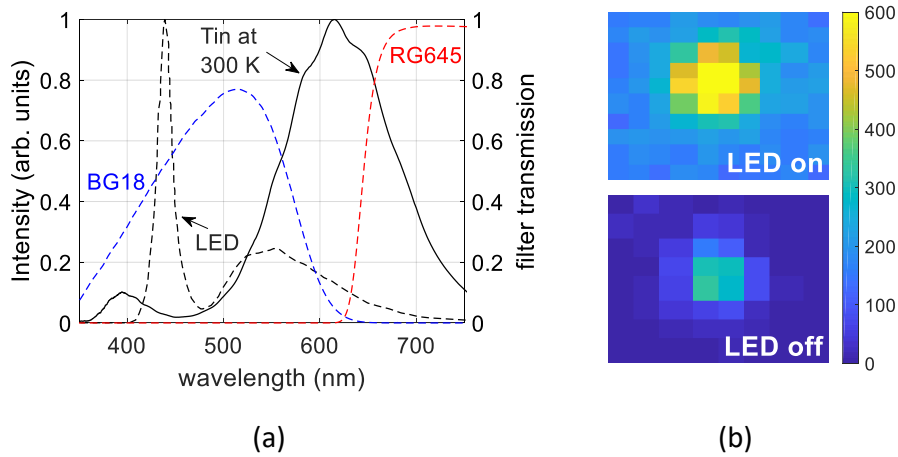


Figure 5.7: (a) Emission spectrum of interfering LED plotted together with the filter transmission curves and SMP:Sn²⁺ emission spectrum at 300 K. (b) An example of the single particle image with LED on and off recorded in the BG18 channel, after subtracting the LED background (unseeded flow, LED on). This figure is reproduced from XUAN et al. (2023).

a substantial amount of interference was observed in the recorded particle images collected from this channel, as shown in Fig. 5.7(b). Note that the constant background level resulting from LED reflection on solid surfaces was evaluated with LED on but without laser and seeded flow, and subtracted to the raw images. However, with laser on and particles seeded, after that subtraction, there is still some "offset" signal due to re-scattering of the LED emission by seeded particles. This interference depends on the particle seeding density. A contribution from the LED light will cause the apparent ratio to diverge from the value obtained with UV illumination alone. In this way, the LED light source mimics the luminescence of particles outside the measurement volume which are at a different temperature than those in the measurement volume, similar to those depositing for example on a hot or cold surface. The ratio of blue to red channel derived from spectral convolution is 10 for the LED emission only as opposed to 1.5 for phosphor luminescence. This setup enables the evaluation of the contribution from multiply scattered light to the temperature measurements and so the capability to exclude it.

5.1.3.2 Results

The results of the experiments with an additional light source (LED) which is multiple re-scattered by a large seeded flow towards the camera are presented in this section. Particle images were recorded at 6 LED output levels at room temperature. They were then fitted and the term I_c in Eq. (4.8) is thus extracted in both frames for each particle. The mean value of the multiple scattering interferences represented by I_c accumulated over 5000 particles is plotted as a function of LED power in Fig. 5.8. Since the LED light would also be reflected and scattered by the surrounding surfaces, such as the fluid pipe wall, and contribute to the signals collected by the camera, the background images in the absence of the particles but with the LED light on were recorded and subtracted to the particle images during the pre-processing.

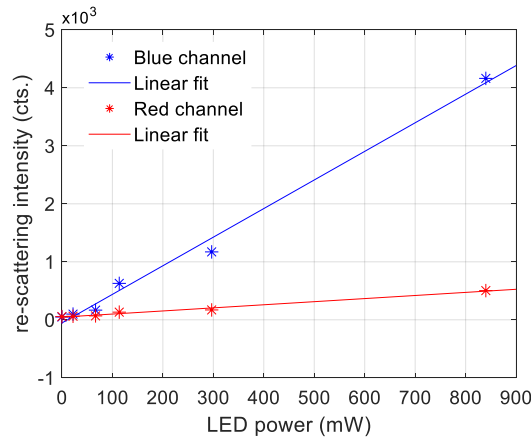


Figure 5.8: Contribution of re-scattered LED emission at different LED output level power, reproduced from XUAN et al. (2023).

As shown, the evaluated multiple scattering increases linearly with the LED power. Compared to the red channel, the blue channel suffers more interference owing to its greater overlap with the LED spectrum, as discussed in Section. 5.1.3.1. To provide an estimation for the relative contribution of re-scattered light and particle luminescence, the average intensity of the particle luminescence over the 9×9 fitting area is compared to the interference term that represents the re-scattered signals. At the maximum LED

5.1. EXPERIMENTS APPLYING THE SPECTRAL SEPARATION METHOD

output power, the re-scattering to particle signal ratios for the blue and red channels are as high as 20 and 3, respectively.

Next, to examine the ability to separate the particle luminescence from the re-scattered LED light, ratio maps produced by this technique are plotted in the top row of Fig. 5.9 where each point is positioned at the particle center position, and the colour corresponding for its ratio. Although the number of points varies because the seeding density cannot be held constantly between the test, the value of the ratios differ very little with the LED power increased.

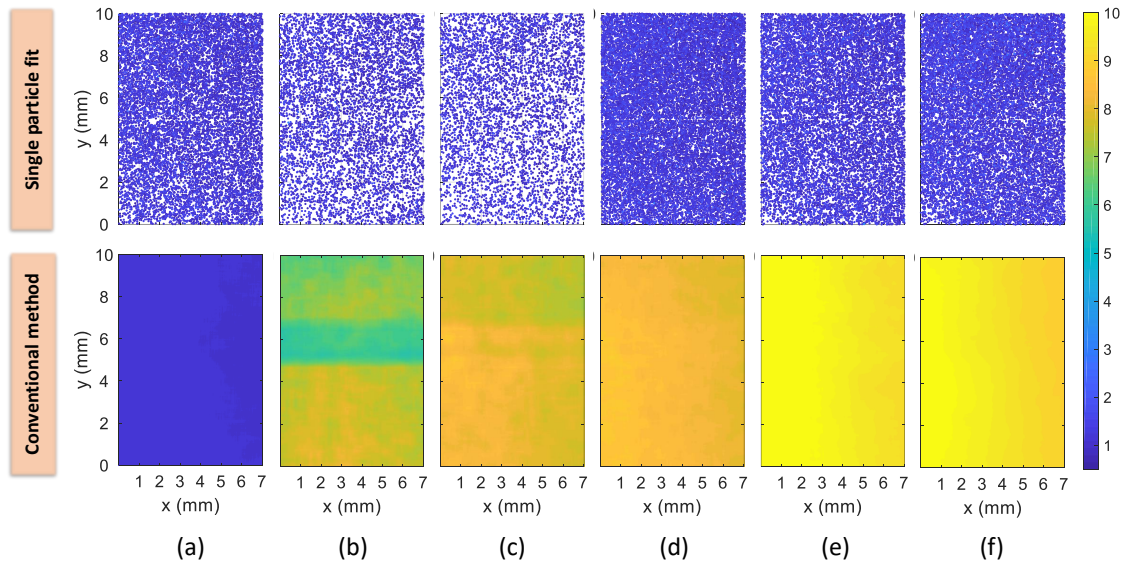


Figure 5.9: Ratio maps obtained from the single particle fit technique and the conventional method (window-based) for different LED output powers (a) 0mW, (b) 22mW (0.2A input), (c) 67mW (0.4A input), (d) 114mW (0.6A input), (e) 297mW (0.8A input), and (f) 840mW (1A input). This figure is reproduced from XUAN et al. (2023).

The luminescence particle images are also processed using the conventional method (window-based). Background-subtracted particle images were overlapped to correct the displacement and smoothed with a moving average filter of 10×10 pixels window size before direct division. The bottom row of Fig. 5.9 presents the resulting ratio maps for the different LED output powers. In the absence of LED light, the two methods yield very similar ratios. However, when the LED is turned on, the ratios from

the window-based method rise significantly, even at a low output power of 22mW, with a more than 6-fold rise compared to the ratio without LED in the majority of areas. This rise in ratio indicates a contribution from the LED emission which is re-scattered by the particles, in agreement with the consideration of spectral overlap between LED emission and filter transmission curves shown in Fig. 5.7. Indeed such low spatial frequency contribution is included in the signals which are divided in the window-based method. With the LED power increasing, recorded signals are gradually dominated by scattered LED, so the results head towards the intensity ratio between spectrally separated LED emission (approximately 10 from Section. 5.1.3.1).

Statistical information obtained from both methods on a per-particle basis can give more insight into the ratio bias induced by the LED light. To facilitate the comparison, the intensity across a 9×9 window around each detected particle is summed up in blue and red channels to calculate the single particle ratios from the window-based technique. Note that this summation approach is more favourable than the window-based approach because only the signals around the particle center are considered, where the luminescence to scattered LED emission ratio is the highest. Fig. 5.10 presents the resulting distribution derived from both fitting-based and window-based methods with LED off and at the maximum power of 840mW. As shown, the distribution from the particle image fitting technique shows a 6% bias in the mean intensity ratio (IR), indicating a robust capacity to reject interference. A minor rise in the particle-to-particle standard deviation (STD) occurs in the presence of LED signal due to a lower signal-to-noise ratio after the subtraction of a high background signal. In contrast, for the sum-based method, the mean intensity ratio (IR) is around 6 at the maximum LED output. This value, although well below the value from the direct window-based technique of around 10, is about a 6-fold rise with respect to the LED off case. In terms of temperature, this would correspond to a difference of more than 700K. The standard deviation (STD) here without LED is larger than the water dispersion findings attributed to potential agglomeration in the gas phase. It is worth noting that, when

the LED is off, the standard deviation for the ratios derived from the sum intensity is lower than that of the fitting method. This can be due to the non-Gaussian character of the images, which leads to imperfect fitting. In the future, filtering based on a fitting quality criterion will be implemented to minimize fitting errors.

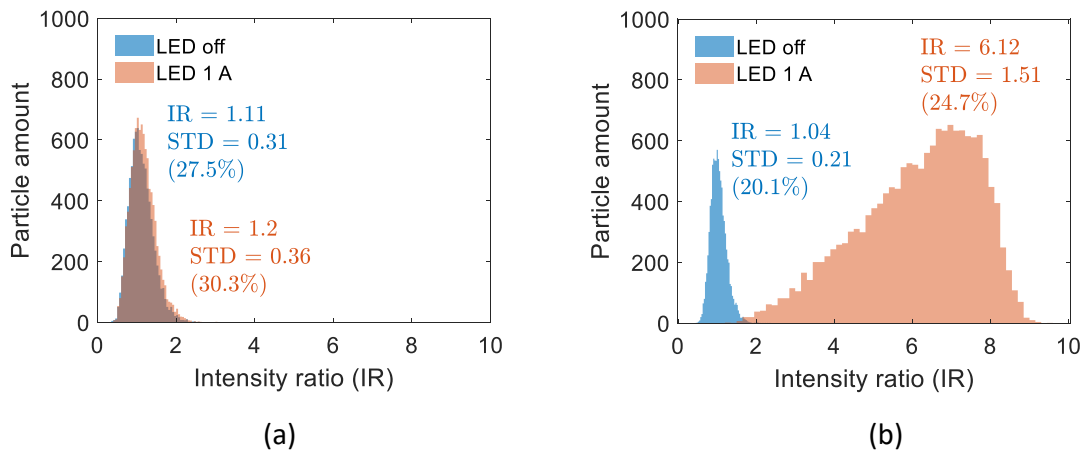


Figure 5.10: Single particle intensity ratios distribution with LED off and at maximum power based on (a) the single particle fit technique and (b) the window-based method. This figure is reproduced from XUAN et al. (2023).

5.1.4 Temperature measurements within thermal boundary layers

5.1.4.1 Experimental setup

Following the above demonstrations, the temperature measurements were carried out in a thin thermal boundary layer formed between a heated flow and a cooled wall, as the figure of the experimental setup shown in Fig. 5.11. In this case, both high spatial resolution and rejection of wall signals play a critical role in observing the sharp temperature gradients in the vicinity of the wall.

An air flow seeded with ZnO particles passed through a 1 m long, 10 mm inner diameter pipe that was wrapped by a winding fiberglass heater (Omega Engineering, STH-SST-SWH) to provide an exit jet temperature of up to 470 K. In order to create a

5.1. EXPERIMENTS APPLYING THE SPECTRAL SEPARATION METHOD

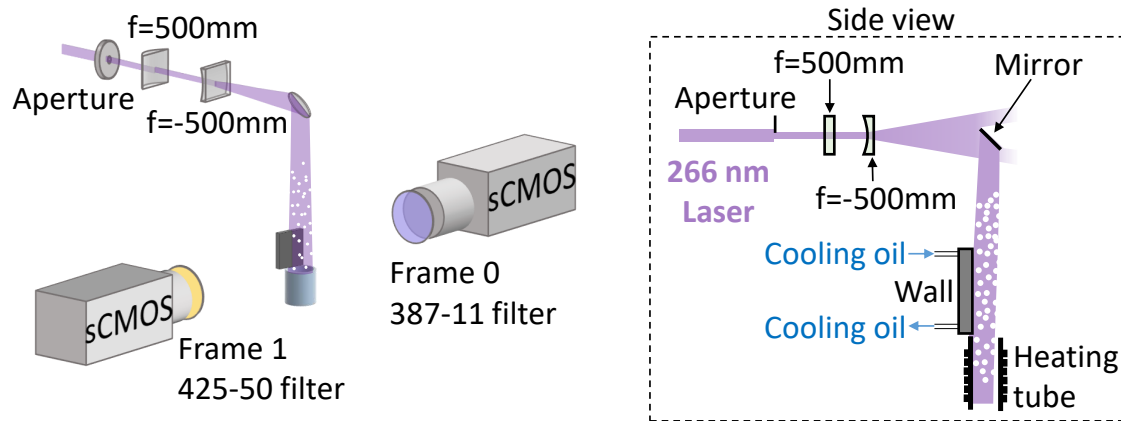


Figure 5.11: Side view of the optical setups for resolving temperature profile in a thermal boundary layer.

thin thermal boundary, an aluminum plate was placed 1.5 mm above the air exit with its surface being positioned to be parallel to the flow direction and exactly tangential to the edge of the seeded tube. This plate was actively cooled at 300 K by an inner serpentine circuit that circulated a temperature-controlled silicone oil, in analog to the heating unit that described in DRAGOMIROV et al. (2018). For the purpose of minimizing the reflection signal from the surface, the plate was painted with a non-luminescent black primer. The hot seeded air was in this way forced to flow over a surface that remained cold, generating a strong temperature gradient near the wall to test the possibility of interpreting the temperature profile within it.

To reach a sufficiently thin boundary layer, the exit jet velocity was set to be 7.5 m/s at the ambient temperature. The Reynolds number with the characteristic length defined as the inner pipe diameter of 10mm was 4750 at the jet exit, which is in the fully turbulent flow regime to achieve a top-hat temperature profile at the jet exit rather than a parabolic one. The camera imaged the flow between the heights of 0 and 2cm along the wall. Considering the position of the highest distance to the leading edge within the field of view as the characteristic length, the Reynolds number is below 9300 being characteristic of the laminar thermal boundary layer regime. Here although the main flow is turbulent, the boundary layer developing near the cooled surface is assumed

to remain laminar. The pipe length (1m) is long enough to allow for fully developed turbulent pipe flow so that the turbulence intensity at the pipe exit is estimated to be approximately 5% (PENNELL et al., 1972). On the other hand, the cooling wall is positioned directly at the exit, with its plane tangent to the pipe's inner circle and parallel to the pipe axis, preventing the formation of an adverse pressure gradient. Therefore perturbations to the laminar boundary layer are expected to be negligible.

During this measurement, the two cameras were also placed on opposite sides of the measurement plane, as in the previous one experiment. An additional aperture was added on the beam path before the expanding lens to use only the central part of the laser beam. Since the beam has a near-Gaussian intensity distribution, the aperture helps minimize the fluence variations, which have a stronger effect on ZnO than on the SMP:Sn²⁺ phosphor because the ZnO is more susceptible to the excitation fluence as demonstrated in ABRAM et al. (2015); FOND et al. (2019).

5.1.4.2 Results

Fig. 5.12(a) presents an example of the recorded luminescence image of the seeded flow. The laser sheet was oriented to propagate almost vertically but with a small angle against the cooled wall, such that upon laser irradiation, the line of the intersection between laser and wall would form a visible light band in camera image. The wall location was then determined in the absence of seeded jet by locating the highest intensity along this band. A coordinate was defined by specifying the leading edge position as the origin ($x = 0$ mm and $y = 0$ mm). Before further processing, the image was cropped to a sub-region (red dash rectangle) that was 3 pixels away from the detected wall including the majority of the seeded jet while exactly excluding the wall surface, and this sub-region extends over about 9×18 mm.

During the fitting, particle intensity data outside the 9×18 mm areas would be ignored when the processed particle in the near-wall regions is close to the boundary

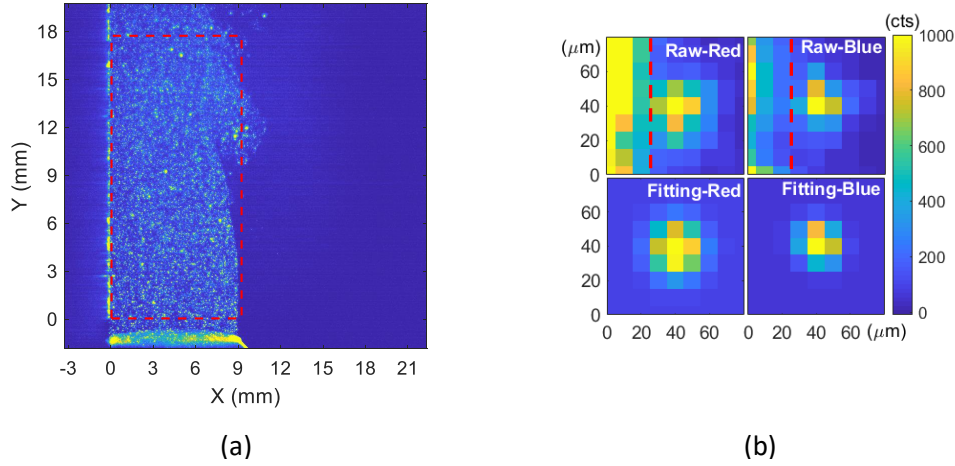


Figure 5.12: (a) Raw particle image of flow in the boundary layer experiments. The processed sub-region is indicated by red dashed rectangles that is 3 pixels away from the detected wall; (b) an example of near-wall particle frame pair and their fitting results. The gray regions are the discarded input data in the fitting. This figure is reproduced from XUAN et al. (2023).

of the cropped sub-region. An enlarged view of an example particle is shown in Fig. 5.12(b). As shown, the contribution of the wall signal is considerable, with the interference I_c estimated to be around 400 counts in the red channel and 300 counts in the blue channel for this particle. In spite of the interference, the fitting exhibits robust performance since it provides a very good match to the recorded intensity distribution in both channels. The shown particle can therefore be used to detect temperature very near to the wall surface, within $40\mu\text{m}$ here.

We now address the ratio to temperature conversion. Fig. 5.13 shows a calibration curve from ABRAM et al. (2015) that was obtained with the same spectral filter combination as in our system, but using a flat plate beamsplitter. The ratios were normalized to 300K and fitted by a power law function. Here due to the difference in laser fluence, in the magnification of the imaging systems and the absence of the beamsplitter, it is possible that a different calibration curve will apply. The measurements were therefore carried out with the current system at two distinct jet exit temperatures (114°C and 195°C) in addition to room temperature. Ratio statistics were accumulated over

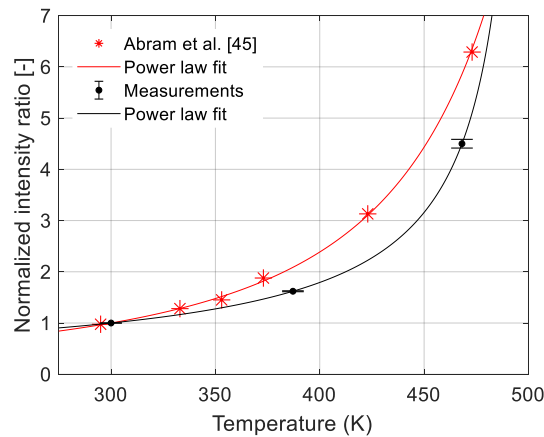


Figure 5.13: ZnO temperature - ratio calibration curve, obtained from Ref. ABRAM et al. (2015) and from the present study. Both data sets are fitted by power law functions of the form $a + b \cdot IR^c$, with IR the normalized intensity ratio. This figure is reproduced from XUAN et al. (2023).

particles located in the central region of the jet, and the average ratio was calculated at each temperature. After normalizing to 300K, the ratios at these three temperatures are also plotted in Fig. 5.13. The error bars for each temperature data in the figure indicate the particle-to-particle ratio standard deviation divided by the square root of the total number of particles. As expected, the fitted curve does not precisely match the previous calibration curve. We therefore applied a power law fit to the three recorded data points which was then used for temperature conversion.

Next, using the single particle fit technique, an example of discrete temperature field obtained from an instantaneous image containing 111 particles can be found in Fig. 5.14(a), with each particle representing an independent temperature measurement point. It should be noted that no post-processing filters were applied to the derived data, e.g. median filter, causing outliers to remain in the results. Due to the uneven laser fluence distribution in the laser sheet and the thermal quenching effect, weaker particles are present at the bottom of the image and in the high temperature regions. Therefore sparser measurements are obtained in the jet center area above the jet exit and in the near wall region till $y = 8$ mm. On the left side of the jet, we can clearly see

5.1. EXPERIMENTS APPLYING THE SPECTRAL SEPARATION METHOD

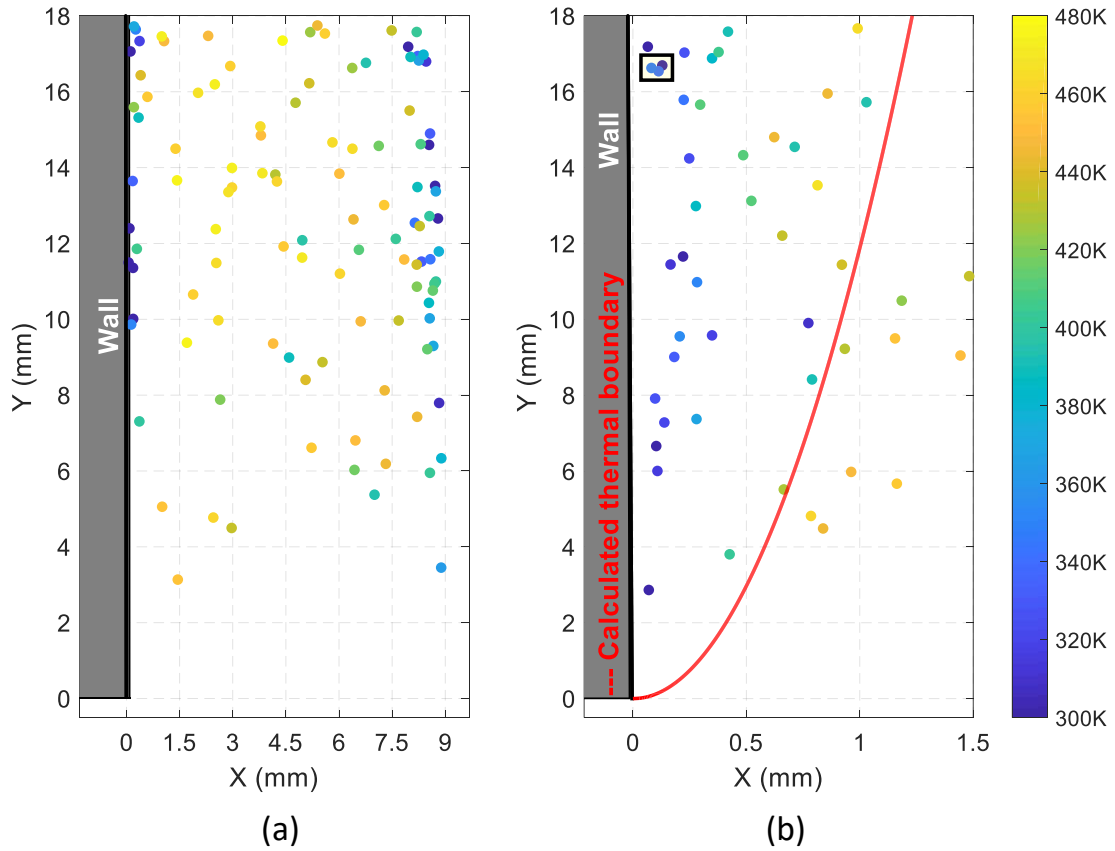


Figure 5.14: Single shot temperature field: (a) the full processed area and (b) a subset of the near-wall domain. The theoretical thermal boundary layer thickness is also plotted in red dashed line. This figure is reproduced from XUAN et al. (2023).

that a low temperature layer develops near the wall over the cooled surface, indicating a thermal boundary layer, while on the right side of the jet, heat transfer with ambient air leads to another thermal mixing layer.

To better visualize the temperature readings in the thermal boundary layer, a subset of the data in the near wall region (1.5mm away from the wall surface) is explored. Fig. 5.14(b) shows an illustration of a single-shot measurement of this subset, where 47 particles are present. In this figure, the x axis is stretched compared to the y axis. It can be found that particles as close as 0.1mm from the wall all indicate a low temperature below 350K which is close to the wall temperature as anticipated. The average distance

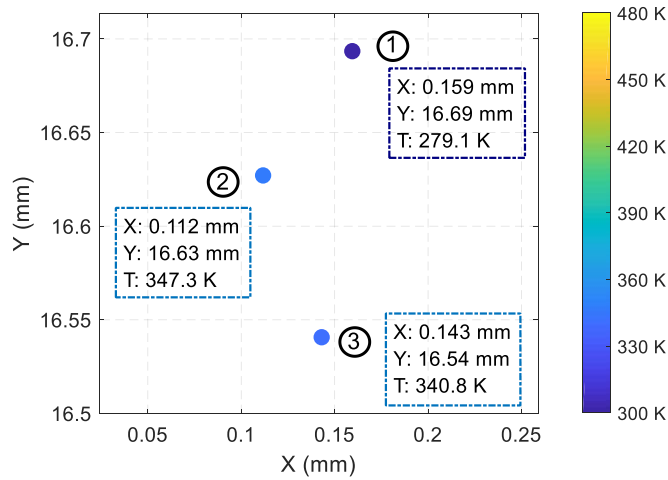


Figure 5.15: A zoom-in view of the three temperature measurements located in the marked rectangle in the upper left corner of Fig. 5.14(b)

between the probe particles of this single-shot measurement is $750\mu m$, with the closest particles in the marked rectangle in the upper left corner of Fig. 5.14(b). A zoom-in view of these three particle images is plotted in Fig. 5.15.

In spite of the temperature variation that indicates the technique precision, these three particles all imply a temperature below 350K since they are very close to the cooled wall. For the instantaneous measurement in Fig. 5.14(b), the minimum inter-particle distance or the minimum detection length is indicated by that between particle image 1 and 2, which is $76\mu m$.

Particle images were recorded over 100 laser pulses, which yielded a total number of 28500 processed particle images. The accumulated temperature field of the full processed area is shown in a scatter 2D plot in Fig. 5.16(a). As observed a large region within the hot jet has a uniform temperature because the flow is fully turbulent at the tube outlet, and thus has a top-hat exit temperature profile. The thermal mixing region with the ambient and the thermal boundary layer appear clearer in these accumulated plots. Again, here a focus in the near wall sub-region within 1.5mm from the wall is presented in Fig. 5.16(b), which includes about 5000 particles measurements. In the accumulated scatter plot, we can clearly see the sharp temperature gradient in the

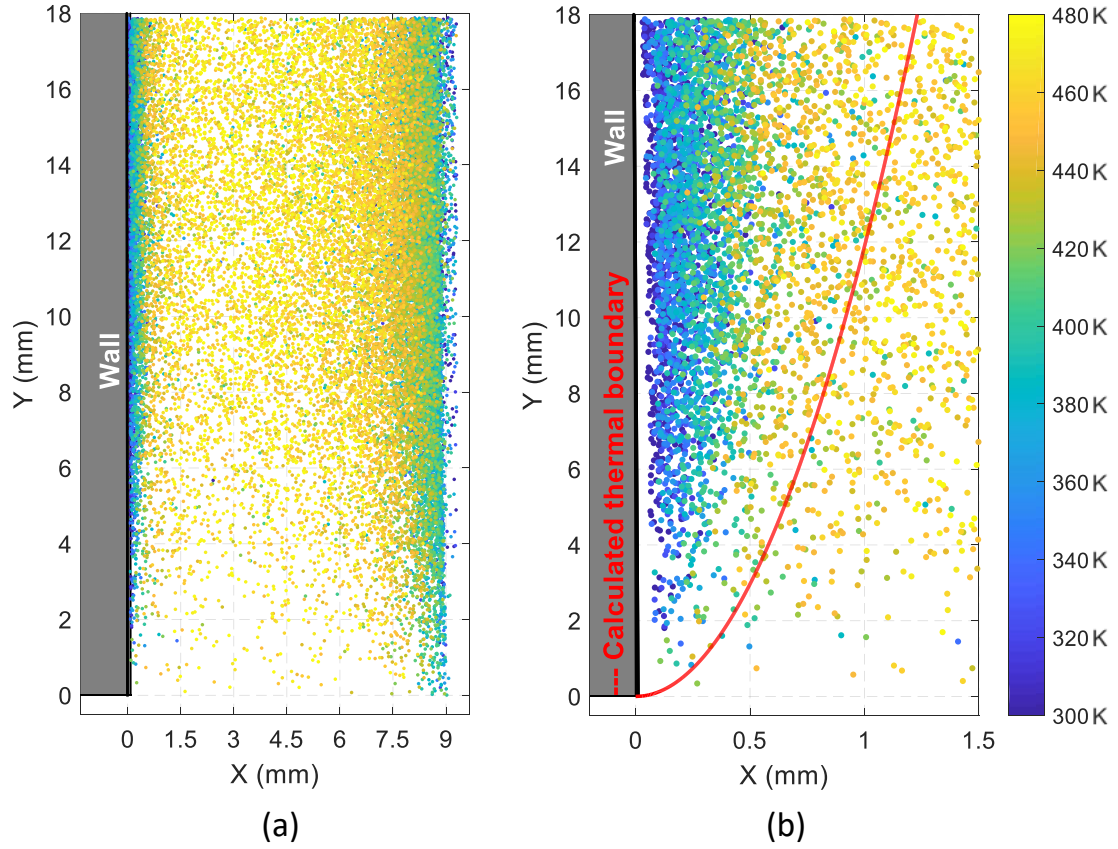


Figure 5.16: Temperature field obtained from accumulated measurements: (a) the full processed area and (b) a subset of the near-wall domain. The theoretical extent of the thermal boundary layer is also plotted as the red dashed line. This figure is reproduced from XUAN et al. (2023).

first $500\mu\text{m}$ near the wall. The width of this layer also increases with distance from the leading edge.

To validate the ability of this new approach to resolve this thin thermal boundary layer, the measured temperature data points are compared to a calculated temperature profile inferred from the laminar Prandtl-Blasius equation (CENGEL, 2004):

$$2\frac{d^2\theta}{d\eta^2} + Pr f \frac{d\theta}{d\eta} = 0 \quad (5.1)$$

5.1. EXPERIMENTS APPLYING THE SPECTRAL SEPARATION METHOD

where Pr is the Prandtl number, calculated here as 0.685 based on the average temperature of the free stream (470K) and the cooling wall (300K); f is the solution of Blasius-equation; θ is the dimensionless temperature defined as:

$$\theta(x, y) = \frac{T(x, y) - T_s}{T_\infty - T_s} \quad (5.2)$$

with \mathbf{x} representing the locations along the wall and \mathbf{y} denoting the locations normal to the wall. T_s is the wall surface temperature, which was maintained at about 300 K during the measurement. T_∞ is taken as the jet exit temperature in this study. Meanwhile, the similarity variable η in Eq. (5.1) is given as:

$$\eta = y \sqrt{\frac{u_\infty}{\nu x}} \quad (5.3)$$

with u_∞ set to be the jet exit velocity of 11.7m/s considering the thermal expansion. The kinetic viscosity ν here is computed also based on the jet exit temperature and simply assumed constant.

In addition, for $0.6 < Pr < 10$, the non-dimensional temperature gradient at the surface is found to be proportional to Pr , which can be written as:

$$\left. \frac{d\theta}{d\eta} \right|_{\eta=0} = 0.332Pr^{1/3} \quad (5.4)$$

Given the boundary condition $\theta(\eta = 0) = 0$ and $\theta(\eta = \infty) = 0$, the Eq. (5.1) can be numerically solved to obtain an equation for θ as an function of η alone. Therefore, the analytical temperature profile at any y position within the thermal boundary layer can be inferred.

Fig. 5.17 shows the calculated temperature profiles at $y = 6$ mm, $y = 12$ mm, and $y = 16$ mm, respectively, and the discrete temperature measurements were binned in 0.15 mm steps for comparison. The temperature sensitivity of ZnO is relatively low at room temperature or below it, so measurement variation is more pronounced than that at

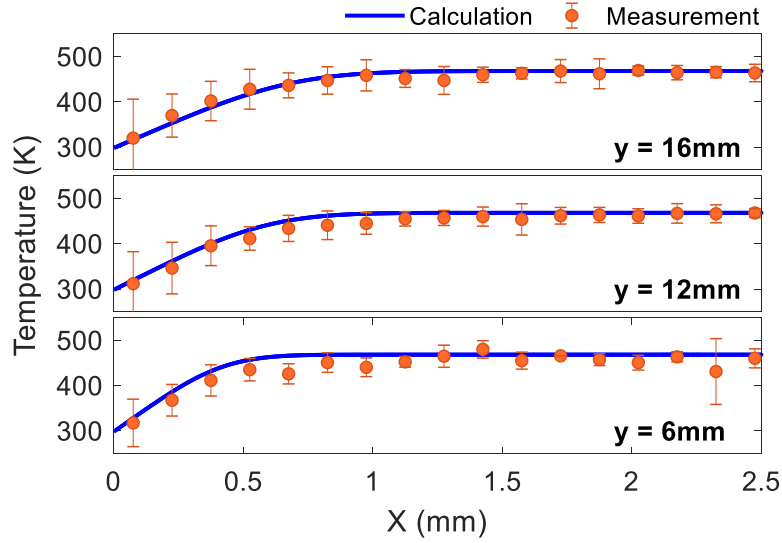


Figure 5.17: Comparison of the temperature profile in the thermal boundary obtained from this single particle fit thermometry technique and calculated using the laminar Prandtl-Blasius equation. This figure is reproduced from XUAN et al. (2023).

high temperature. Nevertheless, the average of the measured temperature matches the calculations very well with a maximum and an average deviation of 40K and 11K respectively. Such performance is attributed to two remarkable features of this fitting-based technique: it can reject the interfering environment near the wall which would otherwise bias the temperature detection. In addition, each measurement originating from individual micron size volume in space, is free of spatial averaging errors.

5.1.5 Analysis of ratio precision for different systems

In the previous discussion, experiments were conducted in two main imaging configurations, for two phosphor particles, dispersed in air or in water. In order to provide guidance on the optimum configuration, the measurement precision of each of those configurations was analyzed in this section. In addition, measurements were also performed in configurations that did not allow temperature measurements, for example,

5.1. EXPERIMENTS APPLYING THE SPECTRAL SEPARATION METHOD

without filters, or using the same filter on both cameras to check various hypotheses for error sources.

Table 5.1: The particle-to-particle standard deviation in ratios with SMP:Sn²⁺ particles seeded in the gas for two optical configurations at room temperature. Of the two, the pellicle beamsplitter configuration is also tested using different filters combinations or even without filters.

| Filters combination | Pellicle BS (95 % CI) | Opposite cameras (95 % CI) |
|---------------------|-----------------------|----------------------------|
| BG18 & RG645 | 19.5 (18.9, 20.1) % | 19.8 (19.4, 20.2) % |
| No filters | 15.4 (15.0, 15.8) % | - |
| Both RG645 | 10.3 (9.2, 11.4) % | - |
| Both BG18 | 16.7 (15.4, 18.0) % | - |

The analysis was firstly based on the SMP:Sn²⁺ aerosol. In the beamsplitter configuration, when two different filters (BG18 and RG645) are used as those configurations shown in Section. 3.2, the ratio precision is 19.5%, which is much larger than the noise limited precision of 6.1% obtained from the calculation method presented in Section. 3.2.4 of ABRAM et al. (2018). Emission anisotropy has little effect in this case since the light collection axis is the same for both cameras. However, there may be a potential contribution of particle-to-particle variations in the "apparent" emission color. Therefore, to test this hypothesis measurements were also performed with both cameras equipped with the same filters. Results are shown in Table. 5.1. Within the table, the temperature precision is inferred through the calculation of the standard deviation of the individual particle intensity ratio samples (σ), and this value is presented with a 95% confidence interval (CI) to account for statistical uncertainty. These confidence intervals are determined from the variance defined by Equation. 5.5, which offers a theoretical evaluation of the variance in sample variance ($Var(\sigma^2)$), taking into account the number of samples (n) and the mean precision ($\bar{\sigma}$). It is important to note that such calculations assume that the samples follows a Gaussian distribution (CHO und CHO, 2009).

$$\text{Var}(\sigma^2) = \frac{2\bar{\sigma}^4}{(n-1)} \quad (5.5)$$

When no filters are placed in front of either camera, there is only a minor improvement of the precision with respect to the reference filter combination (BG18 & RG645), which is in line with the interpretation above that the particle-to-particle emission variation mainly dominates the precision, despite a significant signal increase since both cameras can collect emission at a broader wavelength range. In addition, blue emitting dust particles will result in a different transmission/reflection ratio than phosphor particles for an unfiltered configuration situation, because of the spectral dependence of the beamsplitter. Similarly, scattered light, by its polarised nature, would also lead to reflection/transmission ratio variations with respect to direct particle luminescence. Notably, only the scattered luminescence is concerned here, since a prism was used to clean the laser line so as to remove a potential 532 nm contribution, and the objectives used would not transmit 266 nm scattered light.

The configuration with both cameras using the same red filter RG645 yields a near two-fold improvement of the precision compared to the reference configuration, from 19.5% to 10.3%, although there should be a small increase in random uncertainty due to the lower signal level provided by RG645 filter. This significant improvement again indicates that changes in the emission spectrum from one particle to the other largely contribute to the intensity ratio variation. Compared to the no filter case, using two RG645 filters also has better precision because certain interfering lights are blocked by the filters. Likewise, the counterpart with two blue filters BG18 yields only a small improvement with respect to the reference filter combination (BG18 & RG645), from 19.5% to 16.7%, while the signal level is increased by a factor of 1.5 compared to the double RG645 filter configuration. This is also consistent with the conclusion from the double RG645 filter case, that the variation in the luminescence spectrum of individual dispersed SMP:Sn²⁺ particles plays a more important role in intensity

5.1. EXPERIMENTS APPLYING THE SPECTRAL SEPARATION METHOD

ratio precision than the signal limitation. The poorer performance offered by the double BG18 filter combination can be attributed to a higher temperature sensitivity of SMP:Sn²⁺ particles in the blue region, as can be seen in Fig. 5.1 which shows a sensitive peak at about 400 nm. Furthermore, the blue filter would capture the blue fluorescences from dust particles, receiving more variations that are induced by the polarisation and wavelength dependence of the beamsplitter as mentioned above.

The particle-to-particle standard deviation obtained with the opposite camera configurations is 19.8%, which is almost identical to the value for the beamsplitter configuration for the same filter combination. This would rule out a significant role of anisotropy in the luminescence emission of SMP:Sn²⁺, which would express itself strongly in the opposite camera configuration. A more minor role cannot be ruled out since the absence of beamsplitter also doubled the signal with respect to the beamsplitter. Note that in the opposite camera configuration, the astigmatism in the particle image can be significant. The particle-to-particle standard deviation was also calculated for the general Gaussian form Eq. (4.4) and found to be 28.5% against 19.8% of rotated form Eq. (4.8).

Results obtained for the two types of particles, SMP:Sn²⁺ and ZnO, in the gas and water media are shown in Table 5.2. For the phosphor SMP:Sn²⁺, water dispersion offers a significant reduction in standard deviation compared to seeded gas flows from 19.5% to 12.2%. This may be due to better particle size and shape homogeneity obtained in the liquid phase produced by the ultrasonic dispersion process, while in gas flow particle agglomeration is more likely to occur. Moreover, fewer dust particles are present in the liquid dispersion.

Table 5.2: The particle-to-particle standard deviation in ratios for the two applied phosphors dispersed in gas and water at room temperature

| Phosphors | Gas (95 % CI) | Water (95 % CI) |
|------------------------------------|---------------------|---------------------|
| SMP:Sn ²⁺ (Pellicle BS) | 19.5 (18.9, 20.1) % | 12.2 (9.9, 14.1) % |
| ZnO (Opposite cameras) | 32.1 (31.9, 32.4) % | 41.9 (40.9, 42.9) % |

All results based on ZnO in this thesis were obtained in the opposite camera configuration. In the air, the ratio precision obtained with ZnO is 32.1% which is about 50% larger than that obtained for the tin-doped phosphor (19.8%) at the same configuration. Note that the intensity in the weakest channel for ZnO is about twice as low as that for the tin-doped phosphor, so here both the emission luminescence difference between particles and the signal level may account for the lower precision obtained with ZnO. In liquid dispersion, however, the particle-to-particle standard deviation is much larger, 42%, compared to the seeded gas flow. A possible reason can be that the smaller particle size or de-agglomeration of ZnO particles by the ultrasonic dispersion may lead to larger luminescence anisotropy or color variations.

5.2 Test cases using the dual-frame lifetime method

The results above in this chapter demonstrate that the single particle image fit concept can achieve a high spatial resolution and accurately quantify the temperature field within the thermal boundary layer. Alternatively, a potential direction to simplify this concept is to employ the dual-frame lifetime method rather than the spectral separation approach (both methods as described in Section. 3.1) to measure the individual particle intensity ratio. The dual-frame lifetime method enables measurement with a single camera so as to eliminate the need for disparity correction between the images in the two cameras. Additionally, the single-camera setting avoids errors caused by beamsplitter aberrations or luminescence emission anisotropy for the two-camera setup, which makes this method more robust against experimental uncertainties. Therefore, we conducted some preliminary tests on several phosphor particles using the dual-frame lifetime method to explore the possibility of enhancing the proposed concept.

5.2.1 Thermographic phosphor particles investigated

In test cases, the performance of four distinct particle types was evaluated. The first one is SMP:Sn^{2+} , and its property has been presented in the Section. 5.1.1. Fig. 5.18 presents the changes of SMP:Sn^{2+} in luminescence lifetime concerning temperature, serving as a reproduction of the Fig. 12 in FOND et al. (2019). It can be observed that there is initially a flat evolution in luminescence lifetime followed by a rapid decrease from about 600 K, indicating a greater lifetime sensitivity in higher temperature environments, so this phosphor particle could be well-suited for thermometry in gaseous phase where high temperature processes often occur. It is worth noting that the SMP:Sn^{2+} particles exhibit non-spherical shapes as demonstrated in the SEM measurements carried out by FOND et al. (2019). SMP:Sn^{2+} particles are applied because of their easy accessibility as commercial products.

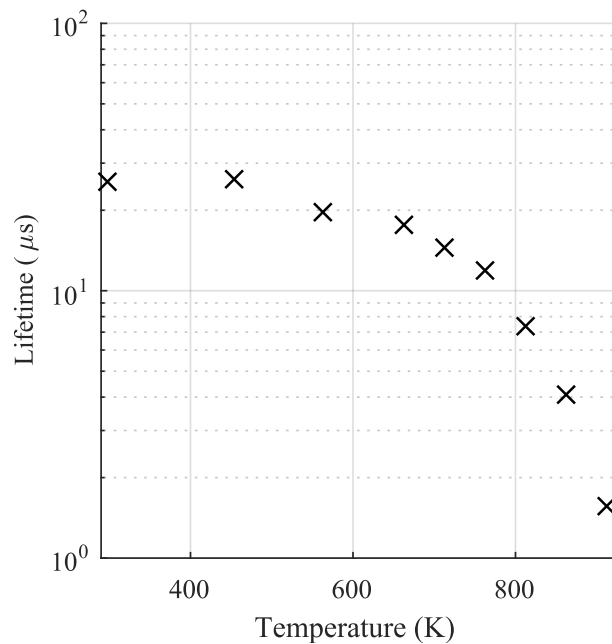


Figure 5.18: Emission decay time ($1/e$) of SMP:Sn^{2+} after 266nm excitation over the 300-900 K range, reproduced from FOND et al. (2019).

5.2. TEST CASES USING THE DUAL-FRAME LIFETIME METHOD

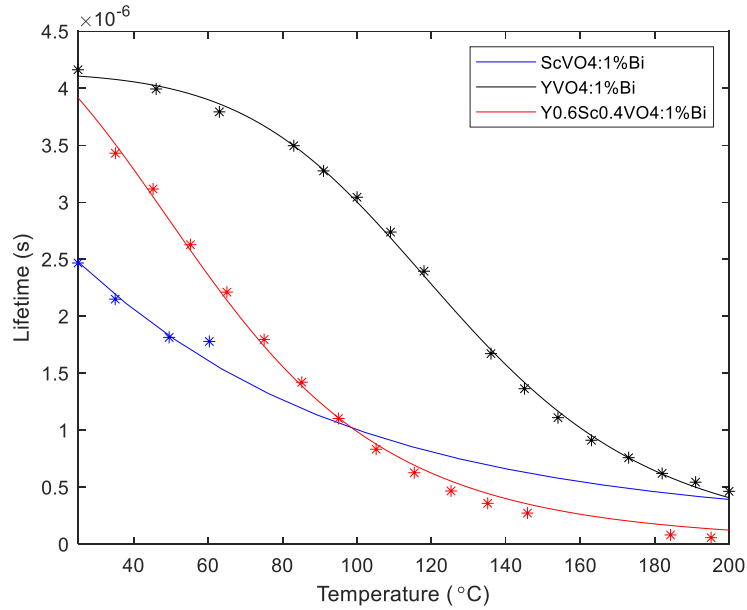


Figure 5.19: Lifetime as a function of temperature for $\text{ScVO}_4 : 1\% \text{Bi}$, $\text{YVO}_4 : 1\% \text{Bi}$ and $\text{Y}_{0.6}\text{Sc}_{0.4}\text{VO}_4 : 1\% \text{Bi}$ excited by 266nm laser. This figure is reproduced from RASHED (2022).

The remaining three particle types employed in test cases, namely $\text{YVO}_4 : 1\% \text{Bi}$, $\text{Y}_{0.6}\text{Sc}_{0.4}\text{VO}_4 : 1\% \text{Bi}$ and $\text{Y}_2\text{O}_3 : 3\% \text{Eu}^{3+}$, were all synthesized in our lab. $\text{YVO}_4 : 1\% \text{Bi}$ and $\text{Y}_{0.6}\text{Sc}_{0.4}\text{VO}_4 : 1\% \text{Bi}$ particles were synthesized using the same method, the classical solid-state method, while the $\text{Y}_2\text{O}_3 : 3\% \text{Eu}^{3+}$ particles were prepared using a flame aerosol synthesis approach (ABRAM et al., 2019). During the synthesis process of $\text{Y}_2\text{O}_3 : 3\% \text{Eu}^{3+}$, aerosol droplets with an approximate diameter of $5 \mu\text{m}$ were produced by an ultrasonic atomizer, and the flame temperature was maintained at about 1500 K. The aerosol synthesis route could offer higher dopant uniformity, and the produced particles are very regular so less likely to show anisotropy or particle-to-particle variations. Consequently, the $\text{Y}_2\text{O}_3 : 3\% \text{Eu}^{3+}$ particles possess a spherical shape as shown in the SEM images (Fig. 7) in ABRAM et al. (2019), whereas the shapes of $\text{YVO}_4 : 1\% \text{Bi}$ and $\text{Y}_{0.6}\text{Sc}_{0.4}\text{VO}_4 : 1\% \text{Bi}$ particles produced by the solid-state method were cuboidal-like, see Fig. 3.13 and Fig. 3.14 in RASHED (2022).

5.2. TEST CASES USING THE DUAL-FRAME LIFETIME METHOD

Fig. 5.19 presents the luminescence lifetimes of $\text{YVO}_4 : 1\% \text{Bi}$ and $\text{Y}_{0.6}\text{Sc}_{0.4}\text{VO}_4 : 1\% \text{Bi}$ as a function of temperature, which is also measured in our lab. Further details regarding their luminescent properties as well as their synthesis method can be found in the work of RASHED (2022). Unlike the $\text{SMP}:\text{Sn}^{2+}$ particles, $\text{YVO}_4 : 1\% \text{Bi}$ and $\text{Y}_{0.6}\text{Sc}_{0.4}\text{VO}_4 : 1\% \text{Bi}$ are sensitive to temperatures below 140°C , resulting in a good adaptability to temperature tracing applications in liquid fluids, especially water. The lifetime data of different doping ratios of Y^{3+} to Sc^{3+} were reported in ELASHRY et al. (2023).

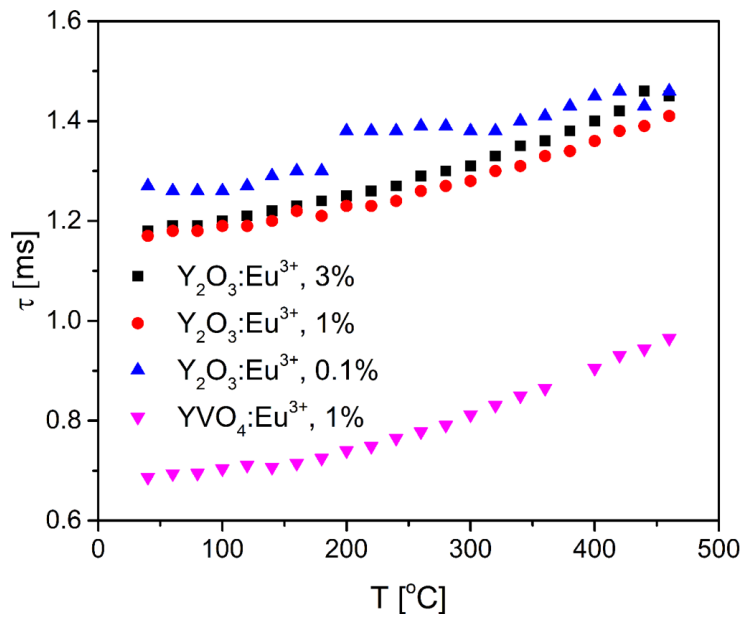


Figure 5.20: Radiative lifetimes of $^5\text{D}_0$ level of Eu^{3+} of Y_2O_3 with 3 %, 1 % and 0.1 %, and YVO_4 doped with 1 % concentration of Eu^{3+} , on the temperature range from 40°C to 460°C . This figure is reproduced from ĆIRIĆ et al. (2020).

The lifetime data of $^5\text{D}_0$ level of Eu^{3+} doped with 3 % Y_2O_3 is illustrated in Fig. 5.20 (reproduced ĆIRIĆ et al. (2020)). As observed, the luminescence time of $\text{Y}_2\text{O}_3 : 3\% \text{Eu}^{3+}$ increases slightly from $1.2 \mu\text{s}$ to $1.45 \mu\text{s}$ as the temperature varying from 40°C to 460°C , representing an average temperature sensitivity of $\sim 0.045\% / ^\circ\text{C}$. Such a low temperature sensitivity signifies substantial uncertainty when applying $\text{Y}_2\text{O}_3 : 3\% \text{Eu}^{3+}$ particle to perform thermometry in a non-uniform temperature field with the dual-

frame lifetime method. The reason for implementing this particle was to study the impact of the spherical shape of particles on the temporally separated intensity ratio. It should be noted that the particles examined in Fig. 5.20 were synthesized with a polymer complex solution method (KRSMANOVIĆ et al., 2011) that differed from the method used here. Consequently, the resulting luminescence lifetimes at specific temperatures can slightly diverge. Given that we did not characterize the luminescence decay property of the sample employed, the value from the literature could be considered as an approximation, while its lifetime at room temperature would also be estimated in the later experiment for optimizing camera timing.

5.2.2 Experimental setup

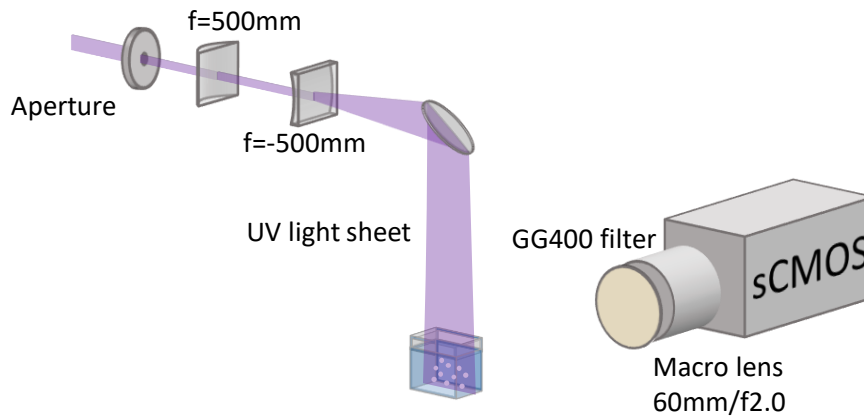


Figure 5.21: Optical setup to acquire temporal separation intensity ratios for high-resolution particle imaging in liquid dispersion.

Fig. 5.21 shows the optical setup for the tests of implementing the dual-frame lifetime method to improve the high spatial resolution temperature measurement. This setup is highly similar to those used to access the spectral separation intensity ratios in Section. 5.1, with the exception of the camera operating in double-frame mode to enable temporal separation dual-frame determination. Another difference was the use of an optical filter GG400 (from SHOTT) instead of the filters matching the peak wavelengths of the phosphor emission spectrum. The filter was used to prevent

interference signals from the stray light or reflection of 266 nm laser. Here, it should be noted that for some phosphors such as the $\text{Y}_2\text{O}_3 : 3\% \text{Eu}^{3+}$ particles, emission of several transitions would be acquired by the camera. During this experiment, only isothermal tests at room temperature were conducted, and thus the intensity ratio distribution of single phosphor particles at room temperature were explored. The temperature dependency of intensity ratios derived from temporarily separated images will be demonstrated and determined in further works.

Of the four particle types applied, tin-doped phosphor $\text{SMP}:\text{Sn}^{2+}$ was also used in Section. 5.1.2.1 to resolve the temperature in a liquid dispersion, and in Section. 5.1.3.1 to demonstrate the ability to reject the low frequency interference in a seeded gas. The lifetime of $\text{SMP}:\text{Sn}^{2+}$ is about $26\mu\text{s}$ as mentioned in Section. 5.1.1, we thus set the first frame exposure time t_1 to $19\mu\text{s}$, resulting in a normalized time ($\tau_n = t_1/\tau$) of 0.72, within the optimal range of 0.5-4 as recommended by ABRAM et al. (2020). The luminescence of $\text{YVO}_4 : 1\% \text{Bi}$ and $\text{Y}_{0.6}\text{Sc}_{0.4}\text{VO}_4 : 1\% \text{Bi}$ exhibit similar lifetimes of approximately $4\mu\text{s}$ at room temperature, see Fig. 5.19, so that the first frame exposure time t_1 for imaging them was chosen to be $2.4\mu\text{s}$, leading to a normalized time τ_n of 0.6. Since the luminescence decay time of the phosphor $\text{Y}_2\text{O}_3 : 3\% \text{Eu}^{3+}$ at room temperature had not been measured on this specific sample, it could be estimated by gradually delaying the start of the first frame exposure with respect to the laser pulse until the camera cannot acquire any luminescence signals. This process does not need to be highly precise, for example using a delaying step size of every 1 microsecond, and the total decay of $\text{Y}_2\text{O}_3 : 3\% \text{Eu}^{3+}$ is found to be within $4\sim 6\mu\text{s}$. Therefore, the lifetime τ of $\text{Y}_2\text{O}_3 : 3\% \text{Eu}^{3+}$ can be calculated to be about $1\mu\text{s}$, in agreement with the study of ĆIRIĆ et al. (2020). The first frame exposure time t_1 in the experiment is consequently set to be $0.7\mu\text{s}$, giving a normalized time τ_n of 0.7. In the images acquired using this camera timing, the luminescence intensity is almost at the same level between the two temporarily separated frames, which verifies the total decay time approximation according to the integral analysis of the exponential decay function.

5.2.3 Results

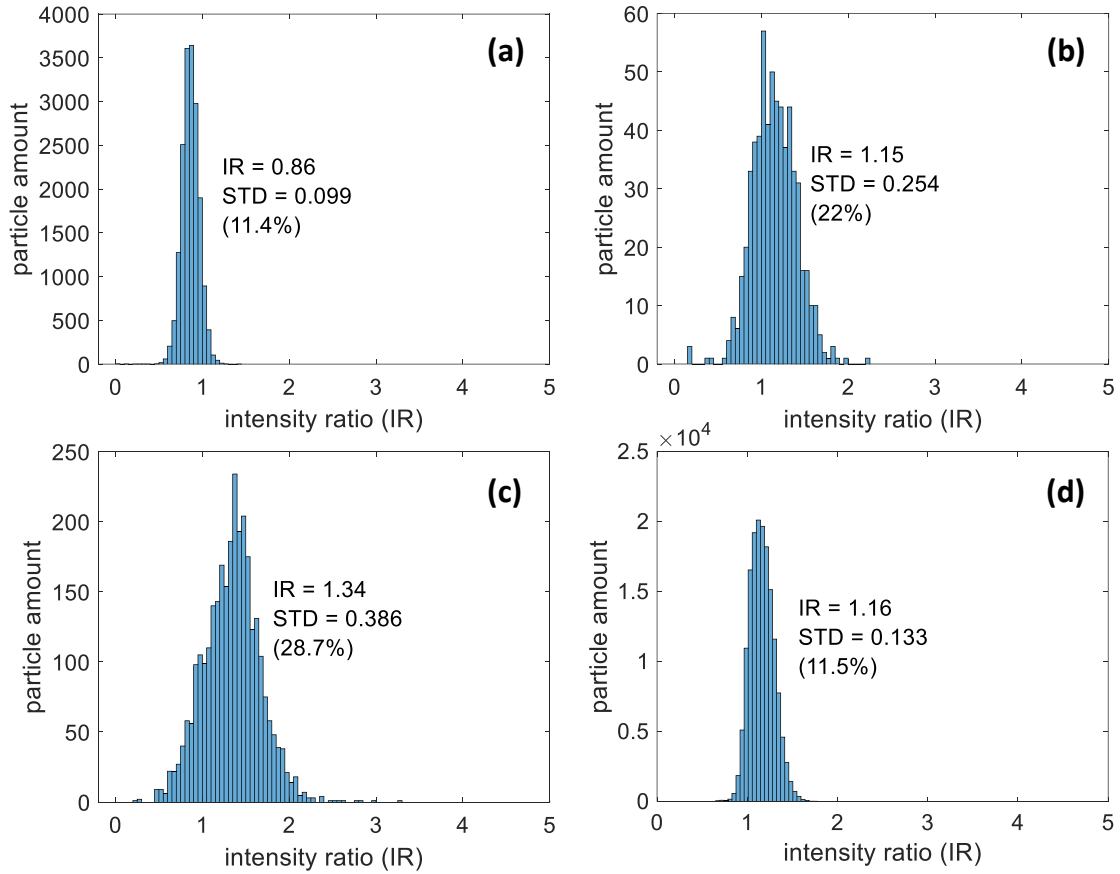


Figure 5.22: Intensity ratios distribution of four tested phosphor particles obtained from the dual-frame lifetime method at room temperature. (a) tin-doped phosphor particles, $\text{SMP}:\text{Sn}^{2+}$; (b) $\text{YVO}_4 :1\%\text{Bi}$ particles; (c) $\text{Y}_{0.6}\text{Sc}_{0.4}\text{VO}_4 :1\%\text{Bi}$ particles; (d) $\text{Y}_2\text{O}_3:\text{Eu}^{3+}$ particles.

For each of the four phosphors, we estimated the intensity ratios between the temporarily separated dual-frame for at least 500 measurements (single particles) over an accumulated measured field of $14 \times 17 \text{ mm}$ under isothermal conditions (room temperature). Their ratio distributions are presented in Fig. 5.22, which results were obtained with an image fitting R-square above 0.95 as explained in Section. 4.1.3. Notably, as a white field correction was conducted, these results could contain a potential deviation caused by the image detector pixel-to-pixel sensitivity and distortions in

the optical. In the figure, one can observe that $\text{YVO}_4 : 1\% \text{Bi}$ and $\text{Y}_{0.6}\text{Sc}_{0.4}\text{VO}_4 : 1\% \text{Bi}$ have similar ratio variations exceeding 20%, while $\text{SMP}:\text{Sn}^{2+}$ and $\text{Y}_2\text{O}_3 : 3\% \text{Eu}^{3+}$ show a much smaller variation of about 11%, indicating significantly less fluctuations in their emission decay time. For $\text{SMP}:\text{Sn}^{2+}$, this discrepancy can be attributed to the fact that the lifetime of $\text{SMP}:\text{Sn}^{2+}$ is more insensitivity at room temperature compared to $\text{YVO}_4 : 1\% \text{Bi}$ and $\text{Y}_{0.6}\text{Sc}_{0.4}\text{VO}_4 : 1\% \text{Bi}$, as shown in Fig. 5.18 and Fig. 5.19. In addition, the phosphorescence properties of $\text{SMP}:\text{Sn}^{2+}$ are less susceptible to variations in the fluence of laser light sheet (FOND et al., 2019). Furthermore, given an identical random error in the detected lifetime induced by the same imaging setup, particles with longer lifetimes, such as $\text{SMP}:\text{Sn}^{2+}$ particles, are preferable due to their reduced susceptibility to such an error. However, the poor temperature sensitivity of $\text{SMP}:\text{Sn}^{2+}$ within low temperature range limits its application in the environments of, for example water dispersion, despite its remarkable performance in terms of intensity ratio variation.

Differences in particle size and shape can also alter the phosphor emission decay time (SHAN et al., 2010; VALIEV et al., 2018; BOIKO et al., 2021) causing larger ratio bias here. The $\text{Y}_2\text{O}_3 : 3\% \text{Eu}^{3+}$ particle is therefore tested to investigate the potential of its spherical shape to yield reduced intensity ratio variations. However, $\text{Y}_2\text{O}_3 : 3\% \text{Eu}^{3+}$ exhibits a similar ratio precision to that of the $\text{SMP}:\text{Sn}^{2+}$, characterized by a non-spherical shape. This rules out the dependence of the intensity ratio on the spherical shape of particles. The remarkable precision of $\text{Y}_2\text{O}_3 : 3\% \text{Eu}^{3+}$ particle can be also attributed to the fact that its lifetime is extremely insensitive to the temperature (see Fig. 5.20), which inversely limits its application. The other causes of such a small intensity variation remain unexplained because the luminescence properties of this sample, for example the dependence on laser energy fluence, have yet to be characterized.

6

Multi-point temperature reconstruction in opaque packed beds

This chapter covers demonstration experiments aimed at measuring temperatures at discrete points inside an opaque, regular packed bed that serves as a highly scattering media. In this context, spheres strategically situated at the measured locations were coated with luminescent phosphor powder and excited by penetrating laser light. The decay time of the emitted luminescence depends on the sphere temperature, which forms the basis of this measurement technique. As a verification, the measured temperatures were validated against thermocouple readings.

The preliminary experiments were conducted under both isothermal and non-isothermal conditions with only one luminescent sphere loading in the packed bed. These experiments served two purposes: first, they established and verified the method, and second, they facilitated the derivation of an in-situ temperature-ratio calibration curve, ensuring accurate temperature evaluation. The experiments were subsequently extended to the case of three luminescent spheres under non-isothermal conditions. Those three spheres were present simultaneously in the packed bed, where the measured luminescence is a complex superposition of the contribution by each sphere. By

isolating the individual luminescence contributions using the proposed linear regression method, simultaneous temperature measurement at three discrete points within the bed was realized.

Nonetheless, the purely experimental way is limited to the packed bed with a regular structure, since it requires disassembling and reassembling the packed bed multiple times but keeping the structure identical. In practice, actual packed beds commonly feature a randomized structure, making it unfeasible to reconstruct the packed bed with precisely the same structure repeatedly. To overcome this limitation, this chapter introduces the combination of the proposed concept with ray tracing simulations, providing an option that eliminates the necessity for repetitive bed reassembly. The work in this chapter is partly derived from the publication XUAN et al. (2024).

6.1 Thermographic phosphor particles selection

In the experiment of temperature reconstruction in the opaqua packed bed, YAG:Cr³⁺ was used as thermographic phosphor because its luminescence decay time was sensitive over the 20 – 300 °C (SHEN und BRAY, 1997) temperature range that was aimed at in this work. The temperature dependency of YAG:Cr³⁺ luminescence lifetime is shown in the Fig. 3.2(a) in Section. 3.1.2, which allows us to determine the lifetime of YAG:Cr³⁺ at room temperature to be about 4 ms.

6.2 Design of the packed bed

In order to perform the experiments with a packing geometry in which each sphere position is unambiguously defined and reproducible, we conducted the experiments with a regular face-centered cubic (FCC) packing of identical spheres. The packing has 107 spheres that are arranged in three vertical layers of 5 × 5 spheres interleaved with two layers of 4 × 4 spheres, as illustrated in Fig. 6.1(a). To uniquely identify each

6.2. DESIGN OF THE PACKED BED

sphere, an index system was established in which the centre sphere was defined as the origin and was labeled $(0,0,0)$ (see Fig. 6.1(b)). In this notation, the z index specifies the vertical layer while the x and y indices indicates the coordinates of the spheres inside each layer. In the 5×5 layers, the spheres have integer x and y coordinates, such as $(1,0,0)$ for the red-coloured sphere in Fig. 6.1 (c). Within the 4×4 layers, which are at uneven z coordinates, the spheres are shifted by a half sphere distance with respect to the 5×5 layers. Consequently, their x and y indices are half integers, e.g. $(-0.5,-0.5,1)$ for the red-coloured sphere in Fig. 6.1 (d).

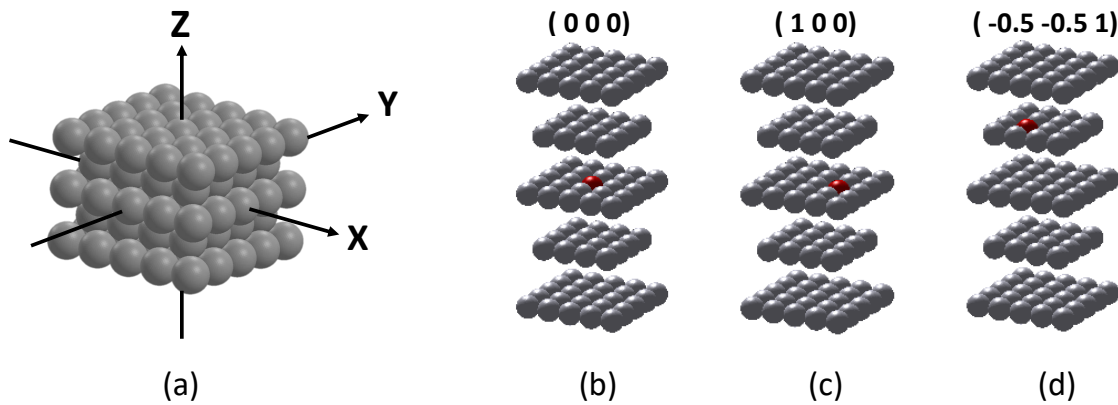


Figure 6.1: (a) Regular packing coordination system; (b), (c) and (d) are the examples of location indices of the red-colored spheres. This figure is reproduced from XUAN et al. (2024).

The present work utilized 6 mm aluminum spheres as packing material due to the high thermal conductivity of aluminum, which minimises the temperature variations inside each sphere. Some spheres were coated with micron-size thermographic phosphor particles to enable local temperature measurements. YAG:Cr^{3+} was used as thermographic phosphor in our experiments because its luminescence decay time was sensitive over the $20 - 300$ °C temperature range that was aimed at in this study, cf. SHEN und BRAY (1997). The phosphor particles were mixed with a binder (HPC, Zyp coating) in a ratio of 1 g of phosphor per 24 mL of binder, and applied on the surface using an airbrush. In order to obtain an uniform coating on the spheres, we designed a custom procedure where the spheres were placed in a tray fixed to the

6.3. OPTICAL SETUP

translation stage of a 3D printer frame. The mixture of phosphor water dispersion and binder was sprayed through an airbrush nozzle replacing the 3D printer injection head. About 500 spraying passes was necessary to reach a coating thickness of 15 μm , estimated by measuring the diameters of tens of spheres before and after coating with a thickness gauge. Between spraying passes, the tray was subjected to a sudden translation causing the spheres to roll. The purpose of this was to randomize the sphere orientation during each spraying pass to maximize the uniformity of the coating. Due to the long drying time of this water-based coating between each spraying pass, the whole coating process took several hours. In addition, it yielded a limited number of spheres with uniform coating, about 5 spheres were hand picked out of initial 100 spheres placed on the tray. The non-luminescent spheres should also be coated with a similar coating but without phosphor particles to obtain a similarly diffuse reflectivity of their surface. Since over hundred non-luminescent spheres have to be coated, we used instead a commercial plastic primer in a spray can, which can coat such large number of spheres in only several minutes. On the other hand, in the future, we will consider spheres made of oxide or ceramic material, for example to study calcination processes. Those will have similar reflective properties than the phosphor coating, and coating the non-luminescent spheres will not be necessary.

6.3 Optical setup

Fig. 6.2(a) is a schematic of the optical setup of the experiment. The packing was held in a fused silica cuvette (cuvettes.ch UQ-752) which width and depth were chosen to be five sphere diameters, in order to fix the bed position. Additionally, the cuvette was selected aimed for a high transmittance for wavelengths 190 - 2500 nm. For excitation of the phosphor luminescence, the 12 mm diameter laser beam of a pulsed frequency doubled Nd:YAG at 532 nm was directed normally through the center of the cuvette lateral face; and to compensate for the loss through multiple reflections inside the

6.3. OPTICAL SETUP

bed, a laser energy of 90 mJ/pulse was used. The excitation light penetrates within the bed and excites, after multiple diffuse reflections, one or several phosphor-coated spheres. Upon being pulsed-excited, the packing spheres emit luminescence that gradually decays over time after the end of the pulse. This luminescence emission exits the packed bed also after multiple scattering events. It is then imaged by a sCMOS camera placed at 90 degrees with respect to the incident beam and equipped with a 50 mm f/1.4 Nikon lens as well as a 645 nm long-pass filter (SCHOTT RG645) to remove the excitation light. The camera was focused on the front surface of the packing to maximise the sharpness of the image. Here the delay time, t_0 , between the laser pulse and the camera's first exposure frame was set to 5 μs , which had negligible impact on signal collection, considering the millisecond-order lifetime for YAG:Cr^{3+} . The first frame exposure time (t_1) was set to 1.5 ms, resulting in a ratio of first frame delay to lifetime (τ) from 0.75 to 2.14 in the range of temperatures during the measurement, representing an optimal temperature precision as mentioned in Section. 3.1.2.

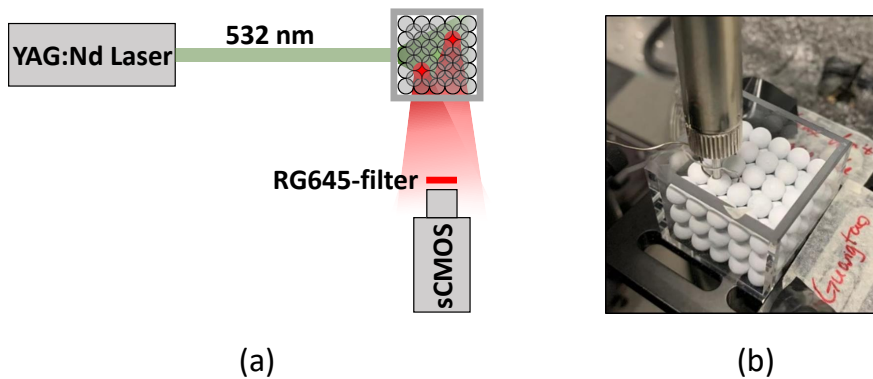


Figure 6.2: (a) Setup for optical thermometry and. (b) Photograph of packing with heating element and thermocouple. This figure is reproduced from XUAN et al. (2024).

To facilitate the heat transfer investigation in the packing, a local heating unit was added to induce a temperature perturbation and to observe the resulting temperature distribution. Specifically, as presented in Fig. 6.2(c), one of the non-luminescent spheres in the top layer was heated by contact with the heating tip of a soldering station. To ensure good contact between the tip and the sphere, a 2.2 mm diameter

6.4. CALIBRATION AND ASSESSMENT OF POSITION INDEPENDENCE OF THE PHOSPHOR THERMOMETRY METHOD

and 3 mm deep hole was drilled into the sphere. An additional 0.55 mm diameter hole was drilled to insert a 0.5 mm diameter type K thermocouple in order to monitor its temperature. The temperature histories of one of the phosphor-coated spheres was also measured using an embedded thermocouple.

Since dual-frame lifetime method exploits the temperature dependence of the decay time, but not that of the emission spectrum, it does not suffer from the spectral distortions caused by the multiple reflection events inside the packing. These reflections may delay and spread the decay waveform through an increase and variation of time flight within the packing, but this effect is expected to be in the sub-nanosecond range for the centimeter-scale bed, while the decay time of YAG:Cr³⁺ is in the millisecond-order range. Therefore, the temporal distortion is considered negligible even for larger packings.

6.4 Calibration and assessment of position independence of the phosphor thermometry method

Prior to measuring temperature in an unknown temperature field, the ratio response to temperature was calibrated. One luminescent sphere with an embedded thermocouple was placed at one out of the four centremost positions in the $z = 1$ layer, (-0.5 -0.5 1), where it experienced a range of temperature, from 27 to 150 °C, as a result of transient heating from the top sphere. During the heating, intensity ratios were derived for different temperatures using local time average over a time series of 19 single pulse measurements (within 2s), during which the temperature variation was less than 1 °C. Those ratios form the curve as shown in Fig. 6.3. A high temperature sensitivity of about 1 %/°C could be derived from the fitted curve, which number is in agreement with the measured decay sensitivity of YAG:Cr³⁺ powder LOPEZ-BONILLA et al. (2023) and the timing dependent sensitivity factor ABRAM et al. (2020). This indicates that,

6.4. CALIBRATION AND ASSESSMENT OF POSITION INDEPENDENCE OF THE PHOSPHOR THERMOMETRY METHOD

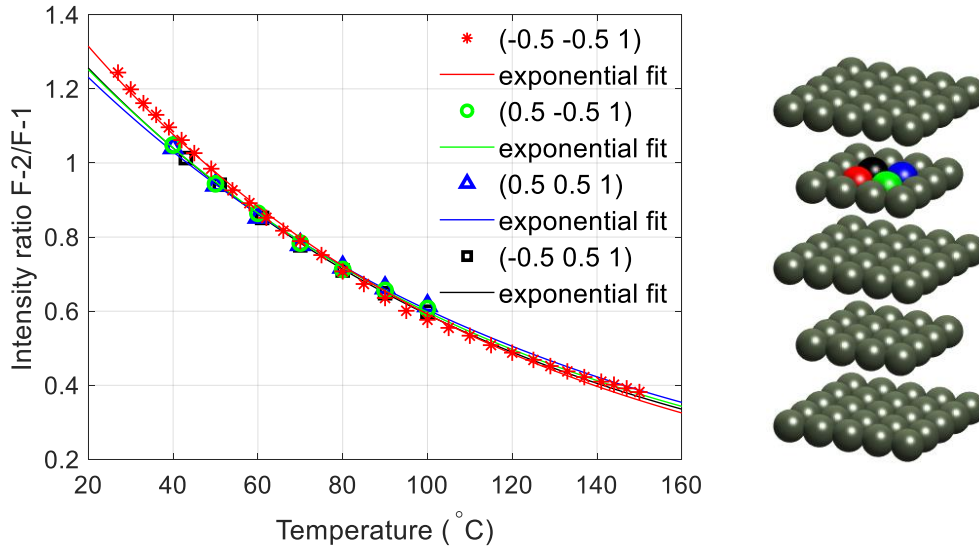


Figure 6.3: The intensity ratios measured at four locations of the luminescent spheres inside the packing, over the 27 – 150 $^{\circ}\text{C}$ temperature range. Exponential fit curves are used for ratio to temperature conversion and to guide the eye.

compared to direct visualization, the perceived luminescence response is unaffected by the indirect measurement of the luminescence from the sphere inside the bed. This in-situ calibration allows to maintain the incident fluence experienced by the sphere in a similar range as during the actual experiment. Measurements were repeated when the sphere was placed at the other three positions within the same $z = 1$ layer, as the results are also shown in Fig. 6.3. The four calibration curves in the figure are of good agreement, with deviation slightly increasing at low temperature and a relative difference of 5.7 % at 27 $^{\circ}\text{C}$. The results demonstrate the repeatability of the system and a first assessment of the independence of the sphere temperature response on its position.

It is difficult to place a sphere with an embedded thermocouple tip in the lower layers as there must be a clear path for the thermocouple lead, especially for $z = -1$ and -2 layers where we were not able to reach at all during the measurement. To further extend the study of position independence to a broader range of positions inside the bed, an experiment was performed with a single luminescent sphere placed at 13

6.4. CALIBRATION AND ASSESSMENT OF POSITION INDEPENDENCE OF THE PHOSPHOR THERMOMETRY METHOD

different internal locations of the packed bed under uniform room temperature, 25 °C condition. At each location, an ensemble of 19 image pairs was taken for dual-frame 2D lifetime determination, as the results presented in Fig. 6.4. The figure shows a small variation around 25 °C, with a mean deviation of 1.7 °C. A more minor variation could be observed among those 4×4 layer, especially for the $z = 1$ layer where the deviation of mean temperature is below 0.5 °C. More considerable measurement variation occurred at the $z = 0$ layer. In particular, the maximum temperature bias of 4.9 °C was at the location (0 1 0), which also presented a larger shot-to-shot fluctuation as expected, because this location had the lowest signal level since the sphere located at it was the furthest away from the beam optical axis and the detector (camera). Despite this, the good agreement between average temperature demonstrated the independence of the temperature measurement from the luminescent sphere locations, showing the robustness of the temporal temperature readout implemented here.

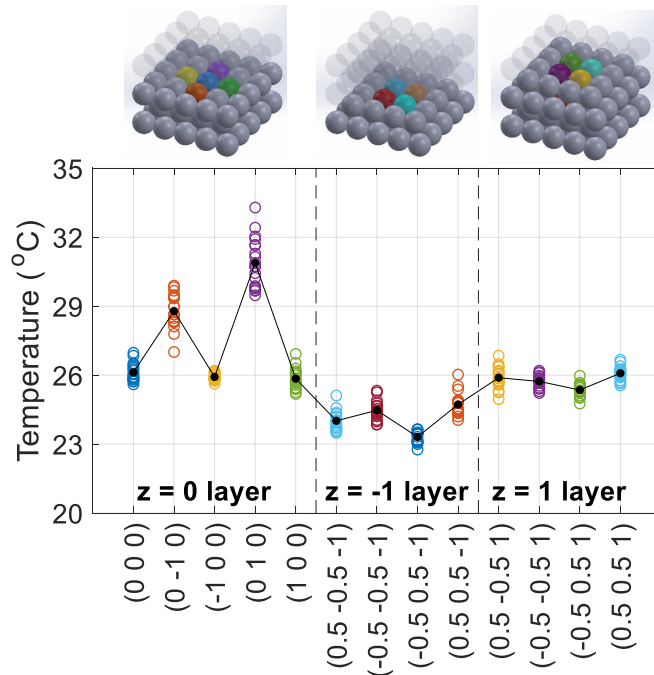


Figure 6.4: Repeated temperature measurements for single luminescent sphere placed at 13 different locations separately in the packing under isothermal condition (25 °C). This figure is reproduced from XUAN et al. (2024).

6.5 Demonstration of three spheres instantaneous thermometry

6.5.1 Experimental results

For demonstrating multi-point temperature detection, we tested the case of three luminescent spheres, S1 (-0.5 -0.5 1), S2 (0 0 0) and S3 (-0.5 -0.5 -1). Their locations are shown on the right of Fig. 6.5. Among these three measured spheres, S2 was embedded with a thermocouple in order to validate the temperature measurements, while S1 and S3 would only be inferred by their temporarily separated intensity ratio.

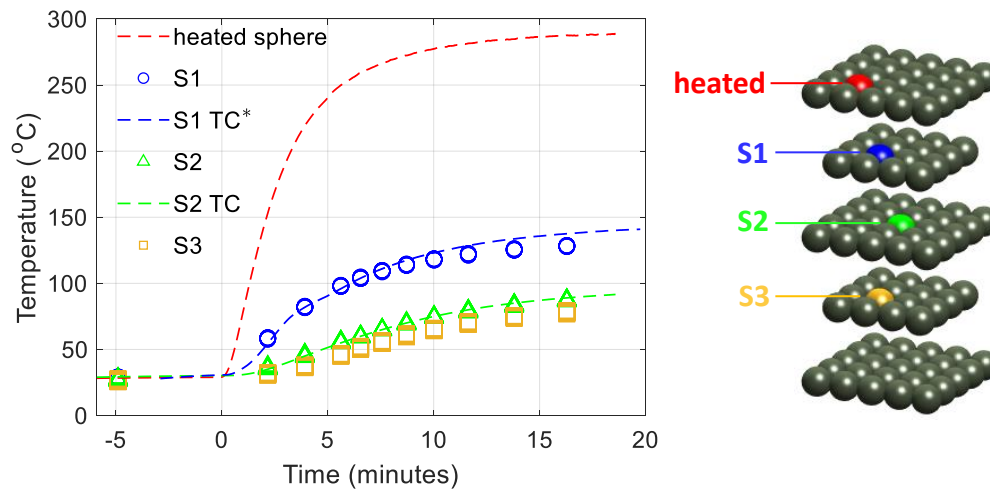


Figure 6.5: Temperature-time traces using linear regression fit to isolate the multiple spheres signals into individual contributions based on measured $S^{(j)}(x, y)$ templates. The temperature of all the spheres except S3 were measured by thermocouple (TC) simultaneously, but the thermocouple readings for S1 is from a separate measurement, denoted by the asterisk exponent. This figure is reproduced from XUAN et al. (2024).

The experiment was started under isothermal room temperature condition. At $t = 0$ min, heating was imposed from one of the top spheres, which temperature was measured by a thermocouple to provide the heated source temperature. Also, this heated sphere temperature will be used as the input data in heat transfer simulation

6.5. DEMONSTRATION OF THREE SPHERES INSTANTANEOUS THERMOMETRY

done by a collaborating researcher for data assimilation, so as to access the thermal properties inside the packed bed. Results under transient heating are plotted on the left of Fig. 6.5. Note that here linear regression fitting for signals separation was based on the measured templates of 2D intensity distribution function $S^{(j)}(x, y)$, when single phosphor coated spheres are placed in the bed at the correspondingly respective positions. As shown, S1 is in direct contact with the heated sphere so it has the lowest temperature difference to the heated sphere. The heat is then transported by contact from S1 to S2 and finally the S3. It is therefore expected that the temperature of the S2 should be theoretically between S1 and S3, as observed in the figure. In addition, the temperature obtained by S2 is in good agreement with its thermocouple readings, with a mean temperature deviation of 0.8 °C, and a maximum deviation below 2 °C at 88 °C. This demonstrates that the contribution from S2 was successfully isolated from those of S1 and S3, which are at different temperatures.

At this stage, only one phosphor-coated sphere with a thermocouple was available. In order to offer additional validations using results from separate measurements with the thermocouple-connected sphere at a different location, we evaluated the repeatability of the experiment. For this, the packed bed was reassembled three times in a different sequence of spheres, and thermocouple measurements were taken each time for the sphere at S2. The maximum deviation between temperature histories was found to be 4 °C.

Since the experiment was found to be repeatable, the packed bed was reassembled and the sphere with the embedded thermocouple was placed this time at S1. The measured profile was added to Fig. 6.5. The resulting mean temperature difference for S1 is 3.8 °C, and the maximum bias is 9 °C occurring at 128 °C. The sphere with a thermocouple cannot be placed at the location of S3, as there was no passage for the thermocouple leads at this position. This fact is one of the limitations of thermocouple application. These results illustrated that the separation of signals can provide accurate independent measurements.

Here the temperature of the heated sphere is limited by the heating source (soldering station), leading to the internal temperature of the packed bed within a modest temperature range, approximately below 200 °C, over which the selected phosphor YAG:Cr³⁺ has high temperature sensitivity, as shown in Fig. 3.2(a). Many phosphor materials are available and some were found to be suitable for measurements at temperature above 1400 °C such as YAG:Tm,Li in NILSSON et al. (2023). At high temperature (above 1000 °C), we anticipate however that the contribution of blackbody radiation could be significant. Therefore blue emitting phosphors with short decay time should be considered so that the contribution of blackbody radiation can be minimized by spectral and temporal filtering.

6.5.2 Analysis of combination with ray tracing simulations

Separating the multiple spheres signals relies on the individual spatial distribution functions $S^{(j)}(x, y)$. Determining the $S^{(j)}(x, y)$ experimentally is, however, often impractical since it amounts to dis- and re-assembling the experimental setup. We therefore employ an optical simulation based on a computer model of the experimental setup to obtain the $S^{(j)}(x, y)$.

The simulations are done by cooperating researchers, M. Ebert and C. Lessig, using Monte Carlo ray tracing that computes both optical paths and the intensity that is transported along these paths. Given the simple geometry of the experimental setup, a computer model of it was generated by hand assuming an ideal packing of the analytic spheres. Since the spheres in the experiment were coated, an ideal diffuse scattering with reflectance factor of 0.75 was used. No laser light propagation or luminescence were simulated but the phosphor-coated spheres were directly modeled as radiation sources. This simplification, however, will introduce inaccuracies to the predicted temperature because in reality the luminescence spatial distribution is dependent on the excitation light distribution. In the simulation, a pinhole camera model was

employed with parameters derived from those provided by the LaVision Davis.10 software calibration used in the experiments.

6.5.2.1 Comparison of measured and simulated intensity distributions

An example for a simulated image in comparison to the measured one can be found in Fig. 6.6(a). A good agreement between the images can be observed with a clear correspondence between the particle interstices (triangle-shaped regions). Since a pinhole camera model is employed, the simulated image appears overly sharp.

A slight asymmetry can be observed in the measured image due to the laser penetrating from the left and therefore leading to a higher excitation irradiance on the left side of the phosphor-coated sphere. This is not present in the simulation since there the phosphor-coated spheres are directly modeled as radiation sources for simplification. The differences between measurement and simulation can be assessed in more detail in the cross sections also shown in Fig. 6.6(b). Again, the simulation provides a symmetrical profile about the sphere position, while the measurement show higher signals on the left side than on the right side for the reason mentioned above. The vertical profile is also symmetrical about the sphere position in the simulated image but not on the measured image, due to the Gaussian shape of the excitation beam which leads to a non uniform irradiance on the phosphor coated sphere.

6.5.2.2 Application in the demonstration case

The ray tracing simulation allows one to obtain the spatial intensity distribution functions $S^{(j)}(x, y)$, without needing to take measurement with the individual spheres at the exact same position as in the multiple spheres measurements, which are only possible in regular beds where all sphere position are fixed. In complex setups, with irregularly packed spheres and for all non-spherical particles, such experimental determination is infeasible.

6.5. DEMONSTRATION OF THREE SPHERES INSTANTANEOUS THERMOMETRY

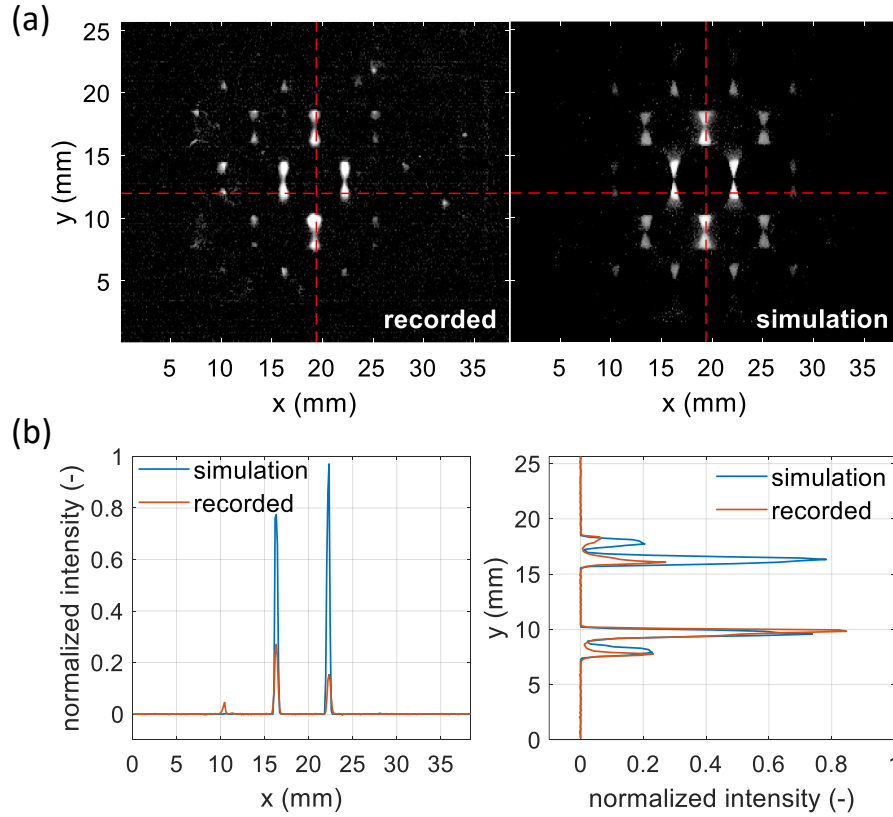


Figure 6.6: (a) Comparison between recorded and simulated image of luminescent light formed on the camera when a luminescent sphere is located at the center of the packing. (b) Normalized intensity plot of the data region indicated by the red dash line in (a). The intensities from the two approaches are normalized to their respective maximum intensities. This figure is reproduced from XUAN et al. (2024).

To validate the use of simulated $S^{(j)}(x, y)$, we performed the temperature estimation for the three luminescent spheres case described in Section. 6.5.1 using simulated $S^{(j)}(x, y)$. The resulting temperatures are plotted in Fig. 6.7. As can be seen there, the temperatures obtained with the proposed method and with the thermocouples are in good agreement for both spheres S1 and S2. Also, the derived temperatures are similar to the reconstructed values inferred from measured $S^{(j)}(x, y)$ (see Fig. 6.5). S1 has a mean temperature deviation from thermocouple measurements of 4.6 °C and a maximum deviation of 10 °C at 106 °C. For S2, the mean temperature deviation is 0.8 °C, while the maximum deviation is less than 1.5 °C at 71 °C. For the third sphere

S3, there is no thermocouple reference measurement available. However, compared to the results obtained with the measured $S^{(j)}(x, y)$ in Fig. 6.5, the difference is larger, between 7 and 12 °C. Given the position of the heated sphere, the lower values provided by the measured luminescence images appear more plausible. This would indicate that although the results using the simulated profiles are promising, the differences between simulated and measured luminescence images are still a limited factor for accurate signal separation. The contribution of the various spheres may be under or over-estimated, which translates here into a 10 °C error representing approximately 10% of the temperature difference of about 100 °C. The effect of a fixed relative signal over-estimation on the temperature error is a complex function of temperature, since the temperature dependent variation of the intensity in the first and the second frame depends on the choice of camera gating, thermal quenching of the phosphor emission intensity and the temperature sensitivity of the decay time of the chosen phosphor. To design future experiments with higher temperature difference, this effect could be modeled based on the temperature dependent characteristics of the chosen phosphor. However, it is clear that the integration of the excitation light propagation is necessary to obtain more accurate evaluations.

6.5.2.3 Limits of reconstruction and its a priori estimation

The condition number κ is a scalar value that quantifies the sensitivity of a function's output to changes in its inputs. In general, the larger the condition number κ , the more sensitive the function is to small changes in its inputs, indicating that small errors in the inputs can lead to large deviations in results. Therefore, the condition number of a linear regression problem indicates the amplification of random errors by the least squares fit. To obtain κ , one can perform the Singular Value Decomposition (SVD) to the input matrix of a linear regression problem. The condition number κ is then given by the ratio of the maximal singular value to the minimal value. For the signal separation process discussed in this thesis, the condition number hence provides a

6.5. DEMONSTRATION OF THREE SPHERES INSTANTANEOUS THERMOMETRY

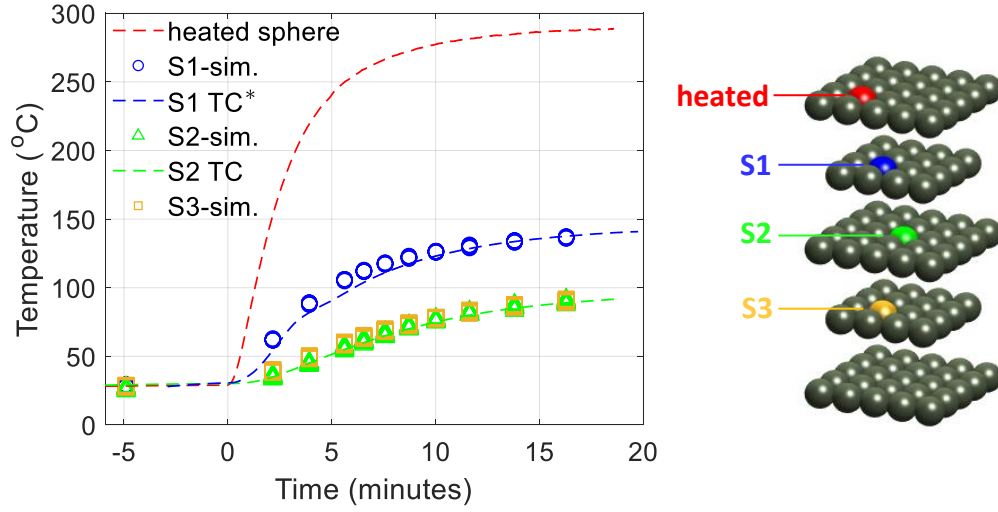


Figure 6.7: Temperature histories measurement for the three luminescent spheres case described in Section. 6.5.1, but using simulated spatial intensity distribution function $S^{(j)}(x, y)$ for signal separation. This figure is reproduced from XUAN et al. (2024).

means to predict the reconstruction quality based on the individual spatial intensity distributions and the configuration of the sphere locations, yielding a priori estimation for the amplification of measurement uncertainties and errors.

In principle, a condition number κ close to unity (one) leads to no or little amplification and is thereby the optimal case. For example, if one sphere case has a precision of 1 K, and we consider a multiple sphere configuration with a condition number of 2, we could anticipate that the temperature precision in this case will degrade to approximately 2 K.

The ray tracing simulation enables us to easily determine the spatial intensity distribution functions $S^{(j)}(x, y)$ for all sphere locations in a packed bed and hence to compute the condition numbers for arbitrary multiple spheres arrangements. This provides the possibility to predict the difficulty of a temperature measurement in a specific configuration before performing an experiment.

Numerical values of the condition number for the three-sphere measured data and simulated data in Section. 6.5.1 and Section. 6.5.2.2 are shown in Table. 6.1. In addition,

6.5. DEMONSTRATION OF THREE SPHERES INSTANTANEOUS THERMOMETRY

Table 6.1: Condition number and fitting errors of the linear regression fit for measured and simulated spatial intensity distribution functions $S^{(j)}(x, y)$, for the sphere arrangement shown in Section. 6.5.1. In the table, F_1 and F_2 indicated the results of the two frames used for the temperature determination.

| $S^{(j)}(x, y)$ obtained | Experiment | Ray tracing simulation |
|--------------------------------------|-------------------|-------------------------------|
| Condition number κ | 1.75 | 2.25 |
| RMSE (F_1 / F_2) $\times 10^3$ | 3.31 / 2.24 | 6.02 / 3.92 |
| RSS (F_1 / F_2) $\times 10^{10}$ | 0.41 / 0.20 | 1.00 / 0.45 |

the table also includes the statistics analysis of root mean square error (RMSE) and residual sum of square (RSS) from the linear regression fitting for the signals separation process. These statistics results were presented for the two frames, denoted by F_1 and F_2 in the table, while the condition number has only one for each case since the $S^{(j)}(x, y)$ template stays the same for both frames. The condition number of the experiment is closer to one than that of the simulation case, which agrees with a more accurate results from the experiment. For the simulation, additional errors arise through the inaccuracies in the alignment between the experimental setup and its computer model, e.g. non-ideal sphere placement or an imperfect camera model in the computer.

Further results of the condition numbers as a function of the sphere arrangement and the corresponding corollaries on the limitation in the number of detectable spheres are provided in XUAN et al. (2024).

7

Conclusions and Future Works

This thesis introduced two innovative concepts based on the analysis of luminescence images of discrete particles. The first one is capable of achieving temperature measurements with exceptional spatial resolution in luminescent particle dispersion. The second concept offers a method for determining temperatures within an opaque packed bed, a particularly challenging context due to its pronounced scattering characteristics. Both concepts were intended to isolate the luminescence of individual discrete particles and thus exploit the thermal dynamics of individual particles. This final chapter serves to summarize the results of all the research work, and presents prospective applications as well as potential directions for further developing this technique.

7.1 Imaging of individual dispersed particle for high spatial resolution thermometry in fluids

7.1.1 Summary of the works

The proposed concept utilizes the discrete nature of the luminescence emission from individual particles, which can be isolated and fitted for temperature measurements to achieve an in-plan high spatial resolution. This was first demonstrated by imaging the signals from tin-doped phosphor SMP:Sn²⁺ in a liquid dispersion. The fit is based on a rotated 2D Gaussian function that exhibits a more robust performance in interpreting particle images with aberration. With this technique, the positioning precision of the particle is better than 0.2 pixels, allowing for an in-plane spatial resolution as high as a few microns for thermometry.

In contrast with the window-based intensity ratio approach in the conventional phosphor thermometry technique, the proposed single particle fit method also offers the ability to separate particle luminescence from signals with a low spatial frequency, such as light re-scattered by surrounding particles. In the presence of a level of interference from re-scattered LED light as high as 20 times the particle signal, the measured ratio was found to remain unchanged within 6%.

The implementation of the proposed concept focuses on the case of a hot gas jet flowing next to a cooled surface. A 100 -500 μm thin thermal boundary layer could be observed in the vicinity of a cooled surface. The results showed that local fluid temperature could be measured as close as 40 μm from the surface, and the results were validated against the solution of a Prandtl-Blasius equation. Moreover, since a minimum inter-measurement distance of 76 μm over a 9 \times 18 mm field of view was achieved, this technique is well-suited to cover a wide range of spatial scales, with a sub-pixel measurement resolution (<10 μm).

7.1. IMAGING OF INDIVIDUAL DISPERSED PARTICLE FOR HIGH SPATIAL RESOLUTION THERMOMETRY IN FLUIDS

On the other hand, relying on signals of individual particles, the high spatial resolution of this technique comes at the cost of a lower precision (10-25% in the ratio in this thesis) than that of the window-based approach (3-4% in the ratio), which averages signals over tens of particles within the window. The precision was not found to be limited by signals, but by other sources of particle-to-particle variations that are smoothed out by the window-based technique. These were investigated by comparing the precision obtained in various imaging configurations, with SMP:Sn²⁺ or ZnO seeded in gas or in water. Anisotropy does not seem to have a major contribution on the particle-to-particle ratio variations for the tin doped phosphors. Fluorescence perhaps from blue emitting dust particles may contribute to variations in apparent colors and therefore ratio. However, for ZnO, we cannot exclude contributions for anisotropy as it was only tested in the opposite camera configurations.

7.1.2 Application in cooling film thermometry

Cooling film technique, also known as film cooling, is a thermal management strategy widely used in high-temperature environments such as gas turbines, rocket engines, and other combustion systems. The technique involves the injection of a cooler fluid, often air, through small holes or slots in a surface that is exposed to high heat fluxes. This creates a protective thermal layer or “film” of cooler fluid that insulates the surface from the hot gases, thereby reducing the surface temperature and preventing thermal damage. The performance of these cooling films is influenced by various factors, including the mainstream flow conditions, the blowing ratios (the ratio of the mass flow rate of the coolant to the mass flow rate of the mainstream flow), and the temperature difference between the mainstream flow and the cooler gas flow (CHOI et al., 2022). Particularly, the temperature distribution in the cooling film is a critical parameter that directly affects the cooling effectiveness.

7.1. IMAGING OF INDIVIDUAL DISPERSED PARTICLE FOR HIGH SPATIAL RESOLUTION THERMOMETRY IN FLUIDS

However, in the context of optical thermometry within cooling films, the re-scattering signals from the solid surface or other system components represent a substantial challenge, since these lights can considerably contribute to the recorded luminescence when the interrogation region approaches the solid boundary side. Though phosphor thermometry has been reported in measuring temperature in gas turbine film cooling flows (SCHREIVOGEL et al., 2016; STRAUSSWALD et al., 2021), an area of about 3 mm in the vicinity of the solid surface was disregarded to minimize the measurement uncertainty and the spatial resolution was limited to ~1 mm. The concept proposed in this thesis could be applied here, which would provide the possibility of obtaining more detailed temperature profiles within the cooling film, and help to better understand the complex heat transfer process within the film under different conditions. Also, such a high spatial resolution could be particularly useful in identifying localized temperature variations within the cooling film so that it could indicate areas where the cooling film is not performing optimally, potentially leading to overheating and damaging the turbine blades. Moreover, the ability to reject low spatial frequency interfering signals shows significant benefits in these applications. By rejecting those re-scattering signals, the proposed method would be able to reduce the measurement distance from the wall from millimeter order to several dozen microns.

7.1.3 Application in thermometry in the preheated zone of a flame

Measuring temperatures near the flame front especially within the preheated zone is crucial to understand the transient behavior of the propagating flame, the spatial distributions of heat flux components, and mass burning rates over the specimen surface. In addition, the temperature in the preheated zone affects the thermal properties of the combustion material during its thermal decomposition. The main challenges of the temperature measurement in this region include the steep temperature gradients, and the small-scale structures such as turbulence-induced eddies for a premixed turbulent

7.1. IMAGING OF INDIVIDUAL DISPERSED PARTICLE FOR HIGH SPATIAL RESOLUTION THERMOMETRY IN FLUIDS

flame (MANSOUR et al., 1998). Traditional probe thermometry techniques may not provide sufficient spatial resolution to capture these fine temperature variations, and can be influenced by various heat exchange mechanisms so as to require the use of energy balance models or corrections to increase the accuracy (YILMAZ et al., 2008). On the other hand, optical methods, such as the window-based phosphor thermometry, are susceptible to the presence of interfering signals, including the luminescence from windows or substrates, background thermal radiation, and the intense light from the reaction zone, which can affect the accuracy and reliability of temperature measurements.

As the results demonstrated in Chapter. 5, this concept would be well-suited to determine the temperatures in the preheated zone of a premixed flame by seeding the selected luminescent particles in the fuel mixture. In this way, both the particle intensity distribution and its position relative to the flame front could be resolved at subpixel accuracy, hence achieving an ultra-high spatial resolution. In addition, the strong background luminosity from the flame does not affect the temperature measurement as the fitting method itself can recognize and subtract the background noise when calculating the intensity ratio. A preliminary work is being conducted by Fan et al. from the National Research Council Canada. They combine this concept with stereo-PIV technique to extract the temperatures in the preheated zone of a swirling micromix H_2 flame, and simultaneously obtain the velocity field.

7.1.4 Future works

Resolving higher seeding density case

As discussed in this thesis, for simplification and minimizing the uncertainties in the particle intensity fitting process, the particles are neglected when their centered 9×9 fitting window covers the intensity distribution of other particles. Though the current method cannot resolve particles that overlap completely in the laser thickness

7.1. IMAGING OF INDIVIDUAL DISPERSED PARTICLE FOR HIGH SPATIAL RESOLUTION THERMOMETRY IN FLUIDS

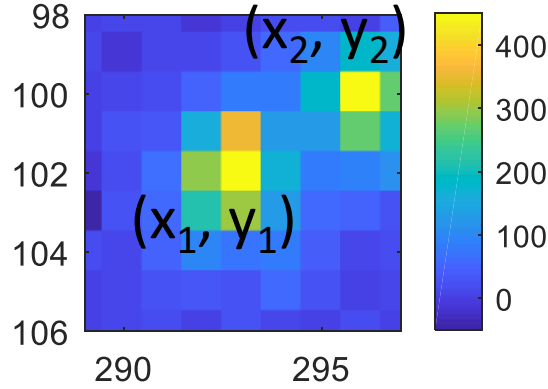


Figure 7.1: overlap particle

direction, it is possible to address the particle images overlapping in the plane, thereby allowing for dense instantaneous temperature measurements. Considering a 9×9 fitting window centered on a fitted particle 1 at location (x_1, y_1) , it also contains the partial intensity distribution of a second particle 2 located at (x_2, y_2) , as shown in Fig. 7.1. Likewise, accounting for the pixel low spatial frequency signals I_c , as explained in Eq. (4.4), the contributions of the two particles to the recorded intensity I_r in this fitting window can then be given by a double Gaussian function:

$$I_r(x, y) = I_1(x, y) + I_2(x, y) + I_c \quad (7.1)$$

where I_1 and I_2 are:

$$I_1(x, y) = I_{10} \cdot \exp \left[-a(x - x_1)^2 - 2b(x - x_1)(y - y_1) - c(y - y_1)^2 \right] \quad (7.2)$$

$$I_2(x, y) = I_{20} \cdot \exp \left[-a(x - x_2)^2 - 2b(x - x_2)(y - y_2) - c(y - y_2)^2 \right] \quad (7.3)$$

with the coefficients a, b, c already defined by Eq. (4.9-4.11), and I_{10}, I_{20} are the peak values of their intensity distribution.

7.1. IMAGING OF INDIVIDUAL DISPERSED PARTICLE FOR HIGH SPATIAL RESOLUTION THERMOMETRY IN FLUIDS

Upon performing Eq. (7.1), the intensity data for both particles can be evaluated. However, it is important to retain only the results for particle 1 for its further intensity ratio analysis. The results for particle 2 should be obtained by performing Eq. (7.1) again on the fitting window centered on particle 2. This is because the current fitting window, as shown in Fig. 7.1, does not encompass the entire intensity distribution of particle 2, which may lead to lower accuracy in the fitting results for this particle, representing a larger bias in its temperature detection.

When more than two particles contribute to the intensity within a single fitting window, the application of a sum of 2D Gaussian functions, corresponding to the number of contributing particles, is a viable approach. Consequently, by implementing the summed Gaussian function to each fitting window centered on each particle, signals of the particle at the center of those windows can be isolated.

Such a process requires obtaining, prior to fitting, the inter-particle distances for all the processed particles to determine how many particles overlap in each fitting window, and thus the number of the terms of the Gaussian functions to be added. This is readily reached through the particle localization process. Nevertheless, the overlapping particle number in each fitting window is random, necessitating a high degree of adaptability in the fitting program to adjust the number of Gaussian function terms from window to window, which underscores the need for further improvement and development of the fitting program. In addition, it should be noted that this thesis defines a window containing 81 pixels (9×9 pixels) for fitting, which is limited to resolving less than 11 overlapping particles, given that each particle image correlates to a rotated Gaussian function with 7 unknowns.

Use of the dual-frame life time method

The work presented in this dissertation focused on the application of the temperature-dependent intensity ratio, primarily derived from the spectral separation method, and

7.1. IMAGING OF INDIVIDUAL DISPERSED PARTICLE FOR HIGH SPATIAL RESOLUTION THERMOMETRY IN FLUIDS

also explored particle image distortion that can be caused by various beamsplitters in this method. A potential future development of the proposed technique could involve substituting the spectral separation method with the dual-frame lifetime approach for imaging the luminescence of individual dispersed particles. This modification could facilitate measurements using a single camera, thereby circumventing possible errors due to beamsplitter aberrations or luminescence emission anisotropy associated with the two-camera setup. Moreover, the dual-frame lifetime method could simplify the imaging processing by eliminating the need for displacement correction between ratio images.

Preliminary tests have been conducted, as the results presented Section. 5.2.3, which shows promising performance for the phosphor particles of SMP:Sn^{2+} and $\text{Y}_2\text{O}_3:\text{Eu}^{3+}$. However, since the luminescence lifetime of $\text{Y}_2\text{O}_3:\text{Eu}^{3+}$ presents an extensive insensitivity insensitive to temperature over a wide range, as observed in Fig. 5.20, it can not be identified as a good temperature tracer. The utilization of $\text{Y}_2\text{O}_3:\text{Eu}^{3+}$ aims to investigate the potential of particles generated through flame aerosol synthesis, characterized by a spherical shape, to yield reduced intensity ratio variations. Nevertheless, the comparable precision of this particle to SMP:Sn^{2+} particle eliminates the influence of the spherical shape on the temporally separated intensity ratio.

Regarding the SMP:Sn^{2+} particle, its lifetime is also initially inert to temperature, rendering it unsuitable for temperature quantification at ambient temperature. Notably, the luminescence lifetime of SMP:Sn^{2+} particle decreases rapidly when the temperature is above 600 K as illustrated in Fig. 5.18, and conversely the luminescence signals of SMP:Sn^{2+} would be very weak at temperatures above 900 K due to the temperature quenching effect as shown in FOND et al. (2019). As a result, SMP:Sn^{2+} particles could be well-suited for temperature measurement using the dual-frame lifetime method within a moderate temperature range from 600 K to 900 K, where an average lifetime sensitivity of $\sim 0.6\%/\text{K}$ can be derived from Fig. 5.18. Further testing with SMP:Sn^{2+} within this range is therefore recommended.

7.2. DETERMINATION OF TEMPERATURE DISTRIBUTION WITHIN OPAQUE PACKED BEDS

Among the four investigated particles in this thesis, $YVO_4 : 1\%Bi$ and $Y_{0.6}Sc_{0.4}VO_4 : 1\%Bi$ manifest a considerable intensity ratio variation, which indicates a high level of measurement uncertainty at this stage. Given their remarkable lifetime sensitivity as demonstrated in ELASHRY et al. (2023), future investigations aimed at mitigating their ratio variation are worthwhile. In parallel, more examinations of alternative phosphors are imperative in future work to ascertain more suitable candidate particles.

7.2 Determination of temperature distribution within opaque packed beds

7.2.1 Summary of the works

An indirect and non-contact temperature detection in opaque packed beds was introduced based on coating selected packing particles with thermographic phosphor. The results demonstrated that temperatures obtained from the dual-frame lifetime method were unaffected by the complex light propagation through the bed. Assuming the recorded luminescence with multiple phosphor-coated spheres to be a linear superposition of the intensity distributions of individual spheres, signals from multiple spheres could be separated using linear regression of individual particle spatial intensity distribution functions. For setups with three phosphor-coated spheres, their resulting reconstructed temperatures were validated against the reference values obtained with embedded thermocouples, with a mean temperature deviation of $0.8\text{ }^\circ\text{C}$ and a maximum deviation below $2\text{ }^\circ\text{C}$. In addition, the results from a repeatable experiment for one out of the three spheres showed a mean temperature bias of $3.8\text{ }^\circ\text{C}$ and a maximum bias of $9\text{ }^\circ\text{C}$.

Luminescence images were also simulated, accounting for the same structure as the experimental packed bed, to obtain the spatial intensity distribution functions

7.2. DETERMINATION OF TEMPERATURE DISTRIBUTION WITHIN OPAQUE PACKED BEDS

for individual spheres without measuring them experimentally, which would require reassembling the bed for each measured sphere position. Good agreement was found between the temperatures inferred from experimental and simulation data, although with slightly degraded accuracy. Such discrepancies are likely due to the omission of the simulation of the exciting laser light. To preliminarily anticipate whether a superimposed luminescence of a combination of multiple luminescent particles can be effectively separated, the condition number κ was proposed as a criterion. In general, the larger the condition number κ , the more sensitive a linear regression function is to small changes in the inputs, thus indicating the amplification of random errors by the least squares fit. For the signal separation process discussed in this thesis, the condition number provides a means to predict the reconstruction quality based on the individual spatial intensity distributions and the configuration of the sphere locations, yielding a priori estimation for the amplification of measurement uncertainties and errors. In principle, a condition number κ close to unity (one) leads to no or little amplification and is thereby the optimal case. The results showed the experimental condition number was closer to one compared to the simulation case, which is consistent with their degrees of accuracy and demonstrates the feasibility of the condition number. Further analysis of the condition numbers is presented in the Journal paper of XUAN et al. (2024).

7.2.2 Future Works

Extension of the amount of measured particles by multi-color imaging

At this stage, it is possible to simultaneously measure the temperatures of up to six spheres according to the condition number analysis demonstrated by XUAN et al. (2024), while practical verification would be required in future investigations. For further extending the particle amount of simultaneous measurements, a feasible method is to use multi-color imaging of phosphor particles for additional separation. Parti-

7.2. DETERMINATION OF TEMPERATURE DISTRIBUTION WITHIN OPAQUE PACKED BEDS

cles would be coated with different phosphors which emit luminescence in different wavelength ranges. Using spectral filters, or color cameras, only particles of each of the phosphor types would appear in the corresponding color-filtered image. This reduces the number of spheres to be separated on the basis of their spatial intensity distribution. For example, two-color imaging on a six-sphere configuration with two phosphors would reduce to two three-sphere signal separation problems.

Data driven optimization of heat transfer simulations

The assimilation of temperature data with the heat transfer simulation could enhance the accuracy of full-field temperature distribution predictions within packed beds. For example, in this thesis, the temperature history of the electrically heated sphere located in the top layer could be taken as the input for heat transfer simulation using the finite element method. This would obtain the transient simulated temperatures of all the packing particles. Subsequently, comparing the experiment and simulation results could accurately determine the simulation parameters such as particle-to-particle air gap, thus optimizing the heat transfer simulation.

In fact, this development has shown progress, as demonstrated in the work of XUAN et al. (2024). Upon the maturation of these results, the proposed method can be extended to probe temperatures in beds with reactive particles, such as those found in laboratory-scale microwave pyrolysis reactors or catalytic packed beds.

Extension to irregular packed beds

The long-term objective is to extend the presented technique to irregular configurations with arbitrarily shaped particles, so that measurement can be obtained in laboratory scale packing with geometries that are more relevant to the industrial process.

7.2. DETERMINATION OF TEMPERATURE DISTRIBUTION WITHIN OPAQUE PACKED BEDS

An example of such a configuration is shown in Fig. 7.2, which is reproduced from Fig. 15 in XUAN et al. (2024). The 3D computer model was obtained using a micro-CT scan, and it is also the approach we plan to employ in the future; an alternative way would be to 3D-print a model, in which case a computer model would be directly available. In Fig. 7.2 we show examples of simulated images representing the spatial intensity distribution functions when individual spheres of this packing are luminescent.

Performing reliable temperature measurements in irregular beds requires a robust calibration between experiment and simulation, including for the intrinsic camera parameters (i.e., its optical parameters) and geometric parameters such as the relative position of laser, bed, and camera. Developing this calibration will be an important aspect for future work.

The implementation of phosphor coatings on irregularly shaped particles can also be achieved by the spraying technique we described here or by using a spray-fluidized bed to increase its yield. The irregular particles could be assembled one by one but in this case, we cannot impose the location accurately, but rather aim to distribute the phosphor-coated particle at favorable locations, and then determine the exact geometry of the whole packed bed, by a similar micro-CT scan as in Fig. 7.2. The phosphor-coated particles would then be detected in the scan data by recognizing their pre-measured shapes. As discussed in Section. 6.4, the temperature calibration is essentially independent of luminescent sphere location. For irregular packing with particles of arbitrary shape, the in-situ calibration can be obtained by positioning one luminescent sphere with a thermocouple where it is most accessible and heated.

The work in this dissertation has demonstrated two novel methods for measuring temperature distributions in complex solid-fluid systems. Both concepts aim to enable discrete luminescence particles as independent thermometers by isolating the individual particle luminescence from other interfering signals or from their superposition signals, thereby allowing for thermometry in challenging environments where solid

7.2. DETERMINATION OF TEMPERATURE DISTRIBUTION WITHIN OPAQUE PACKED BEDS

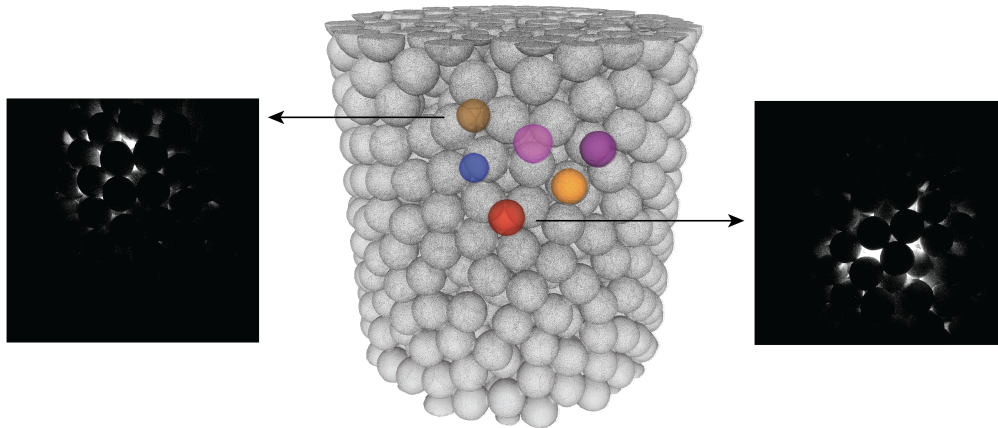


Figure 7.2: Center: micro-CT scan of irregular packing with larger number of spheres and 6 colour-marked luminescent spheres; left, right: single-particle simulated images for two different spheres. This figure is reproduced from Fig. 15 in XUAN et al. (2024).

boundaries exist. Although some preliminary development of the proposed techniques has made progress, there is also a huge space for improvement. The author believes that a further development will certainly contribute to the advancement of the optical thermometry technique.

Reference

- [ABRAM et al. 2015] C. Abram, B. Fond und F. Beyrau. **High-precision flow temperature imaging using ZnO thermographic phosphor tracer particles.** Optics Express, Vol. 23(15):19453, 2015.
- [ABRAM et al. 2018] C. Abram, B. Fond und F. Beyrau. **Temperature measurement techniques for gas and liquid flows using thermographic phosphor tracer particles.** Progress in Energy and Combustion Science, Vol. 64:93–156, 2018.
- [ABRAM et al. 2013] C. Abram, B. Fond, A. L. Heyes und F. Beyrau. **High-speed planar thermometry and velocimetry using thermographic phosphor particles.** Applied Physics B: Lasers and Optics, Vol. 111(2):155–160, 2013.
- [ABRAM et al. 2019] C. Abram, M. Mezhericher, F. Beyrau, H. A. Stone und Y. Ju. **Flame synthesis of nanophosphors using sub-micron aerosols.** Proceedings of the Combustion Institute, Vol. 37(1):1231–1239, 2019.
- [ABRAM et al. 2020] C. Abram, I. Wilson Panjikkaran, S. N. Ogugua und B. Fond. **ScVO₄: Bi³⁺ thermographic phosphor particles for fluid temperature imaging with sub-°C precision.** Optics Letters, Vol. 45(14):3893, 2020.
- [ACHARYA und KANANI 2017] S. Acharya und Y. Kanani. **Chapter Three - Advances in Film Cooling Heat Transfer.** Vol. 49 of Advances in Heat Transfer, pp. 91–156. 2017. Elsevier.
- [ALDÉN et al. 2010] M. Aldén, A. Omrane, M. Richter und G. Särner. **Thermographic phosphors for thermometry: A survey of combustion applications.** Prog. Energ. Combust., Vol. 37:422–461, 2010.
- [AXELROD D 1983] B. T. Axelrod D, Thompson NL. **Total internal reflection fluorescent microscopy.** Journal of Microscopy, Vol. 129(1):19–28, 1983.

-
- [BAHRAMI et al. 2006] M. Bahrami, M. M. Yovanovich und J. R. Culham. **Effective thermal conductivity of rough spherical packed beds.** International Journal of Heat and Mass Transfer, Vol. 49(19):3691–3701, 2006.
- [BANKS et al. 2019] D. Banks, V. Robles, B. Zhang, L. Devia-Cruz, S. Camacho-Lopez und G. Aguilar. **Planar laser induced fluorescence for temperature measurement of optical thermocavitation.** Experimental Thermal and Fluid Science, Vol. 103:385–393, 2019.
- [BAO und CHEN 2012] X. Bao und L. Chen. **Recent Progress in Distributed Fiber Optic Sensors.** Sensors, Vol. 12(7):8601–8639, 2012.
- [BAUER et al. 2019] A. Bauer, S. Wegt, M. Bopp, S. Jakirlic, C. Tropea, A. J. Krafft, N. Shokina, J. Hennig, G. Teschner und H. Egger. **Comparison of wall shear stress estimates obtained by laser Doppler velocimetry, magnetic resonance imaging and numerical simulations.** Experiments in Fluids, Vol. 60(7):1–16, 2019.
- [BEAULIEU et al. 2021] C. Beaulieu, D. Vidal, B. Yari, J. Chaouki und F. Bertrand. **Impact of surface roughness on heat transfer through spherical particle packed beds.** Chemical Engineering Science, Vol. 231:116256, 2021.
- [BECK und HURWICZ 1960] J. V. Beck und H. Hurwicz. **Effect of Thermocouple Cavity on Heat Sink Temperature.** Journal of Heat Transfer, Vol. 82(1):27–36, 1960.
- [BERSON et al. 2010] A. Berson, G. Poignand, P. Blanc-Benon und G. Comte-Bellot. **Capture of instantaneous temperature in oscillating flows: Use of constant-voltage anemometry t.** Review of Scientific Instruments, Vol. 81(1):015102, 2010.
- [BLAIR und BENNETT 1987] M. F. Blair und J. C. Bennett. **Hot-wire measurements of velocity and temperature fluctuations in a heated turbulent boundary layer.** Journal of Physics E: Scientific Instruments, Vol. 20(2):209, 1987.

-
- [BOHLIN et al. 2015] A. Bohlin, M. Mann, B. D. Patterson, A. Dreizler und C. J. Kliewer. **Development of two-beam femtosecond/picosecond one-dimensional rotational coherent anti-Stokes Raman spectroscopy: Time-resolved probing of flame wall interactions.** Proceedings of the Combustion Institute, Vol. 35(3):3723–3730, 2015.
- [BOIKO et al. 2021] V. Boiko, Z. Dai, M. Markowska, C. Leonelli, C. Mortalò, F. Armetta, F. Ursi, G. Nasillo, M. L. Saladino und D. Hreniak. **Particle size-related limitations of persistent phosphors based on the doped Y3Al2Ga3O12 system.** Scientific Reports, Vol. 11(1):1–14, 2021.
- [BRÜBACH et al. 2013] J. Brübach, C. Pflitsch, A. Dreizler und B. Atakan. **On surface temperature measurements with thermographic phosphors: A review.** Prog. Energ. Combust., Vol. 39:37–60, 2013.
- [BUONANNO et al. 2003] G. Buonanno, A. Carotenuto, G. Giovinco und N. Massarotti. **Experimental and Theoretical Modeling of the Effective Thermal Conductivity of Rough Steel Spheroid Packed Beds .** Journal of Heat Transfer, Vol. 125(4):693–702, 2003.
- [BÉTTEGA et al. 2013] R. Béttega, M. Barrozo, R. Corrêa und J. Freire. **CFD simulation of heat transfer inside packed beds: Evaluation of effective thermal conductivity.** JP Journal of Heat and Mass Transfer, Vol. 8:137–148, 2013.
- [CAI et al. 2022] T. Cai, J. Han, M. Kim, J. Jung, H. Shin und K. C. Kim. **Adaptive window technique for lifetime-based temperature and velocity simultaneous measurement using thermographic particle tracking velocimetry with a single camera.** Experiments in Fluids, Vol. 63(10):1–11, 2022.
- [CAI et al. 2021] T. Cai, M. Khodsiani, B. Hallak, C. Abram, F. Beyrau und E. Specht. **Phosphor thermometry at the surface of single reacting large-diameter spherical coke particles to characterise combustion for packed bed furnaces.** Proceedings of the Combustion Institute, Vol. 38(3):4225–4232, 2021.

-
- [CENGEL 2004] Y. A. Cengel. **Heat Transference: A Practical Approach**, Vol. 4. Second edition Edn., 2004.
- [CHANDRASEKHAR 1960] S. Chandrasekhar. **Radiative Transfer**. Dover Publications, 1960.
- [CHEN et al. 2019] L. Chen, C. Wang, M. Moscardini, M. Kamlah und S. Liu. **A DEM-based heat transfer model for the evaluation of effective thermal conductivity of packed beds filled with stagnant fluid: Thermal contact theory and numerical simulation**. International Journal of Heat and Mass Transfer, Vol. 132:331–346, 2019.
- [CHIHARA et al. 2019] T. Chihara, M. Umezawa, K. Miyata, S. Sekiyama, N. Hosokawa, K. Okubo, M. Kamimura und K. Soga. **Biological Deep Temperature Imaging with Fluorescence Lifetime of Rare-Earth-Doped Ceramics Particles in the Second NIR Biological Window**. Scientific Reports, Vol. 9(1):1–8, 2019.
- [CHO und CHO 2009] E. Cho und M. J. Cho. **Variance of sample variance with replacement**. International Journal of Pure and Applied Mathematics, Vol. 52(1):43–47, 2009.
- [CHOI et al. 2022] J. Choi, J. Choi, H. Kwon, H. Jang und H. Park. **Experimental investigation of the film cooling performance by triangular-shaped thin plates on inclined cylindrical holes**. Frontiers in Energy Research, Vol. 10, 2022.
- [CIERPKA et al. 2010] C. Cierpka, M. Rossi, R. Segura und C. J. Kähler. **On the calibration of astigmatism particle tracking velocimetry for microflows**. Measurement Science and Technology, Vol. 22(1):015401, 2010a.
- [CIERPKA et al. 2010] C. Cierpka, R. Segura, R. Hain und C. J. Kähler. **A simple single camera 3C3D velocity measurement technique without errors due to depth of correlation and spatial averaging for microfluidics**. Measurement Science and Technology, Vol. 21(4):045401, 2010b.

-
- [CLEVE et al. 2017] S. Cleve, E. Jondeau, P. Blanc-Benon und G. Comte-Bellot. **Cold wire constant voltage anemometry to measure temperature fluctuations and its application in a thermoacoustic system.** Review of Scientific Instruments, Vol. 88(4):044904, 2017.
- [CUVIER et al. 2017] C. Cuvier, S. Srinath, M. Stanislas, J. M. Foucaut, J. P. Laval, C. J. Kähler, R. Hain, S. Scharnowski, A. Schröder, R. Geisler, J. Agocs, A. Röse, C. Willert, J. Klinner, O. Amili, C. Atkinson und J. Soria. **Extensive characterisation of a high Reynolds number decelerating boundary layer using advanced optical metrology.** Journal of Turbulence, Vol. 18(10):929–972, 2017.
- [DAI et al. 2019] W. Dai, D. Hanaor und Y. Gan. **The effects of packing structure on the effective thermal conductivity of granular media: A grain scale investigation.** International Journal of Thermal Sciences, Vol. 142:266–279, 2019.
- [DE BEER et al. 2018] M. De Beer, C. Du Toit und P. Rousseau. **Experimental study of the effective thermal conductivity in the near-wall region of a packed pebble bed.** Nuclear Engineering and Design, Vol. 339:253–268, 2018.
- [DRAGOMIROV et al. 2018] P. Dragomirov, A. Mendieta, C. Abram, B. Fond und F. Beyrau. **Planar measurements of spray-induced wall cooling using phosphor thermometry.** Experiments in Fluids, Vol. 59(3):1–13, 2018.
- [DUNNMON et al. 2017] J. Dunnmon, S. Sobhani, M. Wu, R. Fahrig und M. Ihme. **An investigation of internal flame structure in porous media combustion via X-ray Computed Tomography.** Proceedings of the Combustion Institute, Vol. 36(3):4399–4408, 2017.
- [DÍAZ-HERAS et al. 2020] M. Díaz-Heras, J. Belmonte und J. Almendros-Ibáñez. **Effective thermal conductivities in packed beds: Review of correlations and its influence on system performance.** Applied Thermal Engineering, Vol. 171:115048, 2020.

-
- [ELASHRY et al. 2023] M. Elashry, A. Rashed, L. Dalipi, U. Betke, C. Abram und B. Fond. **Bismuth-doped rare-earth orthovanadates as tunable luminescence decay-time thermometers.** 2023.
- [ESCOFET-MARTIN et al. 2021] D. Escofet-Martin, A. Ojo, N. Mecker, M. Linne und B. Peterson. **Simultaneous 1D hybrid fs/ps rotational CARS, phosphor thermometry, and CH* imaging to study transient near-wall heat transfer processes.** Proceedings of the Combustion Institute, Vol. 38(1):1579–1587, 2021.
- [FAN und HOCHGREB 2019] L. Fan und S. Hochgreb. **Uncertainty analysis in structured laser illumination planar imaging (SLIPI) applied to non-linear signals: Gas-phase phosphor thermometry.** Measurement Science and Technology, Vol. 30(8), 2019.
- [FAN et al. 2022] L. Fan, P. Vena, B. Savard und B. Fond. **Experimental and numerical investigation on the accuracy of phosphor particle streak velocimetry.** Experiments in Fluids 2022, Vol. 63:165(165):1–20, 2022.
- [FAN et al. 2021] L. Fan, P. Vena, B. Savard, G. Xuan und B. Fond. **High-resolution velocimetry technique based on the decaying streaks of phosphor particles.** Optics Letters, Vol. 46(3):641, 2021.
- [FOND et al. 2015] B. Fond, C. Abram und F. Beyrau. **Characterisation of the luminescence properties of BAM:Eu²⁺ particles as a tracer for thermographic particle image velocimetry.** Applied Physics B: Lasers and Optics, Vol. 121(4):495–509, 2015.
- [FOND et al. 2012] B. Fond, C. Abram, A. L. Heyes, A. M. Kempf und F. Beyrau. **Simultaneous temperature, mixture fraction and velocity imaging in turbulent flows using thermographic phosphor tracer particles.** Optics Express, Vol. 20(20):22118, 2012.
- [FOND et al. 2019] B. Fond, C. Abram, M. Pougin und F. Beyrau. **Investigation of the tin-doped phosphor (Sr,Mg)₃(PO₄):Sn²⁺ for fluid temperature measurements.** Optical Materials Express, Vol. 9(2):802, 2019.

-
- [FRANK und KAISER 2008] J. H. Frank und S. A. Kaiser. **High-resolution imaging of dissipative structures in a turbulent jet flame with laser Rayleigh scattering.** Experiments in Fluids, Vol. 44(2):221–233, 2008.
- [FUCHS2022 et al.] **Near-wall turbulence and wall-shear-stress measurements using volumetric μ PTV.**
- [GANGURDE et al. 2017] L. S. Gangurde, G. S. J. Sturm, T. J. Devadiga, A. I. Stankiewicz und G. D. Stefanidis. **Complexity and Challenges in Noncontact High Temperature Measurements in Microwave-Assisted Catalytic Reactors.** Industrial & Engineering Chemistry Research, Vol. 56(45):13379–13391, 2017. PMID: 29170599.
- [GARCÍA-BAÑOS et al. 2019] B. García-Baños, J. J. Reinoso, F. L. Peñaranda-Foix, J. F. Fernández und J. M. Catalá-Civera. **Temperature Assessment Of Microwave-Enhanced Heating Processes.** Scientific Reports, Vol. 9(1):1–10, 2019.
- [GEITENBEEK et al. 2018] R. G. Geitenbeek, A.-E. Nieuwelink, T. S. Jacobs, B. B. V. Salzman, J. Goetze, A. Meijerink und B. M. Weckhuysen. **In Situ Luminescence Thermometry To Locally Measure Temperature Gradients during Catalytic Reactions.** ACS Catalysis, Vol. 8(3):2397–2401, 2018. PMID: 29527404.
- [GUASTO und BREUER 2008] J. S. Guasto und K. S. Breuer. **Simultaneous, ensemble-averaged measurement of near-wall temperature and velocity in steady microflows using single quantum dot tracking.** Experiments in Fluids, Vol. 45(1):157–166, 2008.
- [HERTLEIN und DU PUIITS 2021] A. Hertlein und R. du Puits. **Direct measurements of the thermal dissipation rate in turbulent Rayleigh–Bénard convection.** Physics of Fluids, Vol. 33(3):035139, 2021.
- [HERZOG et al. 2021] J. M. Herzog, D. Witkowski und D. A. Rothamer. **Combustion-relevant aerosol phosphor thermometry imaging using Ce,Pr:LuAG, Ce:GdPO₄, and Ce:CSSO.** Proceedings of the Combustion Institute, Vol. 38(1):1617–1625, 2021.

-
- [HORN 2020] R. Horn. *Reaktoren für Fluid-Feststoff-Reaktionen: Festbettreaktoren*, pp. 1–70. 2020. Springer Berlin Heidelberg, Berlin, Heidelberg.
- [JAINSKI et al. 2014] C. Jainski, L. Lu, V. Sick und A. Dreizler. **Laser imaging investigation of transient heat transfer processes in turbulent nitrogen jets impinging on a heated wall**. *International Journal of Heat and Mass Transfer*, Vol. 74:101–112, 2014.
- [KÄHLER et al. 2012] C. J. Kähler, S. Scharnowski und C. Cierpka. **On the resolution limit of digital particle image velocimetry**. *Experiments in Fluids*, Vol. 52(6):1629–1639, 2012a.
- [KÄHLER et al. 2012] C. J. Kähler, S. Scharnowski und C. Cierpka. **On the uncertainty of digital PIV and PTV near walls**. *Experiments in Fluids*, Vol. 52(6):1641–1656, 2012b.
- [KLEWICKI und FALCO 1990] J. C. Klewicki und R. E. Falco. **On accurately measuring statistics associated with small-scale structure in turbulent boundary layers using hot-wire probes**. *Journal of Fluid Mechanics*, Vol. 219:119–142, 1990.
- [KOEGL et al. 2020] M. Koegl, M. Pahlevani und L. Zigan. **A Novel Approach for Measurement of Composition and Temperature of N-Decane/Butanol Blends Using Two-Color Laser-Induced Fluorescence of Nile Red**. *Sensors*, Vol. 20(19), 2020.
- [KOLLIE et al. 1977] T. G. Kollie, R. L. Anderson, J. L. Horton und M. J. Roberts. **Large thermocouple thermometry errors caused by magnetic fields**. *Review of Scientific Instruments*, Vol. 48(5):501–511, 1977.
- [KOSAKA et al. 2018] H. Kosaka, F. Zentgraf, A. Scholtissek, L. Bischoff, T. Häber, R. Suntz, B. Albert, C. Hasse und A. Dreizler. **Wall heat fluxes and CO formation/oxidation during laminar and turbulent side-wall quenching of methane and DME flames**. *International Journal of Heat and Fluid Flow*, Vol. 70(September 2017):181–192, 2018.

-
- [KRISHNA et al. 2017] S. Krishna, D. A. Lacoste, W. L. Roberts, J. S. Damazo und E. Kwon. **Temperature measurements in a wall stabilized steady flame using CARS.** AIAA SciTech Forum - 55th AIAA Aerospace Sciences Meeting, (January):1–7, 2017.
- [KRISHNA et al. 2019] Y. Krishna, A. M. Elbaz, Y. Yue und G. Magnotti. **Mole fraction measurement through a transparent quartz burner using filtered Rayleigh scattering.** Appl. Opt., Vol. 58(20):5575–5586, 2019.
- [KRISHNA et al. 2021] Y. Krishna, A. M. Mahuthannan, X. Luo, D. A. Lacoste und G. Magnotti. **High-speed filtered Rayleigh scattering thermometry in premixed flames through narrow channels.** Combustion and Flame, Vol. 225:329–339, 2021.
- [KRSMANOVIĆ et al. 2011] R. M. Krsmanović, Željka Antić, M. G. Nikolić, M. Mitrić und M. D. Dramićanin. **Preparation of Y₂O₃:Eu³⁺ nanopowders via polymer complex solution method and luminescence properties of the sintered ceramics.** Ceramics International, Vol. 37(2):525–531, 2011.
- [LEE et al. 2016] H. Lee, B. Böhm, A. Sadiki und A. Dreizler. **Turbulent heat flux measurement in a non-reacting round jet, using BAM:Eu²⁺ phosphor thermography and particle image velocimetry.** Applied Physics B: Lasers and Optics, Vol. 122(7):1–13, 2016.
- [LI et al. 2023] T. Li, C. Geschwindner, A. Dreizler und B. Böhm. **Particle-resolved optical diagnostics of solid fuel combustion for clean power generation: a review.** Measurement Science and Technology, 2023.
- [LOPEZ-BONILLA et al. 2023] J. Lopez-Bonilla, H. Greichen, F. Beyrau, B. Gunar und B. Fond. **Phosphor thermometry using the phase-shift: optimisation of the measurement precision and application to 2D measurements on a battery.** in preparation for submission to Measurement Science and Technology, 2023.
- [LOWE et al. 2022] D. H. Lowe, S. L. Andersen, G. Sutton, J. I. Camacho, M. B. Copeland, H. Kjeldsen und K. L. Laursen. **Electromagnetic immune phosphor-tipped fibre-**

-
- optic thermometers.** Measurement Science and Technology, Vol. 33(6):065007, 2022.
- [MA et al. 2023] X. Ma, C. Fan, W. Shao, Q. Cao und Z. Cui. **Numerical and experimental studies of packed bed thermal energy storage system based on a novel transient energy model.** Energy Science & Engineering, Vol. 11(2):727–744, 2023.
- [MANSOUR et al. 1998] M. S. Mansour, N. Peters und Y.-C. Chen. **Investigation of scalar mixing in the thin reaction zones regime using a simultaneous CH-LIF/Rayleigh laser technique.** Symposium (International) on Combustion, Vol. 27(1):767–773, 1998. Twenty-Seventh Symposium (International) on Combustion Volume One.
- [MASSING et al. 2016] J. Massing, D. Kaden, C. J. Kähler und C. Cierpka. **Luminescent two-color tracer particles for simultaneous velocity and temperature measurements in microfluidics.** Measurement Science and Technology, Vol. 27(11):115301, 2016.
- [MASSING et al. 2018] J. Massing, C. J. Kähler und C. Cierpka. **A volumetric temperature and velocity measurement technique for microfluidics based on luminescence lifetime imaging.** Experiments in Fluids, Vol. 59(11):1–13, 2018.
- [MCMANUS et al. 2020] T. A. Mcmanus, J. A. Sutton und J. A. Sutton. **Simultaneous 2D filtered Rayleigh scattering thermometry and stereoscopic particle image velocimetry measurements in turbulent non - premixed flames.** Experiments in Fluids, Vol. 61(6):1–19, 2020.
- [MENDIETA et al. 2019] A. Mendieta, B. Fond, P. Dragomirov und F. Beyrau. **A delayed gating approach for interference-free ratio-based phosphor thermometry.** Measurement Science and Technology, Vol. 30(7):074002, 2019.
- [MYDLARSKI und WARHAFT 1998] L. MYDLARSKI und Z. WARHAFT. **Passive scalar statistics in high-Péclet-number grid turbulence.** Journal of Fluid Mechanics, Vol. 358:135–175, 1998.

-
- [NAGANO und TSUJI 1994] Y. Nagano und T. Tsuji. **Recent developments in hot- and cold-wire techniques for measurements in turbulent shear flows near walls.** Experimental Thermal and Fluid Science, Vol. 9(2):94–110, 1994. Special Issue on Measurement in Turbulent Flow.
- [NILSSON et al. 2023] S. Nilsson, H. Feuk und M. Richter. **High temperature thermographic phosphors YAG:Tm;Li and YAG:Dy in reduced oxygen environments.** Journal of Luminescence, Vol. 256:119645, 2023.
- [OJO et al. 2021] A. O. Ojo, D. Escofet-Martin, J. Collins, G. Falconetti und B. Peterson. **Experimental investigation of thermal boundary layers and associated heat loss for transient engine-relevant processes using HRCARS and phosphor thermometry.** Combustion and Flame, Vol. 233:111567, 2021.
- [OJO et al. 2015] A. O. Ojo, B. Fond, B. G. M. Van Wachem, A. L. Heyes und F. Beyrau. **Thermographic laser Doppler velocimetry.** Optics Letters, Vol. 40(20):4759, 2015.
- [OMRANE et al. 2002] A. Omrane, F. Ossler und M. Aldén. **Two-dimensional surface temperature measurements of burning materials.** Proc. Combust. Inst, Vol. 29:2653–2659, 2002.
- [PENNELL et al. 1972] W. Pennell, E. Sparrow und E. Eckert. **Turbulence intensity and time-mean velocity distributions in low reynolds number turbulent pipe flows.** International Journal of Heat and Mass Transfer, Vol. 15(5):1067–1074, 1972.
- [PETERSON et al. 2014] B. Peterson, E. Baum, B. Böhm, V. Sick und A. Dreizler. **Evaluation of toluene LIF thermometry detection strategies applied in an internal combustion engine.** Applied Physics B: Lasers and Optics, Vol. 117(1):151–175, 2014.
- [PICHLER et al. 2021] M. Pichler, B. Haddadi, C. Jordan, H. Norouzi und M. Harasek. **Effect of particle contact point treatment on the CFD simulation of the heat transfer in packed beds.** Chemical Engineering Research and Design, Vol. 165:242–253, 2021.

-
- [PIEJAK et al. 1998] R. Piejak, V. Godyak, B. Alexandrovich und N. Tishchenko. **Surface temperature and thermal balance of probes immersed in high density plasma.** Plasma Sources Science and Technology, Vol. 7(4):590, 1998.
- [PISANI et al. 2022] N. Pisani, E. Numkam Fokoua, I. A. Davidson, F. Poletti, R. Slavík, D. Lowe, G. Machin und G. Sutton. **Toward Gamma Ray Immune Fibre-Optic Phosphor Thermometry for Nuclear Decommissioning.** International Journal of Thermophysics, Vol. 43(4):1–16, 2022.
- [PUITS et al.] **Thermal boundary layers in turbulent Rayleigh-Bénard convection with rough surfaces.**
- [RAFFEL et al. 2018] M. Raffel, C. E. Willert, F. Scarano, C. J. Kähler, S. T. Wereley und J. Kompenhans. **Particle Image Velocimetry: A Practical Guide.** Springer International Publishing, 3 Edn., 2018.
- [RASHED 2022] A. F. O. Rashed. **Lifetime imaging phosphor thermometry: Synthesis of new thermographic phosphors and application to hydrogeology.** Master's thesis, Institute of Fluid Dynamics and Thermodynamics, Otto-von-Guericke-Universität Magdeburg, 2022.
- [RODRIGUES et al. 2022] S. J. Rodrigues, N. Vorhauer-Huget und E. Tsotsas. **Effective thermal conductivity of packed beds made of cubical particles.** International Journal of Heat and Mass Transfer, Vol. 194:122994, 2022.
- [ROSS et al. 2001] D. Ross, M. Gaitan und L. E. Locascio. **Temperature Measurement in Microfluidic Systems Using a Temperature-Dependent Fluorescent Dye.** Analytical Chemistry, Vol. 73(17):4117–4123, 2001.
- [ROUSSEAU et al. 2014] P. Rousseau, C. du Toit, W. van Antwerpen und H. van Antwerpen. **Separate effects tests to determine the effective thermal conductivity in the PBMR HTTU test facility.** Nuclear Engineering and Design, Vol. 271:444–458, 2014.

-
- [SCHNEIDERS et al. 2017] J. F. Schneiders, F. Scarano und G. E. Elsinga. **Resolving vorticity and dissipation in a turbulent boundary layer by tomographic PTV and VIC+**. Experiments in Fluids, Vol. 58(4):1–14, 2017.
- [SCHREIVOGEL et al. 2016] P. Schreivogel, C. Abram, B. Fond, M. Straußwald, F. Beyrau und M. Pfitzner. **Simultaneous kHz-rate temperature and velocity field measurements in the flow emanating from angled and trenched film cooling holes**. International Journal of Heat and Mass Transfer, Vol. 103(x):390–400, 2016.
- [SHAN et al. 2010] J. Shan, M. Uddi, R. Wei, N. Yao und Y. Ju. **The Hidden Effects of Particle Shape and Criteria for Evaluating the Upconversion Luminescence of the Lanthanide Doped Nanophosphors**. The Journal of Physical Chemistry C, Vol. 114(6):2452–2461, 2010.
- [SHEN und BRAY 1997] Y. Shen und K. Bray. **Effect of pressure and temperature on the lifetime of in yttrium aluminum garnet**. Physical Review B - Condensed Matter and Materials Physics, Vol. 56(17):10882–10891, 1997.
- [SHIMURA et al. 2019] M. Shimura, S. Yoshida, K. Osawa, Y. Minamoto, T. Yokomori, K. Iwamoto, M. Tanahashi und H. Kosaka. **Micro particle image velocimetry investigation of near-wall behaviors of tumble enhanced flow in an internal combustion engine**. International Journal of Engine Research, Vol. 20(7):718–725, 2019.
- [SIDDIQUE und SALEMA 2023] I. J. Siddique und A. A. Salema. **Unraveling the metallic thermocouple effects during microwave heating of biomass**. Energy, Vol. 267:126529, 2023.
- [SOMEYA 2021] S. Someya. **Particle-based temperature measurement coupled with velocity measurement**. Measurement Science and Technology, Vol. 32(4):042001, 2021.
- [SOMEYA et al. 2011] S. Someya, Y. Li, K. Ishii und K. Okamoto. **Combined two-dimensional velocity and temperature measurements of natural convection using**

-
- a high-speed camera and temperature-sensitive particles.** Experiments in Fluids, Vol. 50(1):65–73, 2011a.
- [SOMEYA et al. 2011] S. Someya, M. Uchida, K. Tominaga, H. Terunuma, Y. Li und K. Okamoto. **Lifetime-based phosphor thermometry of an optical engine using a high-speed CMOS camera.** International Journal of Heat and Mass Transfer, Vol. 54(17):3927–3932, 2011b.
- [SPOSITO et al. 2021] A. Sposito, E. Heaps, G. Sutton, G. Machin, R. Bernard und S. Clarke. **Phosphor thermometry for nuclear decommissioning and waste storage.** Nuclear Engineering and Design, Vol. 375:111091, 2021.
- [STELTER et al. 2023] M. Stelter, F. Martins, F. Beyrau und B. Fond. **Thermographic 3D Particle Tracking Velocimetry in turbulent gas flows.** Measurement Science and Technology, Vol. 34:074008, 2023.
- [STEPHAN et al. 2019] M. Stephan, F. Zentgraf, E. Berrocal, B. Albert, B. Böhm und A. Dreizler. **Multiple scattering reduction in instantaneous gas phase phosphor thermometry: Applications with dispersed seeding.** Measurement Science and Technology, Vol. 30(5), 2019.
- [STRAUSSWALD et al. 2021] M. Straußwald, C. Abram, T. Sander, F. Beyrau und M. Pfitzner. **Time-resolved temperature and velocity field measurements in gas turbine film cooling flows with mainstream turbulence.** Experiments in Fluids, Vol. 62(1):1–17, 2021.
- [THOMÉO et al. 2004] J. C. Thoméo, C. O. Rouiller und J. T. Freire. **Experimental Analysis of Heat Transfer in Packed Beds with Air Flow.** Industrial & Engineering Chemistry Research, Vol. 43(15):4140–4148, 2004.
- [TOSCANO et al. 2022] A. M. Toscano, M. R. Lato, D. Fontanarosa und M. G. De Giorgi. **Optical Diagnostics for Solid Rocket Plumes Characterization: A Review.** Energies, Vol. 15(4), 2022.

-
- [TSORY et al. 2013] T. Tsory, N. Ben-Jacob, T. Brosh und A. Levy. **Thermal DEM–CFD modeling and simulation of heat transfer through packed bed**. Powder Technology, Vol. 244:52–60, 2013.
- [TSOTSAS und MARTIN 1987] E. Tsotsas und H. Martin. **Thermal conductivity of packed beds: A review**. Chemical Engineering and Processing: Process Intensification, Vol. 22(1):19–37, 1987.
- [UNNIKRISHNAN und YANG 2022] U. Unnikrishnan und V. Yang. **A review of cooling technologies for high temperature rotating components in gas turbine**. Propulsion and Power Research, Vol. 11(3):293–310, 2022.
- [VALIEV et al. 2018] D. Valiev, T. Han, S. Stepanov, V. Vaganov und V. Paygin. **The effect of BaF₂ concentration and particle size distribution on the luminescence efficiency of YAG:Ce³⁺ phosphors**. Materials Research Express, Vol. 5(9):096201, 2018.
- [VAN LIPZIG et al. 2013] J. P. Van Lipzig, M. Yu, N. J. Dam, C. C. Luijten und L. P. De Goey. **Gas-phase thermometry in a high-pressure cell using BaMgAl 10017:Eu as a thermographic phosphor**. Applied Physics B: Lasers and Optics, Vol. 111(3):469–481, 2013.
- [VOGT und STEPHAN 2012] J. Vogt und P. Stephan. **Using microencapsulated fluorescent dyes for simultaneous measurement of temperature and velocity fields**. Measurement Science and Technology, Vol. 23(10):105306, 2012.
- [WIENEKE 2005] B. Wieneke. **Stereo-PIV using self-calibration on particle images**. Experiments in Fluids, Vol. 39(2):267–280, 2005.
- [WU und MIRBOD 2018] Z. Wu und P. Mirbod. **Experimental analysis of the flow near the boundary of random porous media**. Physics of Fluids, Vol. 30(4):047103, 2018.

-
- [XUAN et al. 2024] G. Xuan, M. Ebert, S. J. Rodrigues, N. Vorhauer-Huget, C. Lessig und B. Fond. **Multi-point temperature measurements in packed beds using phosphor thermometry and ray tracing simulations.** *Particuology*, Vol. 85:77–88, 2024.
- [XUAN et al. 2023] G. Xuan, L. Fan, F. Beyrau und B. Fond. **High spatial resolution fluid thermometry in boundary layers by macroscopic imaging of individual phosphor tracer particles.** *Experimental Thermal and Fluid Science*, Vol. 148(May):110977, 2023.
- [YANG und CAI 2019] X. Yang und Z. Cai. **An analysis of a packed bed thermal energy storage system using sensible heat and phase change materials.** *International Journal of Heat and Mass Transfer*, Vol. 144:118651, 2019.
- [YAO et al. 2016] Z. F. Yao, Z. J. Yang und F. J. Wang. **Evaluation of near-wall solution approaches for large-eddy simulations of flow in a centrifugal pump impeller.** *Engineering Applications of Computational Fluid Mechanics*, Vol. 10(1):452–465, 2016.
- [YEH und ATTA 1973] T. T. Yeh und C. W. Atta. **Spectral transfer of scalar and velocity fields in heated-grid turbulence.** *Journal of Fluid Mechanics*, Vol. 58(2):233–261, 1973.
- [YILMAZ et al. 2008] N. Yilmaz, W. Gill, A. B. Donaldson und R. E. Lucero. **Problems encountered in fluctuating flame temperature measurements by thermocouple.** *Sensors (Basel)*, Vol. 8(12):7882–7893, 2008.
- [YOO et al. 2011] J. Yoo, D. Mitchell, D. F. Davidson und R. K. Hanson. **Near-wall imaging using toluene-based planar laser-induced fluorescence in shock tube flow.** *Shock Waves*, Vol. 21(6):523–532, 2011.
- [ZENTGRAF et al. 2017] F. Zentgraf, M. Stephan, E. Berrocal, B. Albert, B. Böhm und A. Dreizler. **Application of structured illumination to gas phase thermometry using**

thermographic phosphor particles: a study for averaged imaging. Experiments in Fluids, Vol. 58(7):1–15, 2017.

[ZHAO et al. 2019] Y. Zhao, P. Zhao, Y. Liu, Y. Xu und J. F. Torres. **On the selection of perturbations for thermal boundary layer control.** Physics of Fluids, Vol. 31(10):104102, 2019.

[ĆIRIĆ et al. 2020] A. Ćirić, S. Stojadinović und M. D. Dramićanin. **Temperature and concentration dependent Judd-Ofelt analysis of $Y_2O_3:Eu^{3+}$ and $YVO_4:Eu^{3+}$.** Physica B: Condensed Matter, Vol. 579:411891, 2020.

Publications list

The work conducted during the PhD and presented in this thesis is associated with the following publications.

Journal publications

1. Xuan, G., Fan, L., Beyrau, F., & Fond, B. (2023). High spatial resolution fluid thermometry in boundary layers by macroscopic imaging of individual phosphor tracer particles. *Experimental Thermal and Fluid Science*, 110977.
2. Xuan, G., Ebert, M., Rodrigues, S. J., Vorhauer-Huget, N., Lessig, C., & Fond, B. (2024). Multi-point temperature measurements in packed beds using phosphor thermometry and ray tracing simulations. *Particuology*, 85, 77-88.
3. Fan, L., Vena, P., Savard, B., Xuan, G., & Fond, B. (2021). High-resolution velocimetry technique based on the decaying streaks of phosphor particles. *Optics Letters*, 46(3), 641-644.

Conference proceedings

1. G. Xuan, L. Fan, F. Beyrau, and B. Fond (2023). Near wall 2D Fluid temperature measurement based on Gaussian-fitting of individual phosphor tracer particle images. *Proceedings of the European Combustion Meeting 2023*, 11th European Combustion Meeting, 26. - 28. April 2023, Rouen, FRANCE
2. G. Xuan, M. Ebert, S. J. Rodrigues, N. Vorhauer-Huget, C. Lessig, and B. Fond (2023). Temperature distribution in packed beds using a hybrid phosphor thermometry, ray tracing and data assimilation approach. *Proceedings of the European Combustion*

Meeting 2023, 11th European Combustion Meeting, 26. - 28. April 2023, Rouen, FRANCE

3. G. Xuan, M. Ebert, S. J. Rodrigues, N. Vorhauer-Huget, C. Lessig, and B. Fond (2022). Multi-point temperature measurements in packed beds of opaque particles using phosphor thermometry with an image-based signal separation technique. *The third International Conference on Phosphor Thermometry*, 18. - 20. July 2022, Magdeburg, Germany
4. G. Xuan, M. Ebert, S. J. Rodrigues, N. Vorhauer-Huget, C. Lessig, and B. Fond (2022). Temperature distribution in granular assemblies using luminescence thermometry and radiative transfer simulation. *Laser Applications to Chemical, Security and Environmental Analysis*, 11. - 15. July 2022, Vancouver, British Columbia, Canada
5. G. Xuan, C. Abram, F. Beyrau, B. Fond (2020). High-resolution interference-free fluid temperature imaging based on two-dimensional fits of single particle images. *The second International Conference on Phosphor Thermometry*, 27. - 29. July 2020, Magdeburg, Germany
6. G. Xuan, C. Abram, F. Beyrau, B. Fond (2020). Single-particle fitting technique for interference-free fluid temperature imaging at 10 microns in-plane spatial resolution. *Laser Applications to Chemical, Security and Environmental Analysis*, 22. - 26. June 2020, Washington, DC, United States

Declaration of Honor

I hereby declare that I produced this thesis without prohibited external assistance and that none other than the listed references and tools have been used.

In the case of co-authorship, especially in the context of a cumulative dissertation, the own contribution is correctly and completely stated. I did not make use of any commercial consultant concerning graduation. A third party did not receive any non-monetary perquisites neither directly nor indirectly for activities which are connected with the contents of the presented thesis. All sources of information are clearly marked, including my own publications.

In particular I have not consciously:

- Fabricated data or rejected undesired results,
- Misused statistical methods with the aim of drawing other conclusions than those warranted by the available data,
- Plagiarized data or publications,
- Presented the results of other researchers in a distorted way.

I do know that violations of copyright may lead to injunction and damage claims of the author and also to prosecution by the law enforcement authorities.

I hereby agree that the thesis may need to be reviewed with an electronic data processing for plagiarism.

This work has not yet been submitted as a doctoral thesis in the same or a similar form in Germany or in any other country. It has not yet been published as a whole.

Magdeburg, November 30, 2023

MSc. Guangtao Xuan